

# **GALLIUM NITRIDE THIN FILMS**

**SUBSTRATES MANIPULATION AND EPITAXIAL  
GROWTH OF GALLIUM NITRIDE THIN FILMS**

**By**

**HUAXIANG SHEN, M. ENG., B. ENG.**

A Thesis submitted to the School of Graduate Studies in Partially  
Fulfillment of the Requirements for the Degree Doctor of Philosophy

McMaster University

© Copyright by Huaxiang Shen, January 2014

DOCTOR OF PHILOSOPHY (2014)      McMaster University

Materials Science

Hamilton, Ontario

TITLE: Substrates Manipulation and Epitaxial Growth of  
Gallium Nitride Thin Films

AUTHOR: Huaxiang Shen, M. Eng. (Zhejiang University), B.  
Eng. (Zhejiang University)

SUPERVISOR: Professor Adrian H. Kitai

NUMBER OF PAGES: xxvi, 186

## Abstract

Light emitting diode (LED)-based solid state displays (SSD) have attracted growing interest due to their advantages in terms of contrast ratio, brightness, viewing angle, and response time compared to liquid crystal displays. GaN based III-nitride thin film materials are suitable materials for SSD due to their wide and tunable bandgaps. However, the large size and costly manufacturing process of commercially available GaN-based LED chips limit the potential uses of LEDs as the pixels of SSD.

In this work, tiny single crystal  $\beta$ -phase (111) oriented SiC whiskers 2  $\mu\text{m}$  in diameter and 18  $\mu\text{m}$  in length are proposed as the substrates for GaN growth due to their small lattice constant mismatch (3%) with GaN, their conductive nature and their small size for potential use in SSD pixels. Aligned SiC whiskers with (111) planes exposed in an alumina matrix prepared by a precise manipulation and alignment method of SiC whiskers including a series of steps was developed in this work. The alignment degree of whiskers achieved in this work is higher than conventional extrusion methods, and a sintering approach capable of forming an aligned alumina/SiC composite was developed and understood using a self-limiting oxidation reaction mechanism.

To take advantage of the potential versatility, scalability and cost effectiveness of sputtering for SSD manufacturing, a reactive sputtering system was built for a

detailed investigation of GaN thin film growth nucleation and subsequent growth behavior on SiC. 6H-SiC single crystal substrates were chosen as a reference substrate for SiC whiskers. An XRRC indicates that a high quality single crystalline GaN thin film was successfully grown epitaxially on 6H-SiC by sputtering. Two-dimensional X-ray diffraction and scanning transmission electron microscopy results demonstrated that the epitaxial growth of GaN thin films relies on the short range order and/or crystalline area of the native oxide layer in GaN/SiC interface for the first time.

## Acknowledgements

The work described in this thesis could not have been finished without the instruction of my supervisor Dr. Adrian Kitai, who is not only a wonderful supervisor but also a nice friend. I deeply appreciate him for his solid expertise, selfless support and optimistic encouragement throughout the whole process of my Ph.D. study in McMaster University. I would also like to express my gratitude to the members of my supervisory committee: Dr. Marek Niewczas and Dr. Ray LaPierre for their support and helpful advises.

Special thanks to Dr. Guozhen Zhu for her help on TEM characterization and fruitful discussion about the results. I also wish to express my thank to Dr. Ping Wei for his help on tape casting.

I would also like to thank the following people for their technical support for my research: Wen He Gong, Jim Garrett, Connie Barry, Jim Britten, Steve Koprach, Chris Butcher, Doug Culley, and Victoria Jarvis. The work cannot go smoothly without their help. The enormous help from my colleagues in Adrian's group are also acknowledged here.

In the end, I would like to dedicate this thesis to my wife, Shilei Chen and my parents for their understanding and support. Your support is the biggest motivation in my life.

# Table of Contents

1	Introduction.....	1
2	Literature Review.....	6
2.1	Overview: LEDs.....	6
2.1.1	Brief History of LEDs.....	6
2.1.2	Semiconductor Materials for LEDs.....	10
2.1.3	Electrical properties of P-N junctions .....	21
2.1.4	LED Manufacturing Process .....	27
2.2	III-Nitride Compound Semiconductors.....	36
2.2.1	Crystal Structure of Nitrides .....	36
2.2.2	Physical Properties of III-Nitrides .....	39
2.2.3	Epitaxial Growth Technique for III-Nitride Semiconductors.....	44
2.2.4	Substrates for the epitaxial growth of III-nitride thin film.....	55
2.3	Silicon Carbide Whiskers and Their Alignment.....	68
2.3.1	Materials Properties .....	68
2.3.2	Synthesis of SiC Whiskers .....	69
2.3.3	Alignment of SiC Whiskers in Ceramic Matrix by Extrusion for Toughening Effect .....	72
3	Research Methodology.....	74
3.1	Manipulation and Alignment of SiC whiskers .....	74

3.1.1	Morphology of As-received SiC whiskers.....	74
3.1.2	Alignment Template .....	75
3.1.3	Tape Casting.....	77
3.1.4	Sintering of Aligned SiC Whiskers in Alumina Green Tape.....	80
3.2	Magnetron Sputtering Growth of GaN Thin Films.....	84
3.2.1	Sputtering System.....	84
3.2.2	Gallium Target Preparation and Target Container Selection .....	86
3.2.3	Substrate Heater.....	87
3.2.4	GaN Thin Film Growth Procedure .....	91
3.3	Characterization .....	92
3.3.1	XRD .....	92
3.3.2	SEM .....	95
3.3.3	STEM.....	96
4	Results and Discussion: Manipulation and Alignment of SiC Whiskers for GaN Thin Film Growth.....	99
4.1	Alignment of SiC Whiskers .....	99
4.2	Transfer of Aligned SiC Whiskers.....	106
4.3	Sintering Behavior of SiC Whiskers in Alumina Matrix .....	110
4.3.1	Development of Self-Regulating Sintering Technique of Random Silicon Carbide Whiskers in Alumina Matrix .....	111

4.3.2	Sintering of the Aligned SiC <sub>w</sub> by Self-regulating Sintering Technique	118
4.4	Study of GaN Thin Film Growth on SiC whiskers .....	121
5	Results and Discussion: Magnetron Sputtering Growth of GaN Thin Films	128
5.1	Control of Contamination in the Thin Film .....	129
5.1.1	Detection of Contamination.....	129
5.1.2	Removal of Contamination.....	134
5.2	Substrate Dependence.....	137
5.3	GaN Thin Film Growth on SiC Substrate in Ar and N <sub>2</sub> Atmosphere ....	140
5.3.1	XRD Studies of GaN Thin Films.....	140
5.3.2	Surface Morphology of GaN Thin Films .....	142
5.3.3	2D-XRD Pole Figures of GaN Thin Films.....	147
5.3.4	GaN/SiC Interfacial Structure and Chemical Composition .....	149
5.4	Effect of H <sub>2</sub> on GaN Thin Film Growth on SiC Substrate .....	154
5.4.1	XRD Studies of GaN Thin Films.....	155
5.4.2	Surface Morphology of GaN Thin Films .....	156
5.4.3	2D-XRD Pole Figures of GaN Thin Films.....	158
5.4.4	GaN/SiC Interfacial Structure and Chemical Composition .....	161
6	Conclusion.....	166
	References .....	170

## List of Figures

Figure 1-1. Color mixing of LED chips. (a) Current LED chips, note that color will change with viewing angle due to large size of chips; (b) Micron-wire LED chips, note that they can provide a more intimate color mixing than current LED chips. 2	
Figure 2-1. Evolution of visible LEDs [1].	8
Figure 2-2. Schematic band structure of GaAs, GaAsP, and GaP. Note that isoelectronic nitrogen doping level is also shown. The direct-indirect transition occurs when mole fraction of phosphorous is between 45-50% [53].	11
Figure 2-3. Peak emission energy versus alloy composition for undoped and nitrogen-doped GaAsP LEDs injected with a current density of 5 A/cm <sup>2</sup> at room temperature. The energy gap of the direct-to-indirect ( $E_{\Gamma}$ -to- $E_X$ ) transition is also shown [58].	12
Figure 2-4. External quantum efficiency of GaAsP based LEDs versus emission wavelength in nitrogen doped and undoped GaAsP [59].	13
Figure 2-5. Efficiency ratio between nitrogen-doped and undoped GaAsP versus phosphorus mole fraction at 300K [59].	14
Figure 2-6. The dependence of bandgap energy of $Al_xGa_{1-x}As$ on alloy composition $x$ . Note that there is a direct-indirect bandgap change at $x=0.45$ [62].	15
Figure 2-7. Band structure of AlGaAs/GaAs heterostructures designed for emission in red part of the visible light spectrum: (a) $Al_xGa_{1-x}As$ /GaAs quantum well with a thin GaAs well; (b) $Al_xGa_{1-x}As$ / $Al_yGa_{1-y}As$ ( $x > y$ ) double heterostructure with $Al_yGa_{1-y}As$ active region [63].	16

Figure 2-8. Bandgap energy and corresponding wavelength versus lattice constant of  $(\text{Al}_x\text{Ga}_{1-x})_y\text{In}_{1-y}\text{P}$  at 300 K. The vertical dashed line shows  $(\text{Al}_x\text{Ga}_{1-x})_{0.5}\text{In}_{0.5}\text{P}$  lattice matched to GaAs [69, 70]. ..... 18

Figure 2-9. Bandgap energy and emission wavelength of unordered AlGaInP lattice matched to GaAs at room temperature [71, 72]. Note that the direct-indirect bandgap transition point is  $x=53\%$  with corresponding wavelength  $\lambda=555\text{nm}$ . ..... 18

Figure 2-10. The relationship between bandgap energy and lattice constant of III-nitrides semiconductors (after [73-76]). ..... 21

Figure 2-11.  $I$ - $V$  characteristic of a p-n junction [78]. Note that  $I(\text{gen.})$  refers to the generation current whose magnitude depends on the generation rate of electron-hole pairs in the diode [78]...... 24

Figure 2-12. Current-voltage characteristics of p-n junctions based on different semiconductors at 295 K [79]. (a) Ge,  $E_g \approx 0.7 \text{ eV}$ ; (b) Si,  $E_g \approx 1.1 \text{ eV}$ ; (c) GaAs,  $E_g \approx 1.4 \text{ eV}$ ; (d) GaAsP,  $E_g \approx 2.0 \text{ eV}$ ; (e) GaInN,  $E_g \approx 2.9 \text{ eV}$  ..... 25

Figure 2-13. Chemical composition and energy band diagram of an AlGaAs quantum well structure, note the energy loss of carriers by the phonon emission [82]. ..... 27

Figure 2-14. Three major steps of LED manufacturing (reproduced from [83]). . 28

Figure 2-15. Stick-and-ball diagrams of wurtzite GaN[84]. ..... 37

Figure 2-16. The orientations which are commonly used in nitrides: the  $(11\bar{2}0)$  and  $(1\bar{1}00)$  planes and associated directions. The diagram is shown as a projection on the  $(0001)$  basal plane [84]. ..... 38

Figure 2-17. The bandgap nitrides, substrates commonly used for nitrides, and other conventional semiconductors versus their lattice constants (after [84]).....	40
Figure 2-18. First Brillouin zones of (a) the wurtzite and (b) the zincblende structures (after [84]). .....	42
Figure 2-19. Calculated band structures of (a) wurtzite GaN, (b) AlN, and (c) InN in the LDA within the FP-LMTO method (after [104]).....	43
Figure 2-20. Schematic of two-flow MOCVD system. a, set up of the MOCVD deposition system; b, principle of two flow reactor. (after [108]) .....	46
Figure 2-21. Surface processes during MBE growth: adsorption, desorption, surface diffusion, lattice incorporation, and decomposition (after [84]). .....	47
Figure 2-22. Nitride MBE growth system with a plasma nitrogen source (after [108]). .....	49
Figure 2-23. Schematic diagram of a planar diode rf reactive sputtering system for the deposition of GaN. The gallium source is a target consisting of a stainless steel cup filled with gallium. A mixture of molecular nitrogen and argon is used as nitrogen source and sputtering gas (rf plasma, 13.56 MHz) (after [134]).....	51
Figure 2-24. The surface SEM images of GaN layers grown at gas pressures of (a) 0.66, (b) 0.93, (c) 1.33, (d) 1.99 and (e) 2.66 Pa and 30% N <sub>2</sub> composition ratio in N <sub>2</sub> /Ar mixture source gas (after [135]).....	52
Figure 2-25. The SEM images of GaN layers grown at gas pressure of (a) 0.4, (b) 0.66, (c) 0.93 and (d) 1.33 Pa and 40% N <sub>2</sub> composition ratio in N <sub>2</sub> /Ar mixture source gas (after [135]).....	53
Figure 2-26. (a) XRRC from (0002) reflection. The inset shows the x-ray pole figure. (b) X-ray $\phi$ scan of the sputtered GaN (after [131]).....	54

Figure 2-27. The unit cell of sapphire: (a) rhombohedral unit cell; (b) hexagonal unit cell. Smaller spheres are for O and large ones are for Al (after [84, 136]). .. 56

Figure 2-28. perspective views in (2X2X1) unit cells: (a) along the  $[0001]$  direction in a rhombohedral unit cell; (b) along the  $[0001]$  direction in hexagonal unit cell. (After [84, 136])..... 57

Figure 2-29. Rhombohedral structure and surface planes of sapphire[140]. ..... 58

Figure 2-30. Projection of bulk basal plane sapphire and GaN cation positions for the observed epitaxial growth orientation. The circles mark Al-atom positions and the dashed lines show the sapphire basal plane unit cells. The open circles mark the N-atom positions and solid lines show the GaN basal plane unit cell. The Al atoms on the sapphire plane sit at positions approximately  $0.5 \text{ \AA}$  above and below the plane position [141]. ..... 61

Figure 2-31. a, tetragonal bonding of a carbon atom with its four nearest silicon neighbors. The bond lengths depicted with  $a$  and C-Si (the nearest neighbor distance) are approximately  $3.08$  and  $1.89 \text{ \AA}$ , respectively. b, three-dimensional structure of 2H-SiC structure[84]. ..... 64

Figure 2-32. Stacking sequence of 3C-, 2H-, 4H-, and 6H-SiC [159]. ..... 64

Figure 2-33.  $(11\bar{2}0)$  plane view of 3C-, 2H-, 4H-, and 6H-SiC polytypes [160]. .... 65

Figure 2-34. The perspective view along (a) the  $[001]$ , (b)  $[011]$ , and (c)  $[111]$  directions of a silicon cell [84]. ..... 67

Figure 2-35. Scanning electron micrographs of SiC whiskers produced by pyrolysis of rice hulls[5]..... 69

Figure 2-36. Cross-sectional view of whisker growth reactor[170]..... 71

Figure 2-37. Illustration of the VLS process for SiC whisker growth [170]. ..... 71

Figure 2-38. Scanning Electron Micrograph of SiC whisker grown by VLS process [170].	72
Figure 3-1. SEM images of as received SiC whiskers.	74
Figure 3-2. The concept of ceramic matrix embedded with aligned SiC whiskers.	75
Figure 3-3. Operation Principle of 3M Vikuiti™ BEF 90/24 [176].	76
Figure 3-4. a) Top view of 3M Vikuiti™ BEF; (b) Cross section view of 3M Vikuiti™ BEF; (c) Sketch of 3M BEF cross section.	77
Figure 3-5. Standard doctor blade assembly with adjustable blade [177].	80
Figure 3-6. Reactive DC-magnetron sputtering system for III-nitride thin films.	85
Figure 3-7. Design of substrate heater for GaN thin film growth.	88
Figure 3-8. The substrate heater for GaN thin films growth (modified from the design as show in Figure 3-7). a, the alumina crucible was placed in the tungsten heating basket as the insulation shield; b, the substrate holder.	90
Figure 3-9. Diffraction patterns in 3D space from a powder specimen and the diffractometer plane [179].	93
Figure 3-10. Five basic components in a 2D-XRD system: X-ray source; X-ray optics; goniometer and specimen stage; specimen alignment and monitor; area detector [180].	94
Figure 4-1. The aligned SiCw on the surface of 3M 90/24 BEF. The whiskers are driven down by gravity all the way to the bottom of the groove.	100
Figure 4-2. SiC whiskers on the surface of a plastic sheet template with wider parallel grooves and larger bottom angle than 3M BEF plastic sheet. Note that	

the whiskers on this template appear more randomly than whiskers on 3M as shown in Figure 4-1. ....	101
Figure 4-3. Set up for XRD characterization for the alignment degree of SiC whiskers (redrawn from [8]). ....	103
Figure 4-4. XRD pattern of aligned SiC whiskers. ....	103
Figure 4-5. Optical microscope image of the aligned SiC whiskers in latex rubber. ....	105
Figure 4-6. SEM images of aligned SiC whiskers in latex rubber. Note that the ridge of rubber latex corresponds to the bottom of the 3M BEF plastic sheet, thus the aligned whiskers stay on the ridge of rubber latex. Because the secondary electron images in SEM can only reflect topographic information, the amount of visible whiskers in SEM images is less than that in optical microscope images. ....	105
Figure 4-7. Optical microscope images of dried SiC whiskers on 3M BEF plastic sheet. Note that the whiskers stay aligned at the bottom of the parallel groove on 3M plastic sheet. ....	107
Figure 4-8. Tape-casted alumina green sheet on silicone-coated Mylar film. a, nano-alumina (45-55 nm APS powder, surface area = 30-40 m <sup>2</sup> /g) is the raw material; b, micron-alumina (<1 μm APS powder, surface area = 10 m <sup>2</sup> /g) is the raw material. ....	109
Figure 4-9. Optical microscope image of aligned silicon carbide whiskers in alumina green tape. The whiskers are aligned vertically in the image. ....	110
Figure 4-10. Top view drawing of the sintered pellet after grinding. Area1, sintered SiC whiskers in alumina matrix; area 2, mullite formed by sintering. ..	112
Figure 4-11. XRD patterns of the sintered pellet. ....	113

Figure 4-12. EDX line scan at the interface between  $\text{Al}_2\text{O}_3\text{-SiC}_w$  mixture and mullite. a. EDX line scan results shown in the electron image of the scanned area; EDX spectra of Si, C, Al, and O are shown below figure a, respectively. .... 115

Figure 4-13. EDX line scan at the interface between  $\text{Al}_2\text{O}_3\text{-SiC}_w$  mixture and mullite (different area from Figure 4-12). a. EDX line scan results shown in the electron image of the scanned area; EDX spectra of Si, C, Al, and O are shown below figure a, respectively. .... 116

Figure 4-14. a, Back scattered electron image. b, EDX mapping of silicon carbide whiskers in sintered pellet. Areas 1 are corresponding to SiC whiskers, and areas 2 are corresponding to alumina. .... 117

Figure 4-15. Schematic diagram of "Sandwich" structure of "self-protective" green pellet for aligned  $\text{SiC}_w$  sintering. Zone 1: mixture of  $\text{SiC}_w$  and  $\text{Al}_2\text{O}_3$  (weight ratio  $\text{Al}_2\text{O}_3/\text{SiC}_w=4$ ); Zone 2: Alumina green tape with aligned  $\text{SiC}_w$ . In order to show the details of the alumina tape, it is not drawn to scale. .... 120

Figure 4-16. a, BSE image of sintered alumina tape cross section; b, EDX mapping of the cross section of the sintered tape. Areas 1 are corresponding to the cross section of SiC whiskers, and areas 2 are corresponding to alumina. 120

Figure 4-17. BSE image of the cross section of SiC whiskers in alumina matrix and their corresponding EDX images/spectrum, the whiskers are labeled as 1, 2, 3, 4, and 5. a. BSE image; b. EDX mapping of whisker #2; c. EDX mapping of whisker #3; d. EDX mapping of whisker #4; e. EDX spectrum of whisker #1 (note that Al and O signals were also collected in this spectrum since the interaction volume of electron beam in the specimen is larger than whisker #1). .... 122

Figure 4-18. SEM images: a. SEI of ceramic substrate with aligned SiC whiskers; b. SEI of GaN grown on ceramic substrate (same area as figure a); c. BSE image of GaN grown on ceramic substrate. .... 124

Figure 4-19. XRD patterns of GaN thin films grown on ceramic substrate with (111)-oriented SiC whiskers. ....	126
Figure 4-20. Schematic drawing of GaN thin film growth on (111) oriented SiC whiskers embedded in alumina matrix.....	127
Figure 5-1. XRD patterns of GaN (#32, #33, and #34) grown on (0001)-oriented 6H-SiC substrates. ....	130
Figure 5-2. a, SEM image of GaN-#34 grown on (0001)-oriented 6H-SiC substrate; b, EDX point analysis spectrum of "spectrum 1" in the SEM image. ....	131
Figure 5-3. Residual gas mass spectra. a, gas mass spectrum at background pressure versus gas mass spectrum at the time when Ar was introduced; b, gas mass spectrum at background pressure versus gas mass spectrum at the time when N <sub>2</sub> was introduced. ....	132
Figure 5-4. a, SEM image of GaN-#42 grown on (111)-oriented Si substrate; b, EDX point analysis spectrum of "spectrum 1" in the SEM image. ....	133
Figure 5-5. Cu-Ga binary phase diagram[185]. ....	133
Figure 5-6. a, SEM image of Ga target carried by copper cup; b, EDX point analysis spectrum of "spectrum 1" in the SEM image.....	134
Figure 5-7. Smooth bore PTFE core stainless steel hose [187].....	135
Figure 5-8. Gas mass spectrum at background pressure versus gas mass spectrum at the time when Ar was introduced after polyethylene tubing was replaced by smooth bore PTFE core hose. ....	135
Figure 5-9. SEM image of GaN-#57 grown on (111)-oriented Si substrate after polyethylene tubing and copper cup were replaced; b, EDX point analysis spectrum of "spectrum 2" in the SEM image. Note that carbon peak in the	

spectrum is from the carbon coating for electrical conduction in SEM. No elements other than C, N, and Ga can be detected from the specimen. ....	136
Figure 5-10. XRD pattern of GaN-#57 grown on (111)-oriented Si substrate after polyethylene tubing and copper cup were replaced.....	137
Figure 5-11. XRD patterns of GaN-#57 grown on Si substrate and GaN-#58 grown on SiC substrate. ....	138
Figure 5-12. SEM images of GaN-#57 grown on Si substrate (a) and GaN-#58 grown on SiC substrate (b).....	139
Figure 5-13. XRD patterns of GaN thin films grown on 6H-SiC substrates with different thickness.....	141
Figure 5-14. XRRC of GaN-#61. FWHM of the peak is 50 arcmin.....	142
Figure 5-15. SEM micrographs of (a) GaN-#58 and (b) GaN-#61. ....	143
Figure 5-16. Grain size distribution of GaN-#58 and GaN-#61 according to SEM micrographs.....	144
Figure 5-17. A proposed pathway to hillock formation in the growth of GaN [189]. .....	145
Figure 5-18. Pole figures of GaN-#61 obtained by 2D-XRD. a, (0002) pole figure; b, $\{10\bar{1}1\}$ pole figure.....	147
Figure 5-19. HAADF micrographs of GaN-#58. a, GaN/SiC interface; b, as grown GaN thin film.....	149
Figure 5-20. Elemental profiles across GaN/SiC interface of GaN-#58 by EELS and HAADF image of scanned area. Ga L <sub>23</sub> edge, N K edge, Si L <sub>23</sub> edge, C K edge, and O K edge are used for each profile. Note that because the EELS spectral features of the Si L <sub>23</sub> edge and the Ga M <sub>23</sub> edge overlap, the Ga L <sub>23</sub>	

edge signal is used instead of the Ga M<sub>23</sub> edge signal to draw the Ga profile. The Si profile is obtained by the multiple linear least squares (MLLS) fitting from the overlapped Si L<sub>23</sub> edge and Ga M<sub>23</sub> edge peak. A chi-squared test was carried out to measure the degree of fitting, and a large difference between observed and expected outcome was found in the interface, which indicates the fitted Si profile in the interface is not accurate. .... 151

Figure 5-21. EELS spectra at GaN/SiC interface of GaN-#58. .... 153

Figure 5-22. XRD patterns of GaN-#61, GaN-#66, and GaN-#67. .... 155

Figure 5-23. SEM micrographs of GaN-#66(a) and GaN-#67(b). .... 156

Figure 5-24. Grain size distribution of GaN-#66 and GaN-#67. .... 157

Figure 5-25. Pole figures of GaN-#66 and GaN-#67 obtained by 2D-XRD. a, (0002) pole figure of GaN-#66; b, {10 $\bar{1}$ 1} pole figure of GaN-#66; c, (0002) pole figure of GaN-#67; d, {10 $\bar{1}$ 1} pole figure of GaN-#67. .... 158

Figure 5-26. a, simulated patterns of (0002) pole figure with all possible orientations; b, simulated patterns of {10 $\bar{1}$ 1} pole figure with all possible orientations. Black squares, black circles, gold squares, blue dots, and red squares correspond to the poles from (0002) oriented wurtzite GaN, {3 $\bar{3}$ 02} oriented wurtzite GaN, {111} oriented zinc-blende GaN, {511} oriented zinc-blende GaN, and 6H-SiC substrate, respectively. Note that {111} and {511} oriented zinc-blende GaN does not show up in {10 $\bar{1}$ 1} pole figures because the 2 $\theta$  range of {10 $\bar{1}$ 1} pole figures does not cover any reflections from the zinc-blende GaN... 159

Figure 5-27. a, ABF image of GaN/SiC interface of GaN-#66, note that the crystalline zone in native oxide layer is highlighted in a red rectangular; b, HAADF image of GaN/SiC interface of GaN-#66; c, ABF image of GaN/SiC interface of

GaN-#67; d, HAADF image of GaN/SiC interface of GaN-#67. Note that Figure c & d were taken on the same area simultaneously, Figure e & f were taken on the same area simultaneously. The crystallographic directions are identical in Figure a, b, c, d..... 162

Figure 5-28. a, elemental profiles across GaN/SiC interface of GaN-#66 by EELS and HAADF image of scanned area; b, elemental profiles across GaN/SiC interface of GaN-#67 by EELS and HAADF image of scanned area. Ga L<sub>23</sub> edge, N K edge, Si L<sub>23</sub> edge, C K edge, and O K edge are used for each profile. Note that because the EELS spectral features of Si L<sub>23</sub> edge and Ga-M<sub>23</sub> edge overlap, Ga L<sub>23</sub> edge signal are used instead of Ga M<sub>23</sub> edge signal to calculate Ga profile, Si profile are obtained by the MLLS fitting from the overlapped Si L<sub>23</sub> edge and Ga M<sub>23</sub> edge peak. Chi-squared test was carried out to measure the degree of fitting, and a large difference between observed and expected outcome was found at the interface, which indicates the fitted Si profile at the interface is not accurate..... 163

## List of Tables

Table 2-1. Development of group III nitrides (partially reproduced from [1]), the following abbreviations are used: low-energy electron beam irradiation (LEEBI), X-ray rocking curves (XRRC), multiple quantum wells (MQW), quantum wells (QW), single quantum well (SQW), double heterostructure (DH), continuous wave (c.w.).....	8
Table 2-2. Manufacturing steps associated with sapphire wafer (reproduced from [83]). .....	28
Table 2-3. GaN epitaxy growth details (reproduced from [83]). .....	31
Table 2-4. LED die fabrication after epitaxy growth (reproduced from [83]). .....	32
Table 2-5. LED packaging and assembly steps (reproduced from [83]). .....	34
Table 2-6. Measured and calculated constants of wurtzite AlN, GaN, and InN. (After [84], LDA: local density approximation; FP-LMTO: full-potential linear muffin-tin orbital; LEO: lateral epitaxial overgrowth) .....	38
Table 2-7. Calculated values of ionic radii (Å), effective charges (electrons), and the FIC for III nitrides (after [103]).....	41
Table 2-8. Properties of sapphire [136].....	59
Table 2-9. Crystallographic relationship between GaN film and sapphire substrates (reproduced from [136, 142]).....	60
Table 2-10. Properties of SiC at room temperature (reproduced from [136, 152]). .....	63
Table 2-11. Properties of Si at room temperature [136].....	67

Table 3-1. Tape casting batch formulation and corresponding function of each component..... 78

Table 5-1. Summary of GaN-#61 thin film orientation on 6H-SiC substrate. (w-GaN: wurtzite GaN; z-GaN: zinc-blende GaN) ..... 149

Table 5-2. Summary of GaN thin films orientations on 6H-SiC substrates for GaN-#66 and GaN-#67. (w-GaN: wurtzite GaN; z-GaN: zinc-blende GaN) ..... 160

## List of Flow Charts

Flow Chart 3-1. Manipulation and alignment of SiC whiskers.....	84
---	----

## List of Abbreviations and Symbols

2D-XRD	Two-dimensional X-ray Diffraction
ABF	Annular Bright Field
BEF	Brightness Enhancement Film
c.w.	Continuous Wave
CCFL	Cold-cathode Fluorescent Lamp
cd	Candela
DH	Double Heterostructure
DHTS	Double Heterostructure with a Transparent Substrate
DIPMeIn	Di-isopropylmethylindium
e	Electron
ECR	Electron Cyclotron Resonance
EDMIn	Ethyldimethylindium
EDX	Energy-dispersive X-ray Spectroscopy
EELS	Electron Energy-loss Spectroscopy
EFG	Edge-defined Film Fed Growth
EL	Electroluminescent
ELNES	Energy-loss Near Edge Structure
Eq.	Equation

fcc	Face-centered Cubic
FIB	Focused Ion Beam
FIC	Fractional Ionic Character
FP-LMTO	Full Potential-Linear Muffin-Tin Orbital
FWHM	Full Width at Half Maximum
GSM	Gradient Solidification Method
HAADF	High-angle Annular Dark-Field
HEM	Heat Exchanger Method
$I(\text{gen.})$	Generation Current
$I$ - $V$	Current-Voltage
LCD	Liquid Crystal Display
LDA	Local Density Approximation
LED(s)	Light-Emitting Diode(s)
LEEBI	Low-energy Electron Beam Irradiation
LPE	Liquide-phase Epitaxy
MBE	Molecular Beam Epitaxy
MLLS	Multiple Linear Least Squares
MOCVD	Metal-Organic Chemical Vapor Deposition
MOVPE	Metalorganic Vapour Phase Epitaxy

MQW	Multiple Quantum Well
$p$	Momentum
QW	Quantum Well
RF	Radio Frequency
SEI	Secondary Electron Image
SEM	Scanning Electron Microscopy/Microscope
SiC <sub>w</sub>	Silicon Carbide Whiskers
SQW	Single Quantum Well
SSD(s)	Solid State Display(s)
STEM	Scanning Transmission Electron Microscopy
TEC	Thermal Expansion Coefficient
TEIn	Triethylindium
TMAI	Trimethylaluminium
TMGa	Trimethylgallium
TMIn	Trimethylindium
VLS	Vapor-Liquid-Solid
$V_{th}$	Threshold Voltage
w-GaN	Wurtzite GaN
$x$	Position

XRD	X-ray Diffraction
XRRC	X-ray Rocking Curve
z-GaN	Zinc-blende GaN

# 1 Introduction

Light-emitting diode (LED)-based solid state displays (SSDs) have attracted growing interest due to their advantages in terms of greater color contrast ratio, higher brightness, larger viewing angle, higher power efficiency, less response time, and smaller display panel thickness compared to current liquid crystal displays (LCDs) as the liquid crystal filters the light emitted from a backlight. GaN-based III-nitrides ( $\text{In}_x\text{Ga}_{1-x}\text{N}$ ) are essential for highly efficient LEDs due to their wide direct bandgap (up to 3.4eV when  $x=0$  [1]) and high internal quantum efficiency [2]. By tuning the indium concentration in InGaN/GaN quantum wells, emission spectra of GaN-based LEDs can be extended from the UV wavelength range to cover the full visible spectrum [1]. Thus, III-nitrides are highly qualified materials selection for LED-based SSDs. However, commercially available III-nitride thin films are most often grown by metal-organic chemical vapor deposition (MOCVD) methods on 4-6" sapphire wafers. These sapphire wafers are cut from large single crystal boules of sapphire by a diamond wire saw. An additional dicing and binning step must take place after the thin film growth to yield LED chips ready for packaging [3]. As a result, the large size (typically 250  $\mu\text{m}$  X 250  $\mu\text{m}$  or larger) and costly manufacturing process of LED chips [4] limit the potential uses of LEDs as the pixels of SSDs except for large and low-resolution display screens.

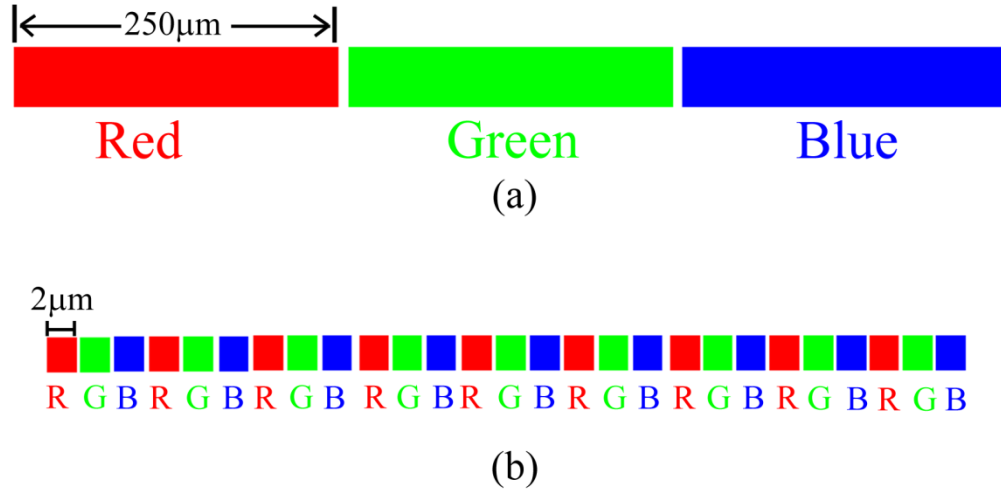


**Figure 1-1. Color mixing of LED chips. (a) Current LED chips, note that color will change with viewing angle due to large size of chips; (b) Micron-wire LED chips, note that they can provide a more intimate color mixing than current LED chips.**

Micron LED chips which are much smaller than currently available LED chips are required to realize the concept of SSD for a uniform color mixing at all viewing angles by a intimate mixing of different LED colors as shown in Figure 1-1. 3C-SiC single crystal whiskers are of particularly suitable to be the substrates for III-nitrides epitaxial growth of micron LED chips. Produced by a cost-effective thermal reduction method [5], SiC whiskers have a diameter of  $1.5\mu\text{m}$  and a length of  $18\mu\text{m}$  on average. The (111) planes of the whiskers, which are perpendicular to the length of the whiskers, are equivalent to (0001) planes of 4H and 6H-SiC, and all of them have the smallest lattice mismatch ( $\sim 3\%$ ) and thermal expansion coefficient (TEC) difference ( $\sim 25\%$ ) as compared to GaN

among other major GaN heteroepitaxial growth substrates including sapphire and silicon. By taking the advantage of silicon carbide whiskers' smaller size compared to large single crystal wafers, together with the conductive nature of SiC, the as-grown micron-size GaN on (111) planes of SiC whiskers can be chosen as building blocks for full color solid state high definition displays/TVs. Thus, to achieve the GaN growth on (111) planes of SiC whiskers, the precise alignment of SiC whiskers are of particularly important. The as-received randomly distributed SiC whiskers need to be precisely lined up and cautiously transferred into a rigid and high-temperature compatible matrix for GaN growth at an elevated temperature in vacuum, which remains challenge and complex because the currently alignment techniques such as extrusion, cold pressing, tape casting, and roll forming, cannot reach a degree of alignment which is suitable for semiconductor thin film epitaxial growth, so it is desirable to develop a new method for the precise alignment of SiC whiskers. On the other hand, from GaN thin film growth point of view, sputtering is a convenient and inexpensive growth method compared with MOCVD and molecular beam epitaxy (MBE) [6], and is quite attractive due to its versatility and scalability for the large scale GaN thin film growth on the matrix of aligned (111) oriented SiC whiskers in large scale production [7]. However, sputtering growth of GaN directly on SiC has rarely been investigated, and the growth conditions for high quality GaN thin films on SiC substrates by sputtering are still unclear.

The general objectives of this thesis are to focus on two aspects for the GaN thin films growth on the matrix of aligned (111) oriented SiC whiskers: (1) to develop a new method including a series of steps for the precise alignment of random SiC whiskers and cautious transfer of the aligned SiC whiskers into a suitable matrix; (2) to investigate the sputtering growth behavior of high quality GaN thin films directly grown on SiC substrates. For aspect (1), the precise alignment of the whiskers is achieved on a patterned 3M Vikuiti™ Brightness Enhancement Film surface with a higher degree of alignment than that achieved by extrusion [8]. The aligned whiskers are then transferred into alumina matrix by tape casting alumina green tape directly on the 3M film with aligned SiC whiskers. A self-regulating technique is also developed to protect the aligned SiC whiskers from being oxidized by sintering in air. After a series of steps of alignment and manipulation, aligned SiC whiskers are successfully embedded rigidly in an alumina matrix. In terms of aspect (2), a reactive DC-magnetron sputtering system is built for GaN thin film growth. (0001)-oriented 6H-SiC wafers are employed as the prototype of the newly developed (111)-oriented 3C-SiC whiskers, since the GaN thin films grown on a bulk substrate can be characterized by X-ray diffraction (XRD), scanning electron microscopy (SEM), and scanning transmission electron microscopy (STEM) comfortably. High quality GaN thin films have been epitaxially grown on 6H-SiC by this technique successfully. The GaN thin films and GaN/SiC interface have been characterized

by XRD, SEM and STEM, and the corresponding mechanism is also investigated. This effort on the GaN epitaxial growth on 6H-SiC single crystal wafers points to a promising way for future work on cost-effective GaN epitaxial growth on aligned (111)-oriented SiC whiskers.

The structure of this thesis is illustrated as follows. The related background, necessary fundamental knowledge, and systematic reviews of previous work are elaborated in Chapter 2. Chapter 3 describes the experimental and characterization methods which are employed in this work. The new alignment and manipulation approaches of SiC whiskers are described in a series in Chapter 4. Following that, the investigation of the sputtering growth behavior of high quality GaN thin films directly on 6H-SiC substrates is systematically illustrated in Chapter 5. The conclusions are drawn and the proposed future work are elaborated in Chapter 6.

## 2 Literature Review

### 2.1 Overview: LEDs

#### 2.1.1 Brief History of LEDs

Discovered in 1907 by accident [9], the LED has become an efficient electroluminescent (EL) device. Independent Russian scientist Oleg Vladimirovich Losev also discovered glow from a zinc oxide and silicon carbide crystal rectifier diode [10] in the mid 1920s. The first modern LED, which was an infrared one, was developed by Bob Biard and Gary Pittman at Texas Instruments in 1961, as they realized that the zinc-diffused area of a semi-insulating GaAs substrate can give off infrared light [11]. The first visible red light LED was created by Nick Holonyack Jr. in 1962, and GaAsP on a GaAs substrate was used for this work. Also by using GaAsP, M. George Craford developed the first yellow LED at Monsanto in 1972. By the 1990s, red-to-yellow light LEDs had become commercially available [1].

It was not easy to develop short wavelength LEDs. SiC used to be a candidate for short wavelength LEDs but was abandoned later due to its low efficiency arising from its indirect bandgap. A II-VI semiconductor system, based on ZnSe, is another candidate for green and blue light LEDs. However, structural defects, which can reduce the quantum efficiency dramatically, are quite easy to be generated in ZnSe. As a result, this diminished the commercial application

potential of II-VI systems. The III-Nitride system, which features a wide distribution of direct bandgaps of AlN (6.2 eV), GaN (3.4 eV) and InN (0.65 eV), has proven itself for green and blue light LEDs. The bandgaps of the III-nitride system can be tuned from 0.65 eV to 6.2 eV by alloying those three nitrides. This wide distribution of bandgaps covers the infrared to ultra violet portion of the electromagnetic spectrum, so the entire visible light spectrum is covered by the III-nitride alloys. With the breakthrough of p-type GaN [12], blue and green ray LEDs based on III-nitride became possible.

Luminous efficacy, a ratio of luminous flux (luminous flux differs from radiant flux in that luminous flux reflects the varying sensitivity of the human eye to different wavelengths) to power, is a measurement of how well a light source produces visible light. A lumen is the luminous flux intensity within unit solid angle of a point source with luminous intensity of one candela (cd). A traditional incandescent tungsten filament lamp can emit about 20 lm/W in efficiency. In 1970s, the efficiency of LEDs was inferior than that of incandescent tungsten filament lamps, so the latter became a point of reference for LED efficiency. High efficiency red, yellow and orange LEDs had been achieved by AlInGaP/GaP by the 1990s [13-17]. The efficacy of blue and green LEDs has been increased by the development of GaN and InGaN, which is summarized in Table 2-1 [1].

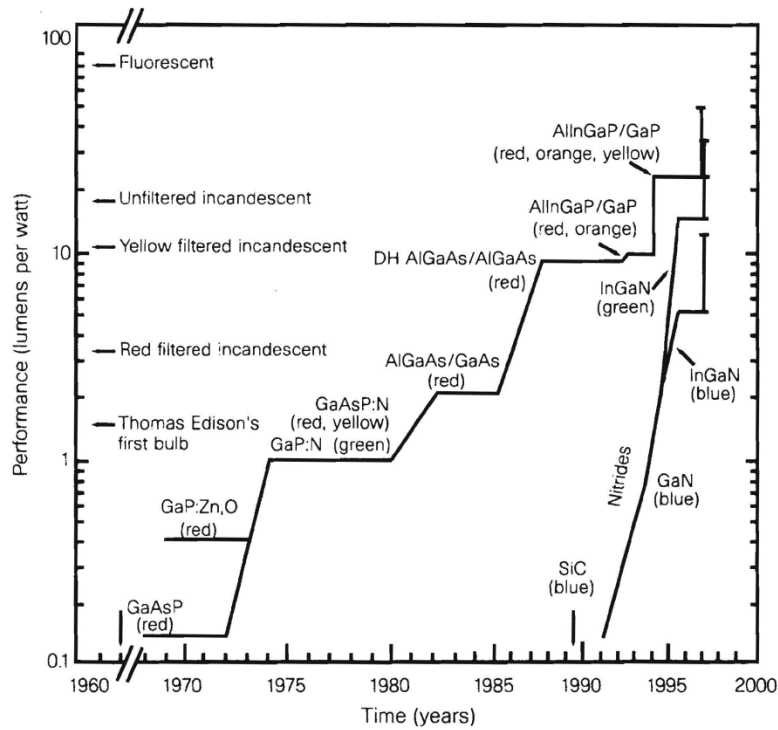


Figure 2-1. Evolution of visible LEDs [1].

Table 2-1. Development of group III nitrides (partially reproduced from [1]), the following abbreviations are used: low-energy electron beam irradiation (LEEBI), X-ray rocking curves (XRRC), multiple quantum wells (MQW), quantum wells (QW), single quantum well (SQW), double heterostructure (DH), continuous wave (c.w.).

Year	Event	Authors	Reference
1969	GaN by hydride vapour phase epitaxy	Maruska and Tietjen	[18]
1971	Metal-insulator-semiconductor LEDs	Pankove <i>et al.</i>	[19]
	GaN by MOCVD	Manasevit <i>et al.</i>	[20]
	Ultraviolet stimulated emission at 2K	Dingle <i>et al.</i>	[21]

<b>1974</b>	GaN by sublimation	Matsumoto and Aoki	[22]
	GaN by MBE	Akasaki and Hayashi	[23]
<b>1975</b>	AlN by reactive evaporation	Yoshida <i>et al.</i>	[24]
<b>1982</b>	Synthesis (high pressure)	Karpinski <i>et al.</i>	[25]
<b>1983</b>	AlN intermediate layer (MBE)	Yoshida <i>et al.</i>	[26]
<b>1986</b>	Specular films using AlN buffer layers	Amano <i>et al.</i>	[27]
<b>1989</b>	p-type doping with Mg and LEEBI	Amano <i>et al.</i>	[28]
	GaN p-n junction LED	Amano and Akasaki	[28]
	InGaN epitaxy (XRRC = 100 arcmin)	Nagamoto <i>et al.</i>	[29]
<b>1991</b>	GaN buffer layer by MOCVD	Nakamura	[30]
<b>1992</b>	Mg activation by thermal annealing	Nakamura	[12]
	High-brightness AlGaIn ultraviolet/blue LED (1.5%)	Akasaki and Amano	[31]
	InGaIn epitaxy (XRRC = 5 arcmin)	Nagamoto <i>et al.</i>	[32]
	High-brightness AlGaIn ultraviolet LEDs	Akasaki <i>et al.</i>	[31]
<b>1993</b>	InGaIn MQW structure	Nakamura <i>et al.</i>	[33]
	InGaIn/AlGaIn DH blue LEDs (1cd)	Nakamura <i>et al.</i>	[34]
<b>1994</b>	InGaIn/AlGaIn DH blue-green LEDs (2 cd)	Nakamura <i>et al.</i>	[35]
<b>1995</b>	InGaIn QW blue, green and yellow LEDs	Nakamura <i>et al.</i>	[36]
	InGaIn SQW green LEDs (10 cd)	Nakamura <i>et al.</i>	[37]
	Blue laser diode, pulsed operation	Nakamura <i>et al.</i>	[38]
<b>1996</b>	Ultraviolet laser diode	Akasaki <i>et al.</i>	[39]

---

	Blue laser diode, pulsed operation	Itaya <i>et al.</i>	[40]
	Blue laser diode, c. w. operation	Nakamura <i>et al.</i>	[41]
<b>2002</b>	High efficiency white light LEDs	Shimizu	[42]
<b>2010</b>	LED efficacy reaches 100 lm/w	Cree	[43]
<b>2013</b>	LED efficacy reaches 140 lm/w	Philips	[44]
<b>2013</b>	Direct observation of Auger emission of LEDs	Iveland <i>et al.</i>	[45]

---

## 2.1.2 Semiconductor Materials for LEDs

### 2.1.2.1 GaAsP: N, GaP: N, GaAsP, and GaP

GaAs<sub>1-x</sub>P<sub>x</sub> became available in 1960s, as one of the pioneering material systems for visible light LEDs [46-51]. The bandgap of GaAs is 1.424 eV, which can be increased by addition of phosphorus in the GaAs, so the emission wavelength of GaAs can be tuned from 870 nm to the visible light wavelength range. The lattice mismatch between GaAs and GaP is large (about 3.6%), so if we add more phosphorous into GaAs, the density of misfit dislocations will increase, then the luminescence efficiency will be reduced by non-radiative recombination of carriers [52]. Even with the assistance of a buffer layer, the density of dislocations cannot be dropped down to a sufficiently low level. Thus, GaAsP LEDs are mainly employed in low-brightness applications.

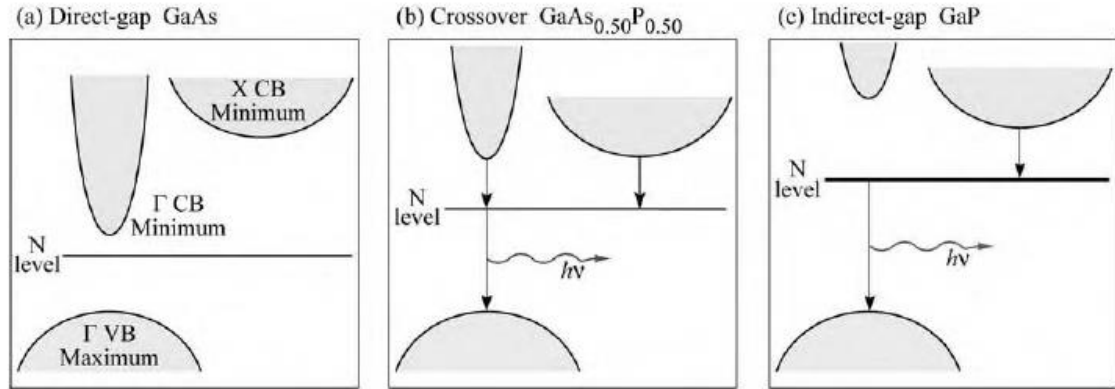


**Figure 2-2. Schematic band structure of GaAs, GaAsP, and GaP. Note that isoelectronic nitrogen doping level is also shown. The direct-indirect transition occurs when mole fraction of phosphorous is between 45-50% [53].**

In Figure 2-2, bandgap structure of GaAs, GaAsP, and GaP is shown. Nitrogen, is frequently doped as an isoelectronic impurity in GaAsP and GaP LEDs [54-60]. The electronic wave function of the isoelectronic impurity is restricted in position (small  $\Delta x$ ), thus the wave function is delocalized in k space (large  $\Delta p$ ) according to Heisenberg's uncertainty principle. This paved a way for electrons to make a transition from the X valley of the conduction band to the central  $\Gamma$  valley of the valence band, as the electron can be trapped by the isoelectronic nitrogen impurity atom. On the other hand, reabsorption effects are less significant in nitrogen-doped GaAsP compared with band-edge emission based LEDs, as the emission energy of nitrogen doped GaAsP is 50-150 meV less than the bandgap of the semiconductor matrix as shown in Figure 2-3. If we control the nitrogen doping in the active region, which is limited within the carrier diffusion lengths

from the junction plane, then the reabsorption of light by nitrogen impurities can be confined to the active region and the quantum efficiency of GaAsP based LEDs can be improved [59].

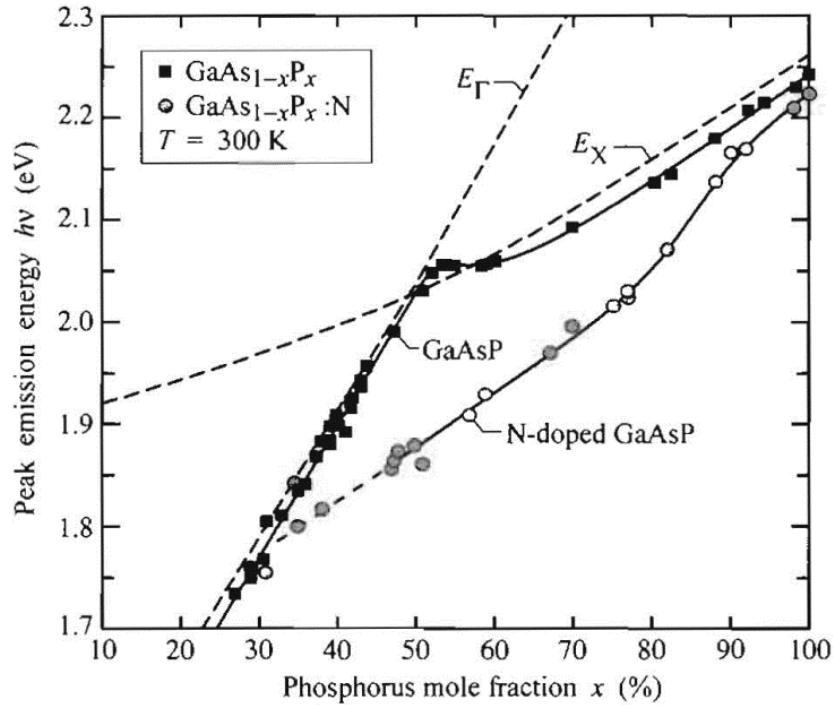


**Figure 2-3. Peak emission energy versus alloy composition for undoped and nitrogen-doped GaAsP LEDs injected with a current density of 5 A/cm<sup>2</sup> at room temperature. The energy gap of the direct-to-indirect ( $E_{\Gamma}$ -to- $E_{\chi}$ ) transition is also shown [58].**

The relationship between external quantum efficiency of GaAsP and emission wavelength is shown in Figure 2-4 [59]. The efficiency of nitrogen doped GaAsP is higher than undoped GaAsP over the whole investigated color range (red to green), especially in the orange, yellow, and green wavelength range. The

dependence of the undoped and nitrogen-doped GaAsP LEDs efficiency ratio on the phosphorous mole fraction in GaAsP has also been investigated. The curve shown in Figure 2-5 demonstrates that nitrogen-doped GaAsP based devices performs more efficiently than undoped GaAsP based devices over the whole composition range. However, due to the limited solubility of nitrogen in GaP, the efficiency of green LEDs based on GaP: N is low, and indicator lamps is the main application of this device [61].

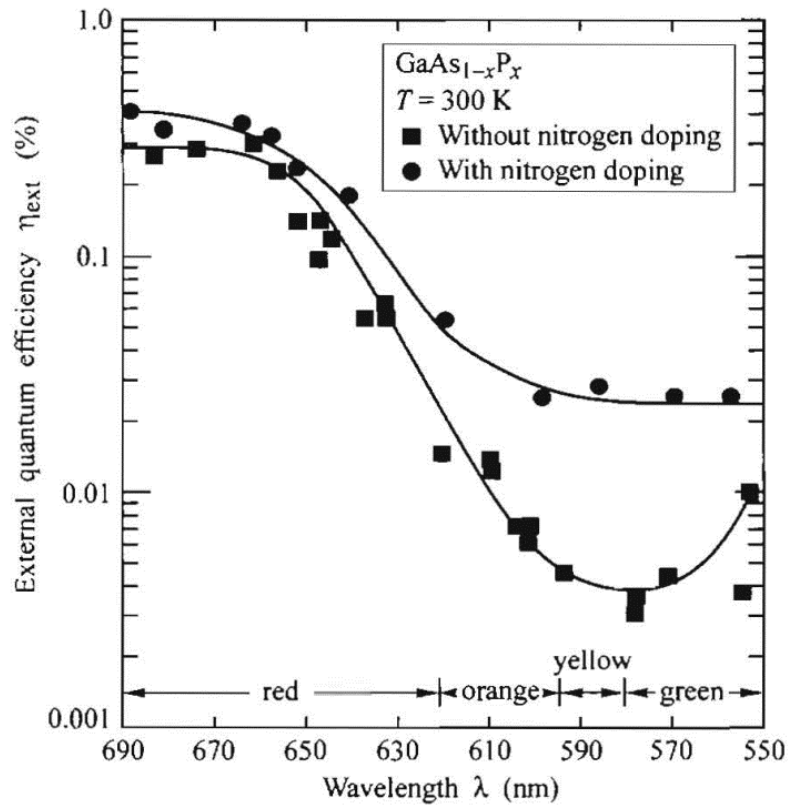


Figure 2-4. External quantum efficiency of GaAsP based LEDs versus emission wavelength in nitrogen doped and undoped GaAsP [59].

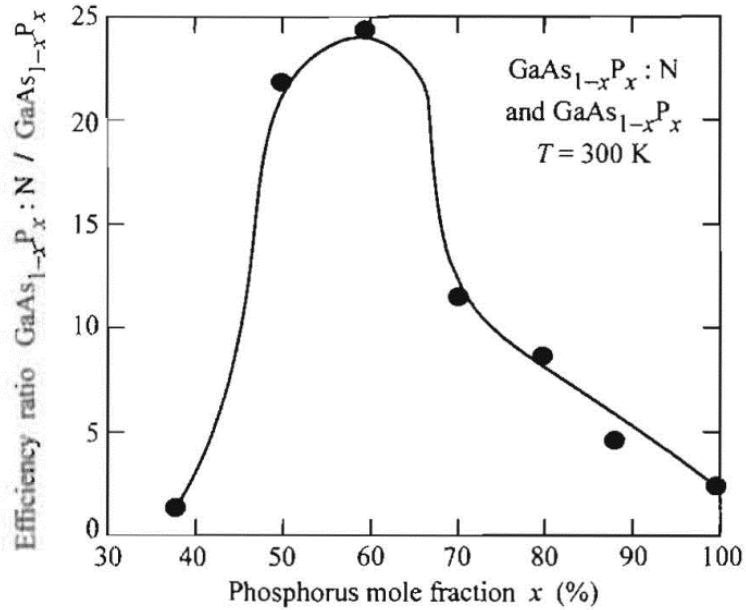
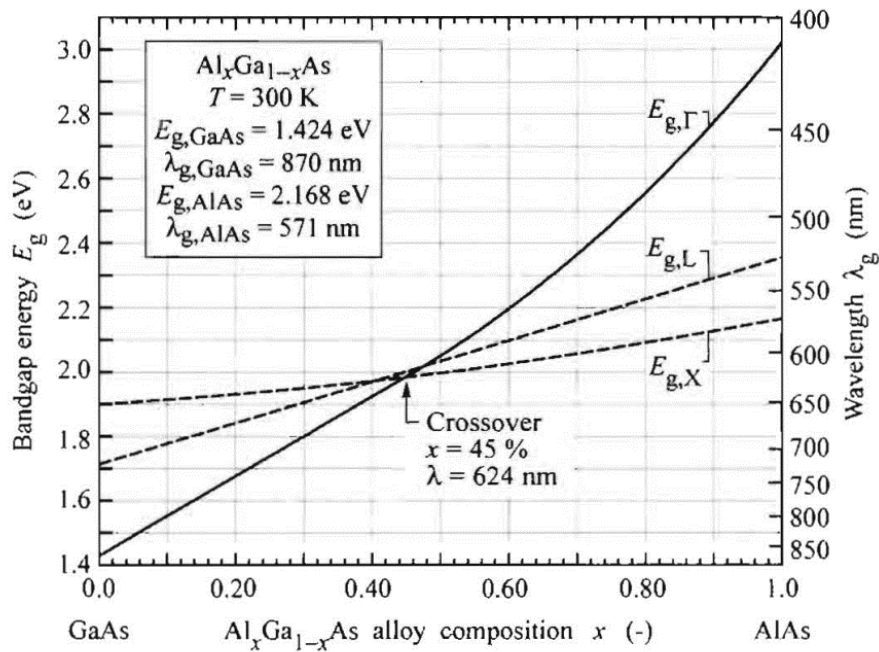


Figure 2-5. Efficiency ratio between nitrogen-doped and undoped GaAsP versus phosphorus mole fraction at 300K [59].

### 2.1.2.2 AlGaAs/GaAs

As the first materials system for high-brightness LEDs,  $\text{Al}_x\text{Ga}_{1-x}\text{As}/\text{GaAs}$  was developed in the 1970s and early 1980s.  $\text{Al}_x\text{Ga}_{1-x}\text{As}$  is lattice matched to GaAs due to the very slight atomic radii difference between Al (1.82 Å) and Ga (1.81 Å). When Al mole fraction  $x$  is less than 0.45,  $\text{Al}_x\text{Ga}_{1-x}\text{As}$  is a direct bandgap semiconductor as shown in Figure 2-6. The corresponding emission wavelength of  $x=0.45$  is 624 nm. Thus this materials system is suitable for high-brightness red light LEDs.



**Figure 2-6.** The dependence of bandgap energy of  $\text{Al}_x\text{Ga}_{1-x}\text{As}$  on alloy composition  $x$ . Note that there is a direct-indirect bandgap change at  $x=0.45$  [62].

To increase the efficiency of the AlGaAs materials system,  $\text{Al}_x\text{Ga}_{1-x}\text{As}/\text{GaAs}$  quantum well and  $\text{Al}_x\text{Ga}_{1-x}\text{As}/\text{Al}_y\text{Ga}_{1-y}\text{As}$  ( $x > y$ ) double heterostructures were employed. The band structures of these two structures are shown in Figure 2-7. A very thin GaAs quantum well is needed to create a size quantization effect and to make the energy states within the quantum well discrete by a sizing effect [63]. This can increase the emission energy, but the approach to making a very thin GaAs quantum well is technically challenging. The most efficient AlGaAs red light LEDs are based on  $\text{Al}_x\text{Ga}_{1-x}\text{As}/\text{Al}_y\text{Ga}_{1-y}\text{As}$  ( $x > y$ ) double heterostructure together with a transparent substrate (DHTS) [64-66]. These high efficiency LEDs are

grown on a temporary GaAs substrate, which will be polished and etched away after growth to avoid the reabsorption issue. The composition of the confinement layer of the heterostructure is  $x > 0.6$ , and the active layer for red LEDs with composition  $x = 0.35$  in the middle is sandwiched by lower and upper confinement layer. As the emission of AlGaAs DH-TS LEDs can be clearly visible under bright ambient conditions, they have become the first suitable LEDs for traffic lights and automotive brake lights [67].

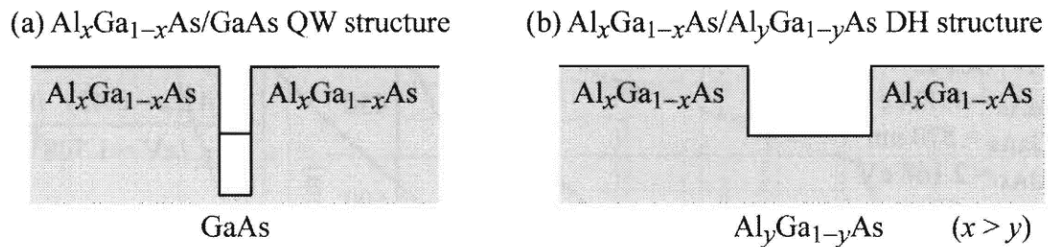


**Figure 2-7. Band structure of AlGaAs/GaAs heterostructures designed for emission in red part of the visible light spectrum: (a)  $\text{Al}_x\text{Ga}_{1-x}\text{As}/\text{GaAs}$  quantum well with a thin GaAs well; (b)  $\text{Al}_x\text{Ga}_{1-x}\text{As}/\text{Al}_y\text{Ga}_{1-y}\text{As}$  ( $x > y$ ) double heterostructure with  $\text{Al}_y\text{Ga}_{1-y}\text{As}$  active region [63].**

AlGaAs DH-TS LEDs require thick confinement layers (125  $\mu\text{m}$ ), which can be grown by liquid-phase epitaxy (LPE) at a high growth rate. Since the oxidation and corrosion problems of AlGaAs layers (mainly induced by the content of Al in the confinement layers), the reliability and lifetime of AlGaAs devices are lower than AlGaInP devices, as the latter do not contain any AlGaAs. The details of AlGaInP devices will be described in Section 2.1.2.3.

### 2.1.2.3 AlGaInP/GaAs

As today's primary material system for high-brightness LEDs in the long-wavelength part of the visible spectrum, the AlGaInP/GaAs material system was developed in 1980s and 1990s. The lattice constant of AlGaInP can be tuned in this way to match the lattice constant of a GaAs substrate: Ga atoms are partially replaced by larger In atoms, and As atoms are fully replaced by smaller P atoms, then GaInP is formed. The lattice of  $\text{Ga}_{0.5}\text{In}_{0.5}\text{P}$  is matched to GaAs at this specific composition. If the Ga atoms in  $\text{Ga}_{0.5}\text{In}_{0.5}\text{P}$  are partially replaced by Al atoms whose atomic radius is similar to Ga to form  $(\text{Al}_x\text{Ga}_{1-x})_{0.5}\text{In}_{0.5}\text{P}$ , it is also lattice matched to GaAs. The bandgap energy and corresponding wavelength versus lattice constant of  $(\text{Al}_x\text{Ga}_{1-x})_y\text{In}_{1-y}\text{P}$  at 300 K is shown in Figure 2-8. The direct-indirect transition point of  $(\text{Al}_x\text{Ga}_{1-x})_{0.5}\text{In}_{0.5}\text{P}$  is  $x=0.53$  as shown in Figure 2-9, and the corresponding bandgap energy is 2.33 eV. In the long wavelength range of red, orange, amber, and yellow, the AlGaInP material system is suitable for high-brightness LEDs [68].

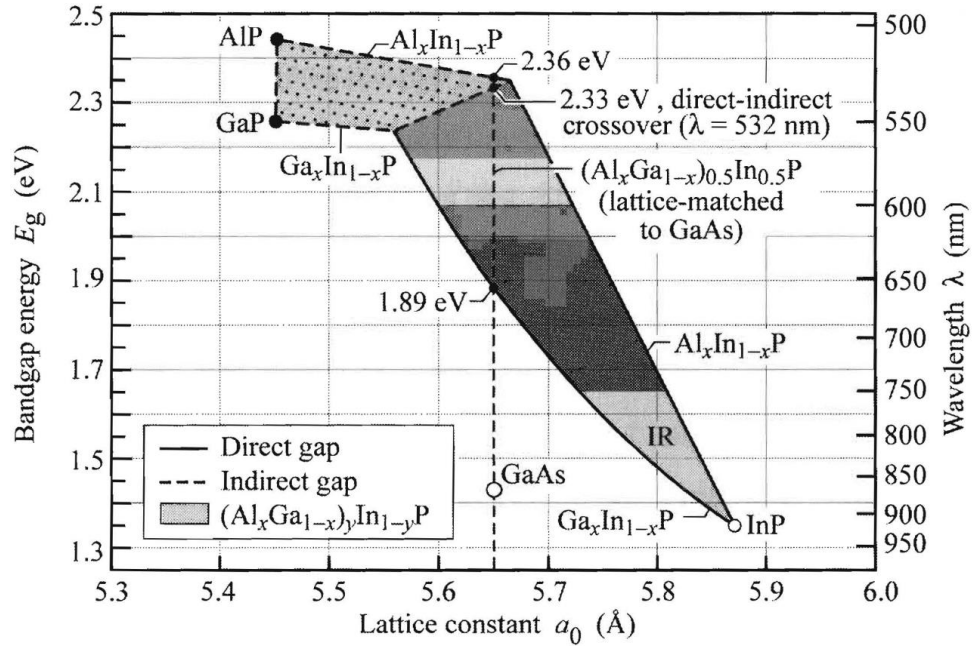


Figure 2-8. Bandgap energy and corresponding wavelength versus lattice constant of  $(Al_xGa_{1-x})_yIn_{1-y}P$  at 300 K. The vertical dashed line shows  $(Al_xGa_{1-x})_0.5In_{0.5}P$  lattice matched to GaAs [69, 70].

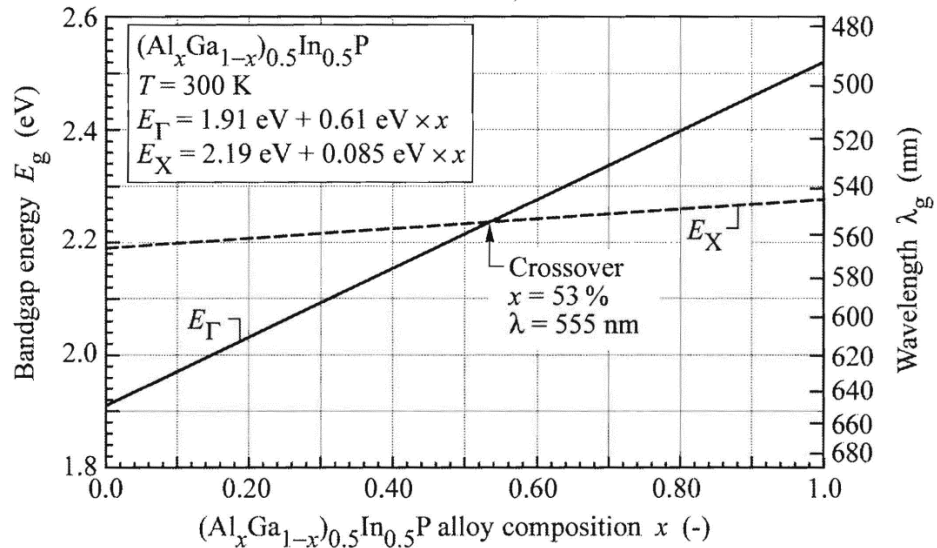


Figure 2-9. Bandgap energy and emission wavelength of unordered AlGaInP lattice matched to GaAs at room temperature [71, 72]. Note that the direct-indirect bandgap transition point is  $x=53\%$  with corresponding wavelength  $\lambda=555\text{nm}$ .

#### 2.1.2.4 GaInN

According to the discussion in the sections above, suitable materials system was still not available for high efficiency blue and green LEDs before the 1990s. Nitrogen doped GaP based green light LEDs can only be used as indicator lamps due to their low brightness. Although SiC blue LEDs became available, their efficiencies are much lower than AlGaInP based LEDs [1]. In 1992, Nakamura et al. successfully solved the activation problem of Mg doping in GaN by thermal annealing [12], which paved a way for the mass production of III-nitride based high brightness blue and green LEDs. Then the first commercially available III-nitride based blue LEDs with an InGaN/AlGaIn double heterostructure was fabricated by Nichia in 1994. The peak wavelength was 450 nm and the external quantum efficiency was 5.4%.

From the bandgap point of view, III nitride compounds are ideal semiconductor materials for short wavelength LEDs. As shown in Figure 2-10, the bandgap emission of  $\text{Ga}_x\text{In}_{1-x}\text{N}$  alloys can cover the electromagnetic spectrum from ultraviolet (3.4 eV of GaN) to infrared (0.8 eV of InN). On the other hand, the chemical bonding within the III-nitride system is strong, and thus intense light illumination and high electric current cannot easily degrade the quality of III-nitride thin films in use[1]. Since inexpensive GaN substrates are still not available, the epitaxial growth of GaN thin films relies on foreign substrates such

as sapphire and SiC. Quite a high density of misfit dislocations ( $10^7$ - $10^{10}$  cm<sup>-2</sup>) can be induced by the lattice constant as well as a linear thermal expansion coefficient mismatch between GaN epilayers and substrates. However, unlike III-V arsenide and III-V phosphide materials, the luminescent efficiency of III-nitride based LEDs can stay high even with those misfit dislocations. It is believed that carriers can be prevented from reaching dislocations by being localized in the potential minima, which is related to the fluctuation of indium in InGaN. In GaN and InGaN, the diffusion length of holes is small and thus not all of the holes can reach dislocations during recombination. The detailed aspects of III-nitride semiconductors will be discussed in Section 2.2.

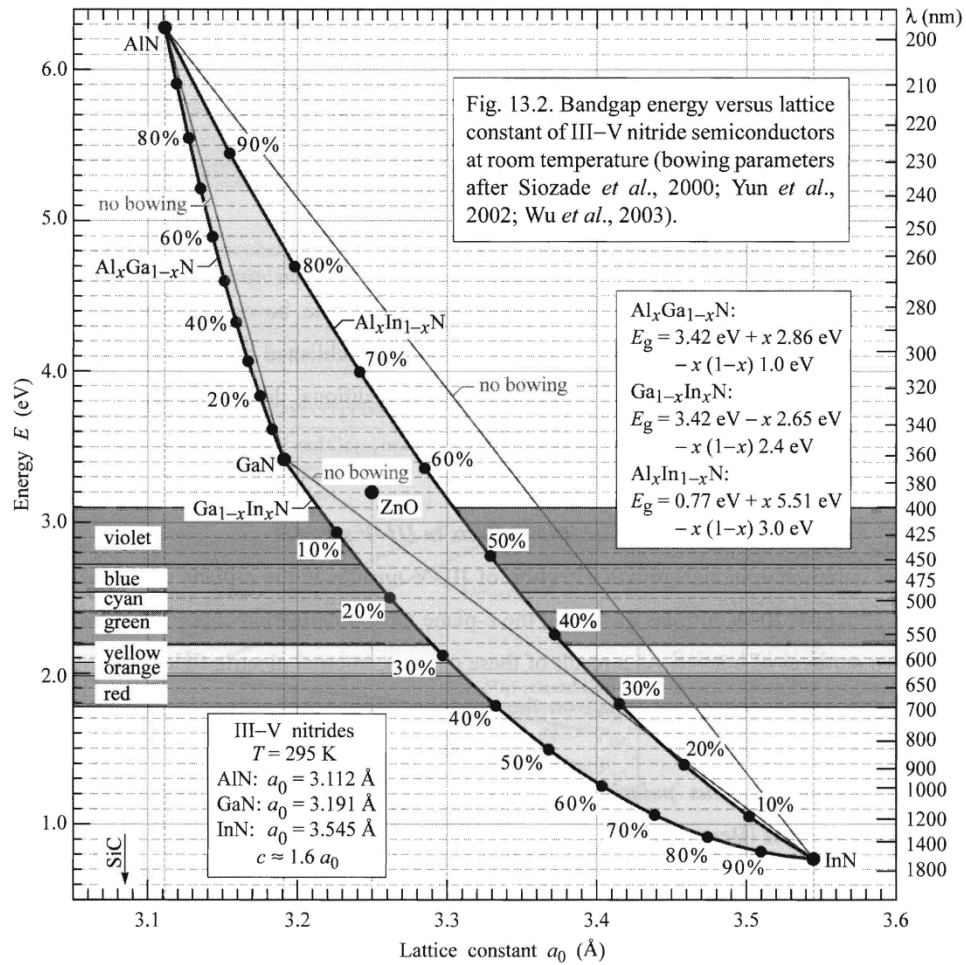


Figure 2-10. The relationship between bandgap energy and lattice constant of III-nitrides semiconductors (after [73-76]).

### 2.1.3 Electrical properties of P-N junctions

#### 2.1.3.1 Current-voltage Characteristic of Diode

A p-type semiconductor with donor concentration of  $N_D$  and n-type semiconductor with acceptor concentration of  $N_A$  are employed to form an abrupt p-n junction

[77]. Upon joining of the two types of semiconductors, the diffusion of carriers will take place, resulting from large carrier concentration gradients at the junction. The electrons diffusing from n to p will leave behind uncompensated positive donor ions in the n-type semiconductor, while the holes diffusing from p to n will leave behind uncompensated acceptors. As a result, an electric field, directed from the n-side to the p-side of the p-n junction, is built up in the p-n junction by diffusion of carriers. This region is depleted of free carriers since the direction of electric field in this region is opposite to the diffusion current. Thus, this region is called a depletion region, and it creates a potential barrier which is called the diffusion voltage,  $V_D$ , given by

$$V_D = \frac{kT}{e} \ln \frac{N_A N_D}{n_i^2} \quad (2.1)$$

where  $n_i$  is the intrinsic carrier concentration. The depletion layer width can be calculated by

$$W_D = \sqrt{\frac{2\varepsilon}{e} (V_D - V) \left( \frac{1}{N_A} + \frac{1}{N_D} \right)} \quad (2.2)$$

where  $\varepsilon$  is the dielectric permittivity of the semiconductor, and  $V$  is the bias voltage of the diode. When the diode is forward biased, electrons will be injected into the p-type region, and holes will be injected into the n-type region. As a result, the carriers will recombine with the opposite type of carriers in the region to which they diffuse. For example, one electron can recombine with a hole by emitting a

photon. This is the principle of LEDs. The current-voltage ( $I$ - $V$ ) relationship of a p-n junction is given by Shockley equation as

$$I = eA \left( \sqrt{\frac{D_p}{\tau_p}} \frac{n_i^2}{N_D} + \sqrt{\frac{D_n}{\tau_n}} \frac{n_i^2}{N_A} \right) \left( e^{eV/kT} - 1 \right) \quad (2.3)$$

Where  $A$  is the cross section area of the diode,  $D_n$  and  $D_p$  are the diffusion coefficients of the electrons and holes, and  $\tau_n$  and  $\tau_p$  are the minority-carrier lifetimes of electrons and holes, respectively.

When the diode is under typical forward bias ( $V \gg kT/e$ ),  $\exp(eV/kT) - 1 \approx \exp(eV/kT)$  the Shockley equation can be converted, by using Eq. (2.1), as

$$I = eA \left( \sqrt{\frac{D_p}{\tau_p}} N_A + \sqrt{\frac{D_n}{\tau_n}} N_D \right) e^{e(V-V_D)/kT} \quad (2.4)$$

When  $V \geq V_D$ , the current starts to increase exponentially with voltage. Thus,  $V_D$  is also called threshold voltage ( $V_{th}$ ) of the diode, as  $V_{th} \approx V_D$ .

Furthermore, when a diode is under zero bias,

$$E_g = eV_D + (E_F - E_V) + (E_C - E_F) \quad (2.5)$$

The distance between Fermi level and band edges is small if the semiconductors are heavily doped, thus  $(E_F - E_V)$  and  $(E_C - E_F)$  are negligible in Eq. (2.5), and threshold voltage can be calculated by

$$V_{th} \approx V_D \approx E_g / e \quad (2.6)$$

A typical  $I$ - $V$  characteristic of a p-n junction is shown in Figure 2-11.

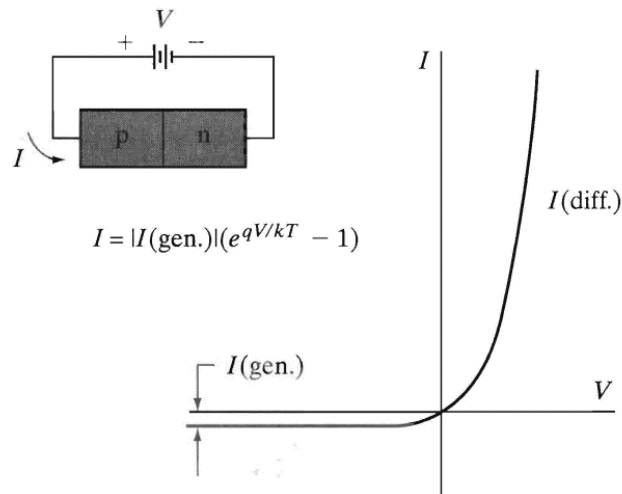


**Figure 2-11.  $I$ - $V$  characteristic of a p-n junction [78]. Note that  $I(\text{gen.})$  refers to the generation current whose magnitude depends on the generation rate of electron-hole pairs in the diode [78].**

The experimental diode  $I$ - $V$  characteristics of different semiconductors are shown in Figure 2-12. The threshold voltage of each semiconductor agrees well with its band gap.

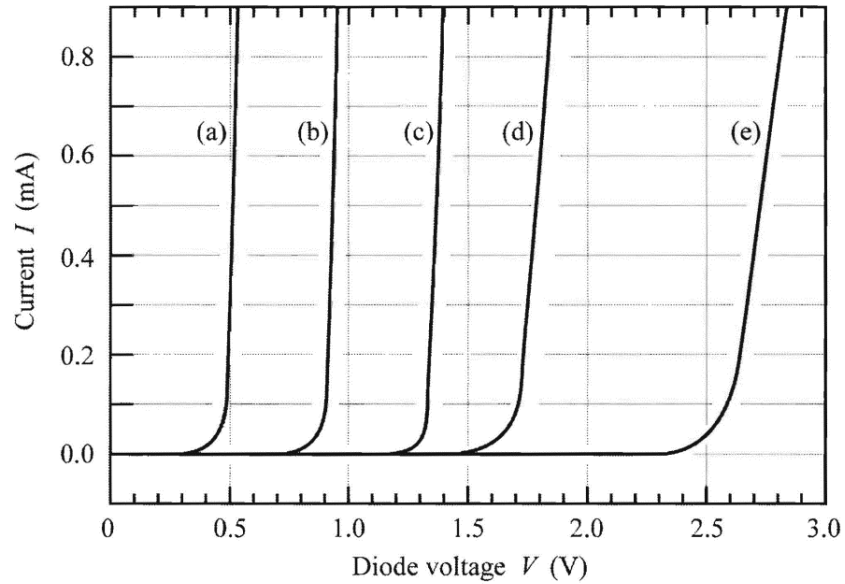


**Figure 2-12. Current-voltage characteristics of p-n junctions based on different semiconductors at 295 K [79]. (a) Ge,  $E_g \approx 0.7$  eV ; (b) Si,  $E_g \approx 1.1$  eV ; (c) GaAs,  $E_g \approx 1.4$  eV ; (d) GaAsP,  $E_g \approx 2.0$  eV ; (e) GaInN,  $E_g \approx 2.9$  eV .**

### 2.1.3.2 Emission Energy and Drive Voltage

A semiconductor with a band gap of  $E_g$  emits a photon possessing the following relationship:  $h\nu \approx E_g$ . The photon energy is approximately the same as the band gap of the semiconductor. Due to the requirement of energy conservation, in an ideal diode, the energy of an injected electron is equal to the energy of an emitted photon [80]

$$eV = h\nu \quad (2.7)$$

Thus, ideally, the photon energy from a diode equals to the drive voltage of an LED times the elementary charge. Combining Eq. (2.6) and (2.7), the diode voltage is given by

$$V = h\nu / e \approx E_g / e \quad (2.8)$$

The actual drive voltage of a real diode will deviate from the ideal value due to several mechanisms. Some diodes could have a series resistance which induces an additional voltage drop. Contact resistance, abrupt heterostructures induced resistances, and bulk resistance especially in semiconductors with low carrier mobilities and carrier concentrations can be responsible for the series resistance in the diode. On the other hand, carrier energy can be lost in the form of phonon emission as shown in Figure 2-13. In semiconductors with large band discontinuities (III-nitrides), the injected individual electron loses energy of magnitude  $\Delta E_c - E_0$ , where  $\Delta E_c$  is the conduction band discontinuity and  $E_0$  is the energy corresponding to the ground state (or lowest quantized state) in the quantum well of conduction band. Similarly,  $\Delta E_v - E_0$  is the energy lost from each injected hole, as  $\Delta E_v$  is the valence band discontinuity and  $E_0$  is the minimum quantized state in quantum well of valence band [81].

The total voltage drop in a forward-biased LED in practice is given by

$$V = \frac{E_g}{e} + IR_s + \frac{\Delta E_c - E_0}{e} + \frac{\Delta E_v - E_0}{e} \quad (2.9)$$

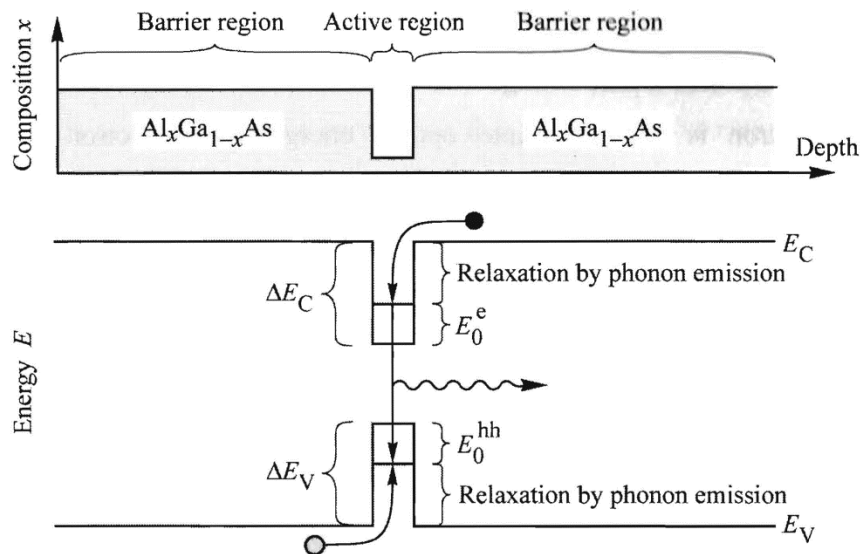


**Figure 2-13. Chemical composition and energy band diagram of an AlGaAs quantum well structure, note the energy loss of carriers by the phonon emission [82].**

### 2.1.4 LED Manufacturing Process

The value chain of LED manufacturing can be divided into three large segments: (a) substrate production; (b) LED die fabrication; and (c) packaged LED assembly. The details of each segment are shown in Figure 2-14.

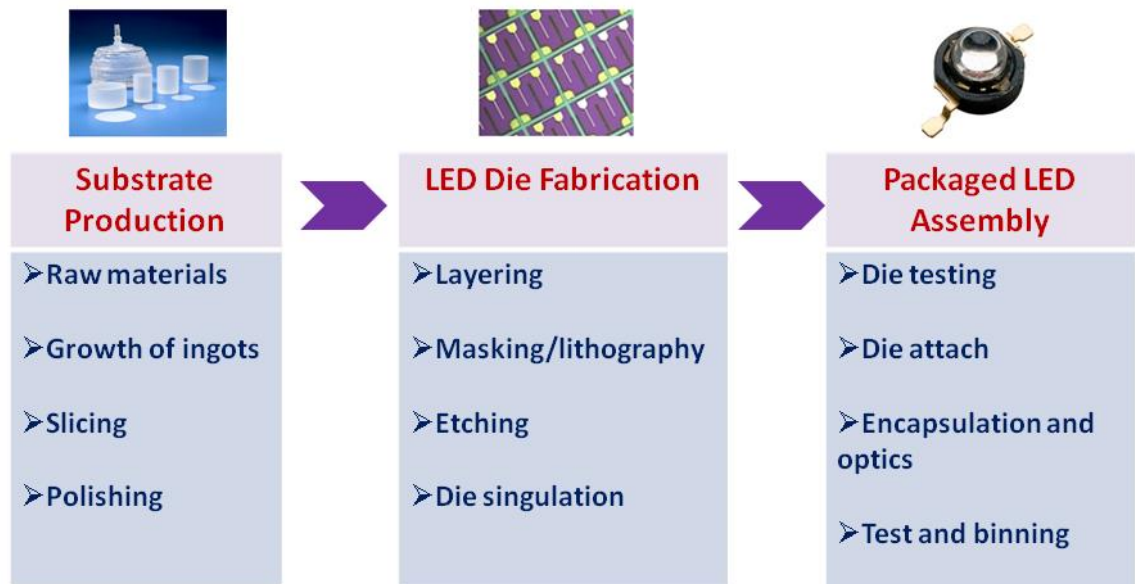


Figure 2-14. Three major steps of LED manufacturing (reproduced from [83]).

#### 2.1.4.1 Substrate Production

In this stage, highly polished and cleaned sapphire wafers are prepared for GaN epilayer growth in an MOCVD reactor. The processing steps in this stage are shown in Table 2-2.

Table 2-2. Manufacturing steps associated with sapphire wafer (reproduced from [83]).

Processing Step	Picture	Description

Boule growth in reactor		The Czochralski method is used to melt alumina and grow a large crystal boule of sapphire
Core fabrication		Sapphire cores with the appropriate diameters are created by drilling the sapphire boule with diamond tools
Wafer slicing		Slicing the cores into thin wafers using a diamond internal diameter saw with deionized cooling water
Lapping and beveling		Rough-cut wafers are treated to remove saw marks and other defects on both sides by using 6 $\mu$ m diamond slurry; reduce the thickness

		of wafers and release strain accumulated by slicing
Polishing and chemical-mechanical planarization		Polycrystalline diamond slurry (3 $\mu$ m-1 $\mu$ m) are used to polish wafers to remove irregularities
Geometry and optical inspection		Wafers are inspected to identify geometric or optical defects that may limit yield
Final cleaning		To remove trace metals, residues and particles. First cleaned by NH <sub>4</sub> OH, dilute HF, and deionized water. Then the wafers are cleaned by HCl and H <sub>2</sub> O <sub>2</sub> followed by deionized water rinse.

### 2.1.4.2 Fabrication of LED Die

The LED die fabrication process is divided into two steps: epitaxial growth and front-end processes. The details in each step are listed in Table 2-3 and Table 2-4.

**Table 2-3. GaN epitaxy growth details (reproduced from [83]).**

<b>Processing step</b>	<b>Description</b>
Bake out	Sapphire substrate is nitrided at high temperature in the atmosphere of ammonia and hydrogen
Nucleation layer growth	The substrate temperature is dropped down to 550°C to grow a thin Al <sub>2</sub> O <sub>3</sub> nucleation layer (3% or less of the wafer thickness)
Temperature ramp	To stabilize the nucleation layer, the substrate is heated up to 1200°C under reduced ammonia pressure.
Buffer layer and n-type GaN layer (3.84μm)	A 50-100 atomic thick amorphous gallium film is grown on the substrate at 550°C. After this, the substrate is heated up until the gallium layer forms a mirror-like layer of gallium nitride. Then a layer of n-type GaN is deposited.
MQW active layer (60nm)	InGaN quantum well is grown at 750°C-850°C. Approximately 20 angstroms thick of InGaN and 100 angstroms thick of GaN are included in this layer. The process is repeated for several times to grow a MQW structure.
p-type layer (170nm)	After the growth of MQW is done, the wafer

	is heated back up for the growth of p-type AlGaIn confinement layer.
--	--

**Table 2-4. LED die fabrication after epitaxy growth (reproduced from [83]).**

<b>Processing step</b>	<b>Sub-steps</b>
Wafer inspection	Carefully inspect the wafer to check if any cracks or defect which might make the wafer unsuitable can be found.
P contact	<ul style="list-style-type: none"> <li>➤ Cleaning</li> <li>➤ 0.097 <math>\mu\text{m}</math> thick Ag deposition by PVD</li> <li>➤ 0.103 <math>\mu\text{m}</math> thick Ti deposition by PVD</li> <li>➤ 0.681 <math>\mu\text{m}</math> thick W deposition by PVD</li> <li>➤ Measurement</li> <li>➤ Cleaning</li> </ul>
N contact opening	<ul style="list-style-type: none"> <li>➤ Lithography 1-coating</li> <li>➤ Lithography 1-baking</li> <li>➤ Lithography 1-stepper</li> <li>➤ Lithography 1-development</li> <li>➤ Measurement</li> <li>➤ Wet Etching Ti + W</li> <li>➤ Wet Etching Ag</li> <li>➤ Remove photoresist</li> <li>➤ Measurement</li> <li>➤ Cleaning</li> <li>➤ Lithography 2-coating</li> <li>➤ Lithography 2-baking</li> </ul>

	<ul style="list-style-type: none"><li>➤ Lithography 2-stepper</li><li>➤ Lithography 2-development</li><li>➤ Measurement</li><li>➤ GaN etching (1.5 <math>\mu\text{m}</math>)</li><li>➤ Remove photoresist</li><li>➤ Measurement</li><li>➤ Cleaning</li></ul>
GaN pattern	<ul style="list-style-type: none"><li>➤ 400 nm dielectric layer by CVD</li><li>➤ Measurement</li><li>➤ Cleaning</li><li>➤ Lithography 3-coating</li><li>➤ Lithography 3-baking</li><li>➤ Lithography 3-stepper</li><li>➤ Lithography 3-development</li><li>➤ Measurement</li><li>➤ Dielectric etching</li><li>➤ Remove photoresist</li><li>➤ Measurement</li><li>➤ Cleaning</li></ul>
N contact	<ul style="list-style-type: none"><li>➤ Lithography 4-coating</li><li>➤ Lithography 4-baking</li><li>➤ Lithography 4-stepper</li><li>➤ Lithography 4-development</li><li>➤ Measurement</li></ul>

	<ul style="list-style-type: none"> <li>➤ Cleaning</li> <li>➤ 0.284 <math>\mu\text{m}</math> Al deposition by PVD</li> <li>➤ 0.069 <math>\mu\text{m}</math> Ni deposition by PVD</li> <li>➤ 3.256 <math>\mu\text{m}</math> Au-Sn by ECD</li> <li>➤ Remove photoresist</li> <li>➤ Measurement</li> <li>➤ Cleaning</li> </ul>
Other	<ul style="list-style-type: none"> <li>➤ Back grinding sapphire</li> <li>➤ Fine grinding sapphire</li> <li>➤ Scribe laser</li> <li>➤ Break substrate</li> </ul>

### 2.1.4.3 Assembly of Packaged LED

In this step, LED die is mounted in the package. Electrical connections are made, phosphor, encapsulant and optics are applied. Testing and binning processes are involved in this step for quality control and product classification purposes.

**Table 2-5. LED packaging and assembly steps (reproduced from [83]).**

Processing step	Description
Package element building	Two layers of alumina are prepared for the LED chip mounting
Stud bumping	Process of wire bonding, where gold is bonded to the die pad

Reflow	The LED is heated to a temperature which is higher than the melting point of solder, but lower than the temperature which may damage other components of the LED package
LED and protective die attach	To protect LED from being destroyed by electrostatic discharge, it is attached to the package element
Reflow	The LED is heated to the melting point of solder again
Under filling	An organic polymer and inorganic filler is added to the package. This can provide support to the solder ball interconnect.
Phosphor	YAG: Ce <sup>3+</sup> phosphor coating is applied to convert the emission of the package from blue to longer wavelength
Lens	An optical lens which can gather and direct light in the appropriate beam angle for the specific application
Annealing	Upon heating, polymer, phosphor and lens are annealed together, then the three parts are in one cohesive unit
Substrate dicing	Individual packaged LED is formed by cutting the substrate

## 2.2 III-Nitride Compound Semiconductors

### 2.2.1 Crystal Structure of Nitrides

Wurtzite, zinc blende, and rock salt are three polytypes of III-nitrides materials [84]. The space group of rock salt GaN is  $Fm\bar{3}m$  in the Hermann-Mauguin notation. Rock salt form of III-nitride can only exist under high pressure, as the transition from covalent bonding to ionic bonding induced by reduced lattice dimensions can only occur under high pressure [84-87]. Since the rock salt phase of GaN only survives under high pressure, practical significance is quite limited for daily lighting.

The space group for zinc blende structure is  $F\bar{4}3m$  [84]. The unit cell of zinc blende is cubic. In each unit cell, two sets of face-centered cubic (fcc) sublattices are included. If one set of fcc sublattice slides along the body diagonal with the distance of one quarter, it will coincide with the other set. Under ambient conditions, zinc blende phase of III-nitrides is not a thermodynamically favorable structure. However, the GaN and InN thin films epitaxially grown on  $\{001\}$  planes of MgO [88], GaAs [89], SiC [90], and Si [91] substrates are zinc blende.

The thermodynamically stable structure of III-nitrides is wurtzite [84]. The space group for wurtzite is  $P6_3mc$ . Each hexagonal unit consists six atoms of each atomic type. Similar to zinc blende structure, the wurtzite structure also consists of two sets of sublattices. The two hexagonal close-packed sublattices penetrate

each other in the unit cell, with an offset along  $c$ -axis by  $5/8$ . The main difference between wurtzite and zinc blende structures arises from the stacking sequence of closest packed diatomic planes: it is AaBbCc along  $\langle 111 \rangle$  direction for zinc blende, while it is AaBbAa for wurtzite along  $\langle 0001 \rangle$  direction. Note that lower case and uppercase letters stand for the two different kinds of constituents. A stick-and-ball diagram of wurtzite GaN is shown in Figure 2-15. In nitrides, as shown in Figure 2-16, three planes and associated directions are technically important in terms of epitaxial growth:  $(0001)$   $c$ -plane,  $(11\bar{2}0)$   $a$ -plane, and  $(1\bar{1}00)$   $m$ -plane;  $\langle 0001 \rangle$ ,  $\langle 11\bar{2}0 \rangle$  and  $\langle 1\bar{1}00 \rangle$ . The lattice constants for III-nitrides are commonly measured by XRD according to Bragg's law. This method is considered as the most accurate one [84]. The measured and calculated lattice constants of wurtzite III-nitrides are shown in Table 2-6.

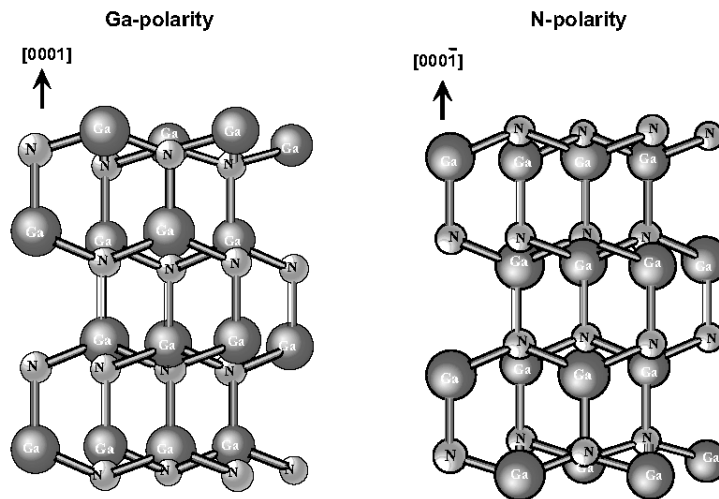


Figure 2-15. Stick-and-ball diagrams of wurtzite GaN[84].



	Pseudopotential LDA [95]	3.06	4.91
	FP-LMTO LDA [96]	3.084	4.948
GaN	Bulk crystal [97]	3.189	5.1864
	Relaxed layer on sapphire [98]	3.1892	5.1850
	Powder [99]	3.1893	5.1851
	Relaxed layer on sapphire [100]	3.1878	5.1854
	GaN substrate-LEO [101]	3.1896	5.1855
	Pseudopotential LDA [95]	3.162	5.142
	FP-LMTO LDA [96]	3.17	5.13
InN	Powder [99]	3.538	5.703
	Pseudopotential LDA [95]	3.501	5.669
	FP-LMTO LDA [96]	3.53	5.54

## 2.2.2 Physical Properties of III-Nitrides

### 2.2.2.1 Bandgaps and Bonding Characteristics

As mentioned in Section 2.1.2.4, one major advantage of III-nitride compound semiconductors is the wide coverage of the direct bandgap. The bandgaps of GaN and AlN are 3.42 eV and 6 eV. According to a recent study, the bandgap of InN is not the previously assumed value of 1.9 eV but rather 0.78 eV [102]. Thus, by alloying wurtzite polytypes of GaN, AlN, and InN to form a continuous alloy system, the bandgap can cover a range from 0.78 eV to 6 eV. The corresponding

emission wavelength of III-nitrides based LEDs and lasers covers from red light to ultraviolet. The bandgaps and lattice constants of III-nitrides, other semiconductors, and related substrates are shown in Figure 2-17.

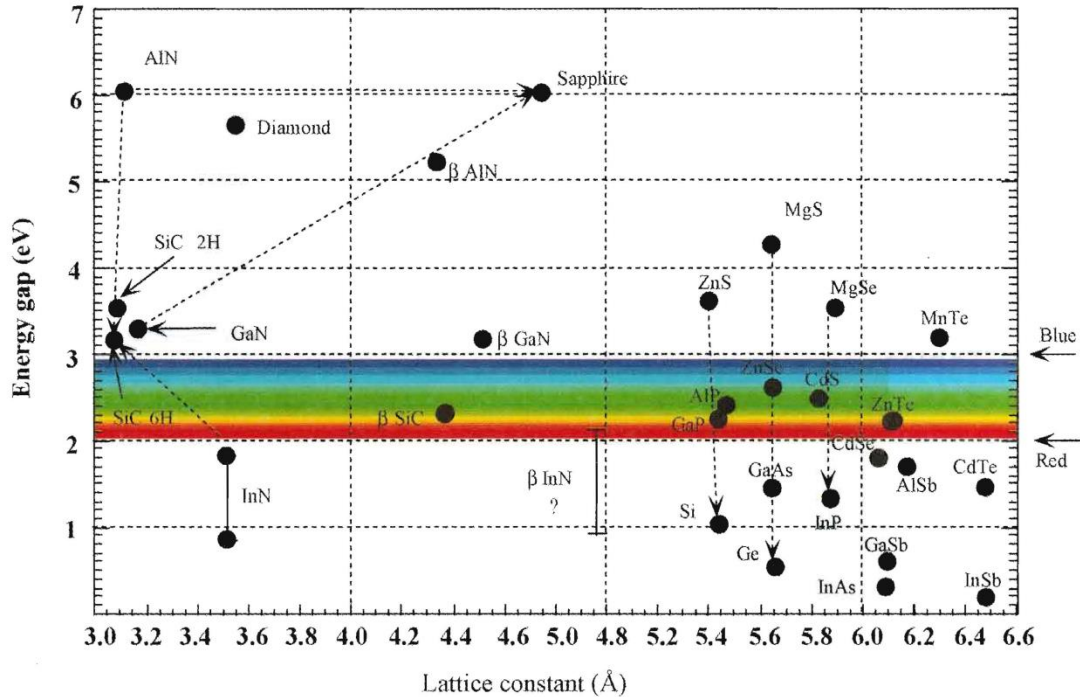


**Figure 2-17. The bandgap nitrides, substrates commonly used for nitrides, and other conventional semiconductors versus their lattice constants (after [84]).**

From Figure 2-17, we can find that the bandgaps of III-nitrides semiconductors, especially GaN and AlN, are wider than most of the conventional semiconductors. The reason is, the bonding type within III-nitrides, is not completely covalent, but partially covalent and partially ionic. A fractional ionic character (FIC) is defined for a binary compound AB as  $FIC = \frac{|Q_A^* - Q_B^*|}{|Q_A^* + Q_B^*|}$ , where  $Q_A^*$  and  $Q_B^*$  are effective charges for atoms A and B, respectively. In the case of pure covalent

bonding,  $Q_A^* = Q_B^*$ , so  $FIC=0$ . For pure ionic compound, all eight electrons belong to the anion,  $Q_A^* = 8$ ,  $Q_B^* = 0$ , then  $FIC=1$ . The calculated effective radii, the effective charges, and FIC for AlN, GaN, and InN are listed in Table 2-7.

**Table 2-7. Calculated values of ionic radii ( $\text{\AA}$ ), effective charges (electrons), and the FIC for III nitrides (after [103]).**

Compound	$r_{III}$ ( $\text{\AA}$ )	$r_N$ ( $\text{\AA}$ )	$Q_{III}^*$ (e)	$Q_N^*$ (e)	FIC
AlN	0.8505	1.0523	1.12	6.88	0.72
GaN	0.9340	1.0119	1.98	6.02	0.51
InN	1.0673	1.0673	1.83	6.17	0.54

The first Brillouin zones of the wurtzite and the zincblende structures, calculated by the full potential-linear muffin-tin orbital (FP-LMTO) method with the local density approximation (LDA) are shown in Figure 2-18. The band structures of (a) wurtzite GaN, (b) wurtzite AlN, and (c) wurtzite InN were also calculated in this way and are shown in Figure 2-19.

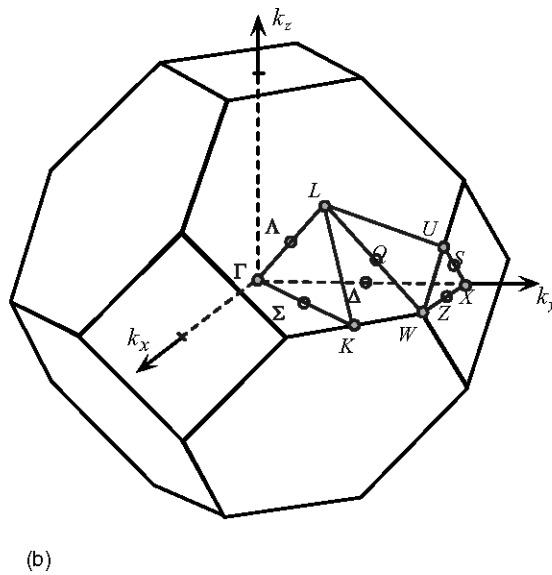
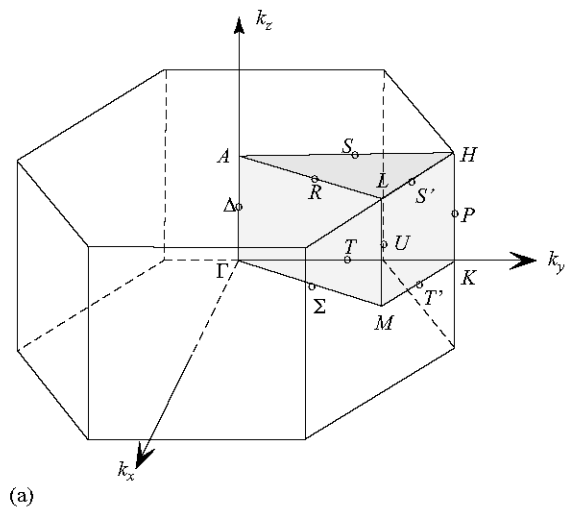


Figure 2-18. First Brillouin zones of (a) the wurtzite and (b) the zincblende structures (after [84]).

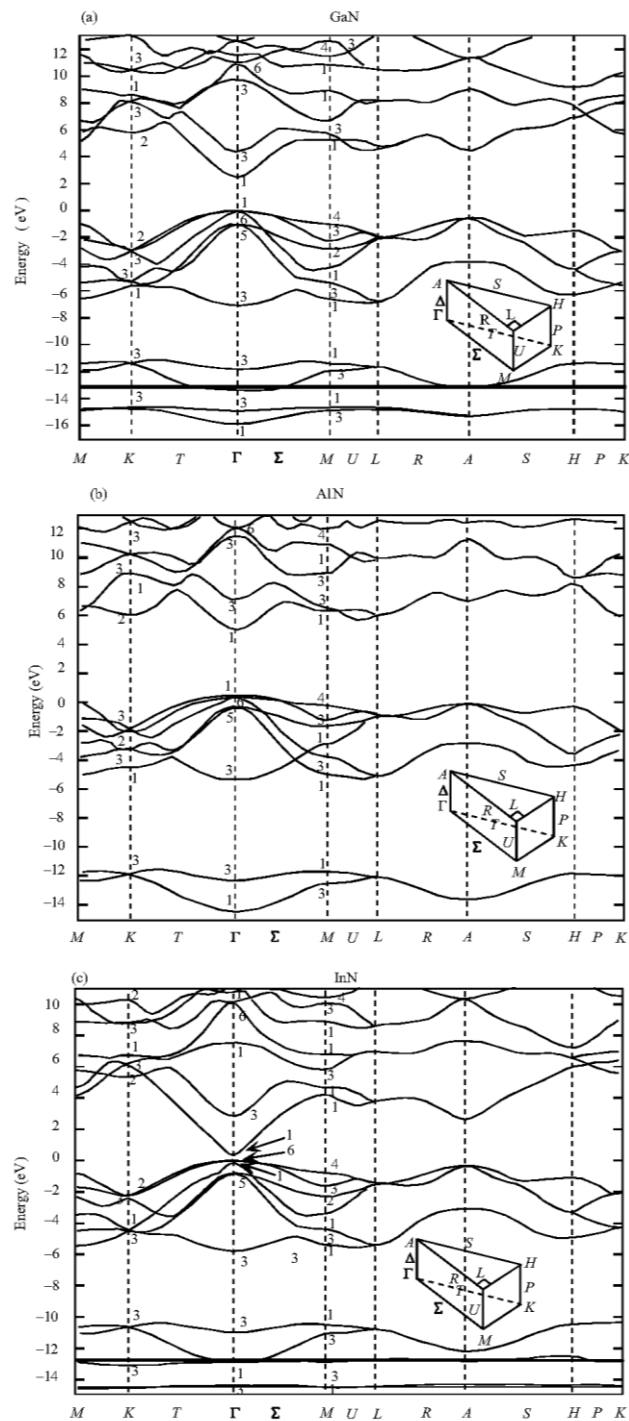


Figure 2-19. Calculated band structures of (a) wurtzite GaN, (b) AlN, and (c) InN in the LDA within the FP-LMTO method (after [104]).

### **2.2.2.2 Advantages of III-Nitrides and III-Nitride Based Devices**

The wide bandgap of III-nitrides has paved a way for the achievement of LED based white light source. Integrated with a high efficiency phosphor, InGaN based blue light LEDs can be a highly efficient white light source to serve as a replacement of the cold-cathode fluorescent lamp(CCFL) for back lighting of liquid crystal displays, and it is also commercialized as a highly efficient and long lifetime daily lighting source to replace compact fluorescent lamp and incandescent lamps [105]. Moreover, arising from large bonding energy and small atomic mass, the phonon energy of GaN is large, so the lattice scattering is hard to occur, which result in the high thermal conductivity and high saturation drift velocity of GaN. Owing to the large bandgap, breakdown voltage of GaN based devices is high. Large bandgap of GaN can keep both high temperature intrinsic carrier concentration and junction thermal current leakage at a low level. These advantages are quite attractive for the materials selection for high-frequency, high-power, high-voltage, high-temperature and low-loss semiconductor devices [106].

### **2.2.3 Epitaxial Growth Technique for III-Nitride Semiconductors**

### 2.2.3.1 MOCVD

MOCVD [also called metalorganic vapour phase epitaxy (MOVPE)] is the most widely used technology for the epitaxial growth of III-Nitride thin film. In a MOCVD system, trimethylgallium (TMGa) is the gallium source, trimethylaluminium (TMAI) is the aluminum source, trimethylindium (TMIn), triethylindium (TEIn), diisopropylmethylindium (DIPMeIn), or ethyldimethylindium (EDMIn) is the Indium source, and ammonia is the nitrogen sources. The composition and growth rate are precisely controlled by the adjustment of the mass flow rate and dilution of the various components of the gas stream. A block of graphite called a susceptor is used as the substrate holder, which can also be heated by a RF coil, a resistance heater, or a strip heater. The walls of the MOCVD system are kept substantially colder than the heated interior because we are not willing to deposit thin films on the hot wall. The underlying chemical reactions involve a set of complex gas phase and surface reactions[84]. Organometallic precursor gases and ammonia are transported into the deposition system and the reactions usually take place near or on the surface of a heated substrate. This involves the reactions between metal source (TMGa, TMAI, and TMIn) and ammonia. In detail, chemical steps can be divided into the following: 1. Ga and N precursor adsorption and decomposition; 2. Ga and N desorption from the surface; 3. Ga and N surface diffusion; 4. Thermal decomposition of GaN as it related to growth. Kinetically, the balance between adsorption and desorption needs to be

considered. Hadis Morkoç discussed the thermodynamic and kinetic aspects of MOCVD in detail [84].

As shown in Figure 2-20, Nakamura et al. used a modified MOCVD system, which employed a novel two-flow approach that yielded excellent film quality. The reactor sources are supplied from a horizontal inlet, and a vertical subflow composed of nitrogen and hydrogen drives the reactants down to the substrate surface [107, 108]. On the other hand, the vertical flow can also suppress thermal convection effects [84]. Typically very high temperature is required for the growth of GaN thin film for a sufficient decomposition, surface diffusion of incoming species and adatoms.

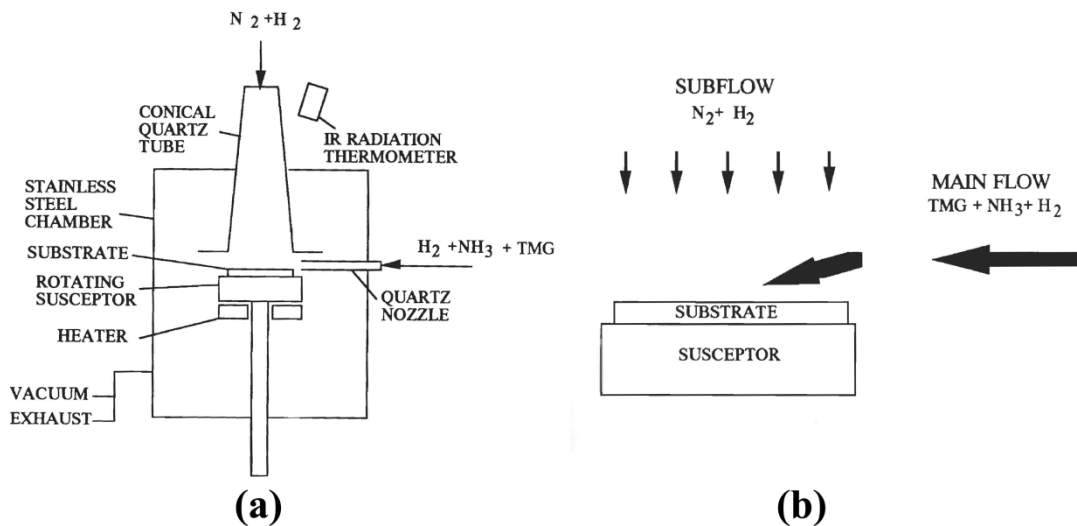


**Figure 2-20. Schematic of two-flow MOCVD system. a, set up of the MOCVD deposition system; b, principle of two flow reactor. (after [108])**

### 2.2.3.2 MBE

As mentioned previously, MOCVD is a mass transfer process with a thermodynamically equilibrium condition. On the contrary, in a MBE system, the composition of the thin film, together with its doping level, reply on the arrival rate of the constituent elements and dopants [109]. Thus, the growth condition of MBE is governed by kinetics. The thin film growth process in a MBE system can be summarized in sequence as: adsorption, desorption, surface diffusion, incorporation, and decomposition. These processes are shown schematically in Figure 2-21.

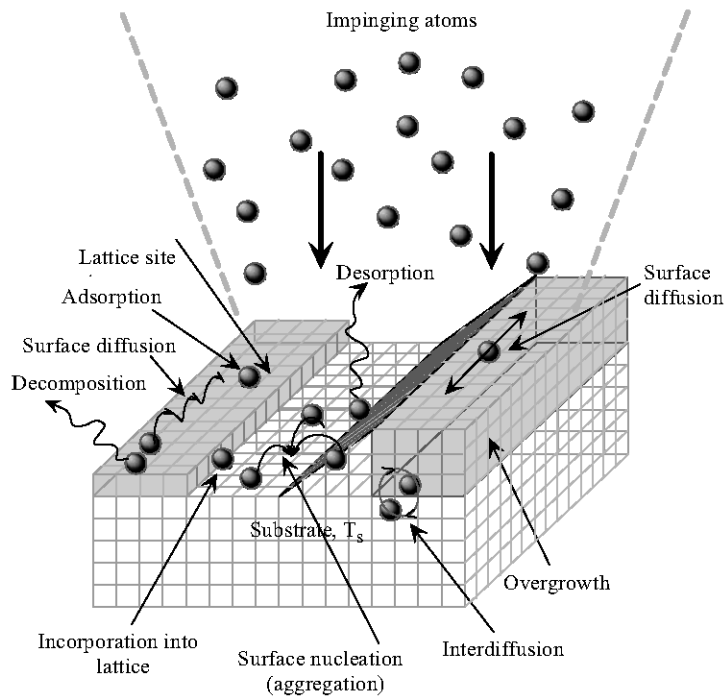


**Figure 2-21. Surface processes during MBE growth: adsorption, desorption, surface diffusion, lattice incorporation, and decomposition (after [84]).**

To maximum the surface diffusion of the adatoms, the growth rate of MBE is low (typical rate is  $1\mu\text{m/h}$ ). For the nitride growth in a MBE system, metal species of Ga, In, and Al are provided by its corresponding metal sources, respectively. On the other hand, nitrogen is provided by nitrogen gas. Due to its large molecular cohesive energy (9.8 eV per  $\text{N}_2$  molecular) between two nitrogen atoms, nitrogen gas, is considered as one of the least reactive gases. That is why the development of MBE as a growth technique for nitrides was slow at the beginning because of the low growth temperature compared with MOCVD system. Several approaches have been taken for the improvement of supplying an atomic source of nitrogen[84]. Radio frequency (RF) plasma and electron cyclotron resonance (ECR) microwave plasma sources are the two most successful techniques discovered [110]. The plasma source can crack molecular nitrogen to improve the activity of nitrogen. Finally the plasma stream is a complex mixture of atomic, molecular, and ionic N radicals. One type of MBE nitride system that incorporates a nitrogen plasma source to achieve GaN materials are shown in Figure 2-22. A major advantage for nitride growth is that a high growth temperature is unnecessary due to the atomic nitrogen source. The lower growth temperature will not result in high thermal stress upon cooling. Less diffusion and reduced alloy segregation can also be achieved by such a process. Compared with MOCVD systems, the p-GaN films grown by MBE are not passivated due to the absence of atomic hydrogen species during the growth [107].

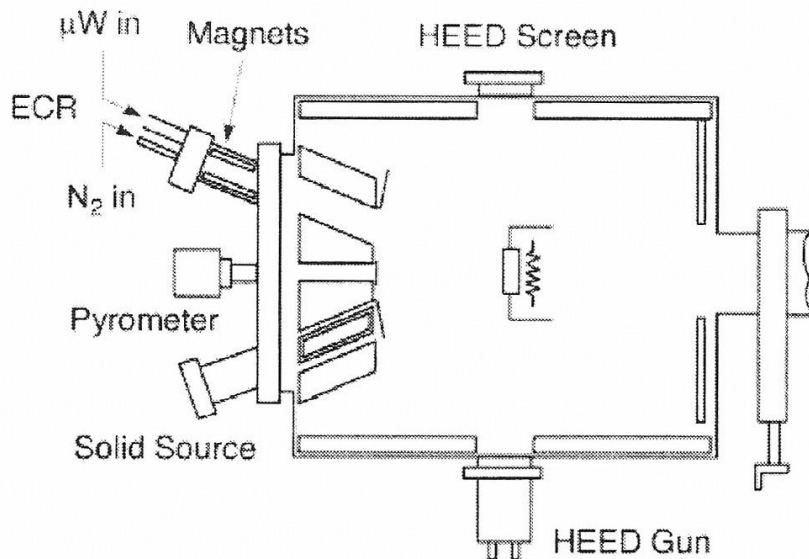


Figure 2-22. Nitride MBE growth system with a plasma nitrogen source (after [108]).

### 2.2.3.3 Sputtering

Sputtering is a physical vapour deposition process. Typically a target sits on the cathode of a magnetron, and argon ions, which are cracked from argon atoms by plasma (plasma is created between the anode and cathode of the magnetron), collide with the atoms in the target with a momentum transfer process. Compared with MOCVD and MBE system, sputtering is versatile and scalable [7]. From large scale production point of view, sputtering is an inexpensive way to grow III-nitride thin films. On the other hand, it is environmental friendly compared with MOCVD as no complex trialkyl compounds such as TMGa, TMIn, and TMAI are involved in the growth procedure.

The first reported plasma-assisted deposition of Group III-nitrides was by Fischer and Schroter in 1910, as they reacted indium metal with nitrogen in a cathodic discharge to produce InN powder[111]. Sputtering growth of GaN was initialized by Hovel and Cuomo in 1972[112], and followed up by a series of studies by tuning types of targets, atmosphere, and substrate temperature [113-133]. A typical reactive sputtering system for the growth of III-nitride thin films is shown in Figure 2-23. The vacuum of the chamber is controlled by the pumping system, and nitrogen and argon are introduced from the gas inlets on the left hand side of the chamber. The plasma is created by the magnetron with RF power. A gallium metal target sits on top of the magnetron (cathode). The substrate is mounted on the substrate holder. The substrate can be heated as the GaN growth needs an elevated temperature.

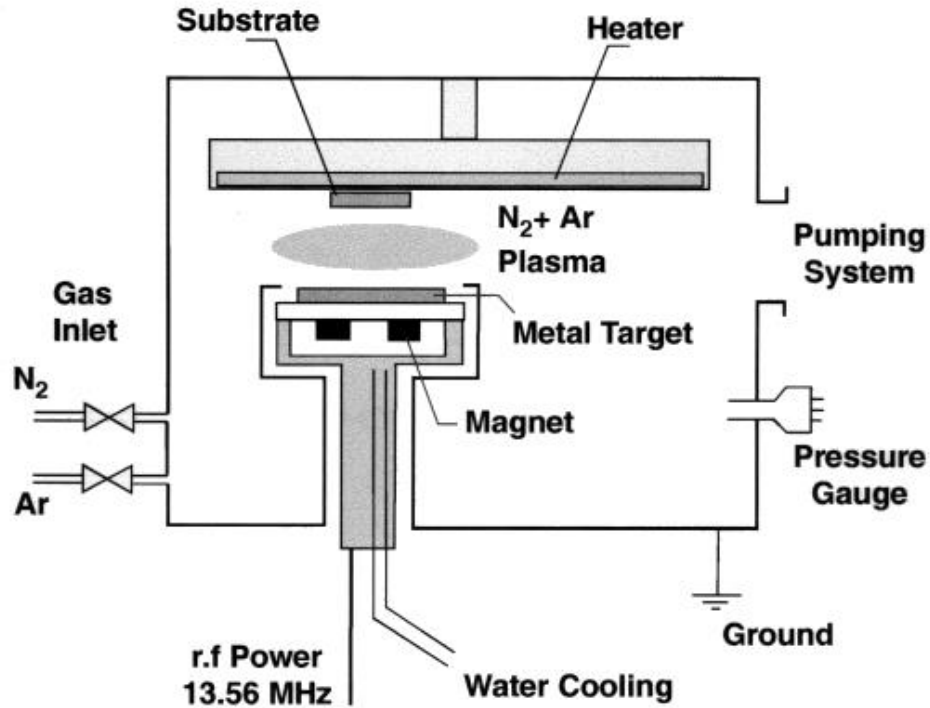
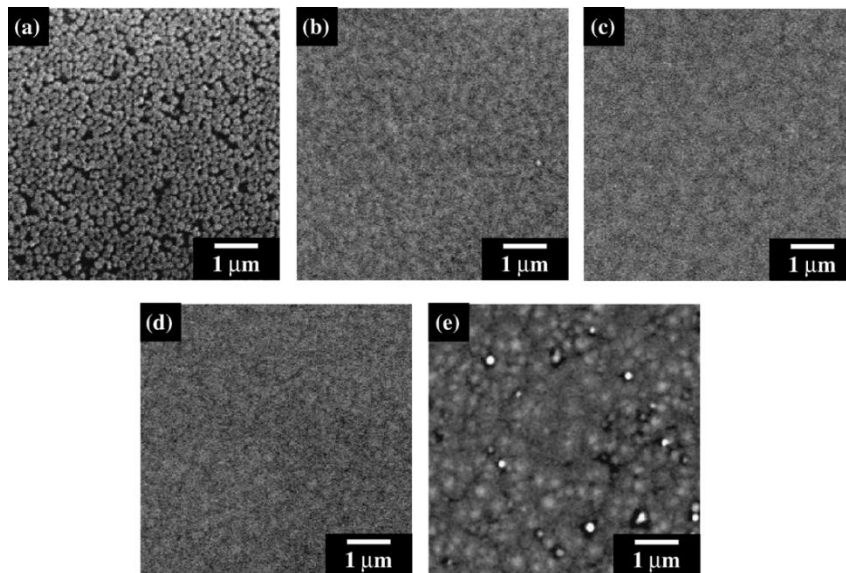


Figure 2-23. Schematic diagram of a planar diode rf reactive sputtering system for the deposition of GaN. The gallium source is a target consisting of a stainless steel cup filled with gallium. A mixture of molecular nitrogen and argon is used as nitrogen source and sputtering gas (rf plasma, 13.56 MHz) (after [134]).

Shinoda *et al.* studied growth of GaN and related alloys by sputtering epitaxy on (0001)-oriented sapphire substrate [135]. The surface morphology of the GaN thin film was affected by the gas pressure. When the nitrogen composition is 30% in the  $N_2/Ar$  mixture, GaN topography changed from nanosized columnar to flat surface, and finally became a pyramid facet structure with the increase of gas pressure as shown in Figure 2-24. A high-quality single crystalline epilayer with a flat surface can be obtained under 0.66Pa pressure and 40% $N_2$  in the  $N_2/Ar$

mixture as shown in Figure 2-25. When the gas pressure is low,  $N_2$  is insufficient and GaN thin film deposited on the substrate is nonstoichiometric. With the increase of gas pressure, more nitrogen can be involved in the sputtering process to form a stoichiometric GaN thin film. If the gas pressure continues to increase, the sputtered gallium atoms can be scattered by the  $N_2/Ar$  mixture, and as a result, the kinetic energy of the gallium atoms are reduced. Thus, the surface migration of the adatoms on the substrate becomes quite limited, and eventually, pyramid facet are formed on the substrate instead of a smooth layer.



**Figure 2-24.** The surface SEM images of GaN layers grown at gas pressures of (a) 0.66, (b) 0.93, (c) 1.33, (d) 1.99 and (e) 2.66 Pa and 30%  $N_2$  composition ratio in  $N_2/Ar$  mixture source gas (after [135]).

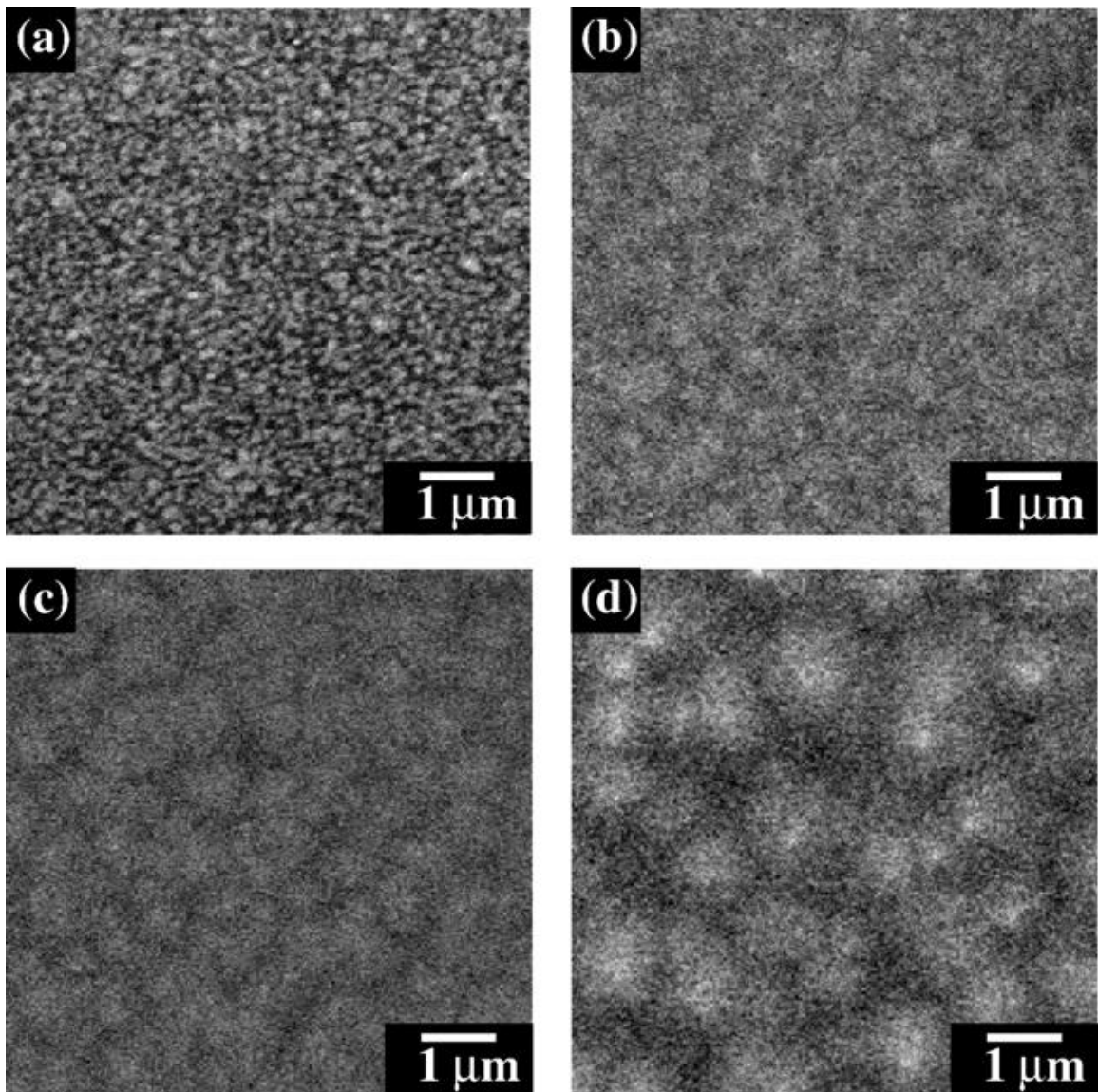


Figure 2-25. The SEM images of GaN layers grown at gas pressure of (a) 0.4, (b) 0.66, (c) 0.93 and (d) 1.33 Pa and 40%  $N_2$  composition ratio in  $N_2/Ar$  mixture source gas (after [135]).

High quality single crystal GaN was successfully grown on (0001) sapphire substrate by Park *et al.* using ultrahigh-rate magnetron sputtering epitaxy [131]. The background pressure of the deposition chamber was  $1 \times 10^{-6}$  Torr and a

$N_2/Ar$  gas mixture was used to react with gallium. The substrate was heated to  $1200^\circ C$  for deposition. The growth rate was  $10\text{-}60 \mu\text{m}/\text{min}$ . The full width at half maximum (FWHM) of the XRRC is  $300 \text{ arcsec}$  as shown in Figure 2-26. Pole figure and x-ray  $\phi$  scan results in Figure 2-26 also demonstrate the six fold symmetry of the hexagonal crystal.

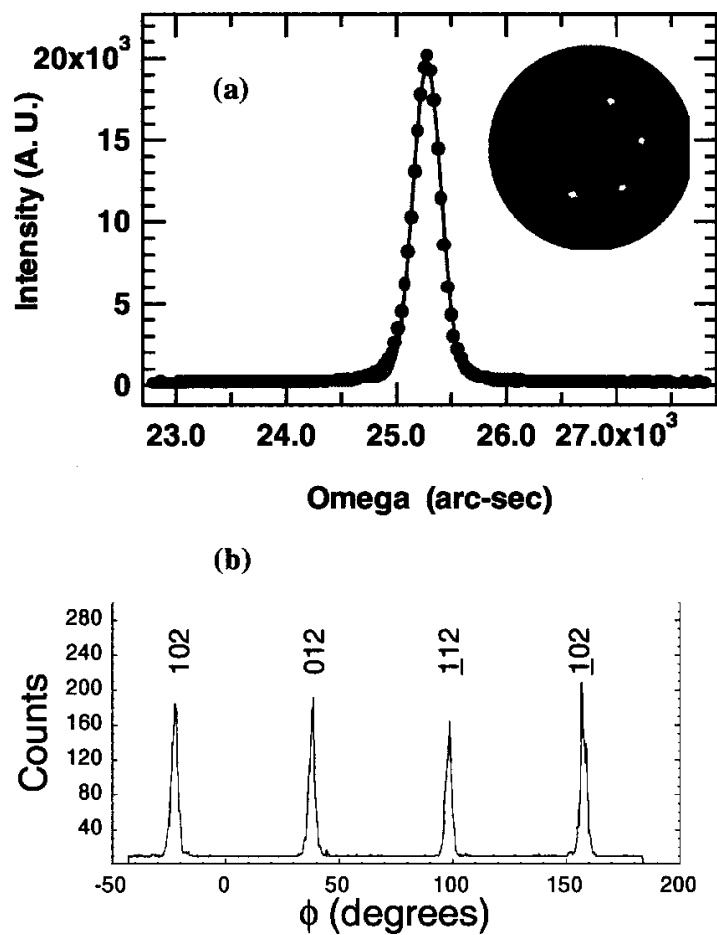


Figure 2-26. (a) XRRC from  $(0002)$  reflection. The inset shows the x-ray pole figure. (b) X-ray  $\phi$  scan of the sputtered GaN (after  $[131]$ ).

## 2.2.4 Substrates for the epitaxial growth of III-nitride thin film

### 2.2.4.1 Sapphire

Advantages of sapphire, such as low cost, high quality in bulk and surface properties, availability in large area, and lack of photon reabsorption have paved a way for it to become a dominant substrate material for III-nitride epitaxy. Two types of unit cells as shown in Figure 2-27 can represent the crystal structure of sapphire: rhombohedral and hexagonal. The rhombohedral unit cell has 4  $\text{Al}^{3+}$  ions and 6  $\text{O}^{2-}$  ions, and the hexagonal unit cell has 12  $\text{Al}^{3+}$  ions and 18  $\text{O}^{2-}$  ions. The hexagonal close packed lattice is formed by anions with  $a=0.476$  nm and  $c=1.299$  nm. Figure 2-28 shows the unreconstructed basal  $c$ -plane perspective views for both unit cells. Details of sapphire surface planes of rhombohedral structure is shown in Figure 2-29.

Several methods can be employed to produce single crystal sapphire substrates: edge-defined film fed growth (EFG), Czochralski crystal growth, heat exchanger method (HEM), and gradient solidification method (GSM) [136]. Czochralski technique uses a seed crystal to pull the crystal out from a molten charge of  $\text{Al}_2\text{O}_3$ . The crystallization will occur on the seed and follow the orientation of the seed[137]. In the case of HEM, the  $\text{Al}_2\text{O}_3$  is melted in the center of crucible. Helium is used to cool the center of the crucible from the bottom to the top of the crystal. Less thermal convection takes place as the temperature gradient is from the top to the bottom. GSM technique is a similar way to HEM. In EFG, the cross

section of the melt is controlled by a die, and the crystal is pulled out from the melt as a ribbon [138]. The most common dislocations that can be found in single crystal sapphire are edge or mixed dislocations with Burgers vectors in the  $\langle 11\bar{2}0 \rangle$  direction [139]. However, the crystal defects in the sapphire substrates are not likely to transfer into a GaN epilayer during growth[136].

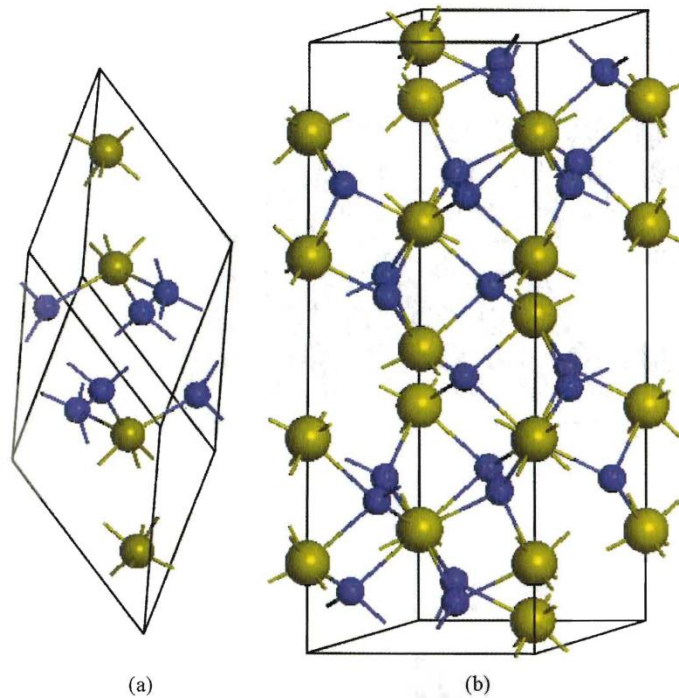


**Figure 2-27. The unit cell of sapphire: (a) rhombohedral unit cell; (b) hexagonal unit cell. Smaller spheres are for O and large ones are for Al (after [84, 136]).**

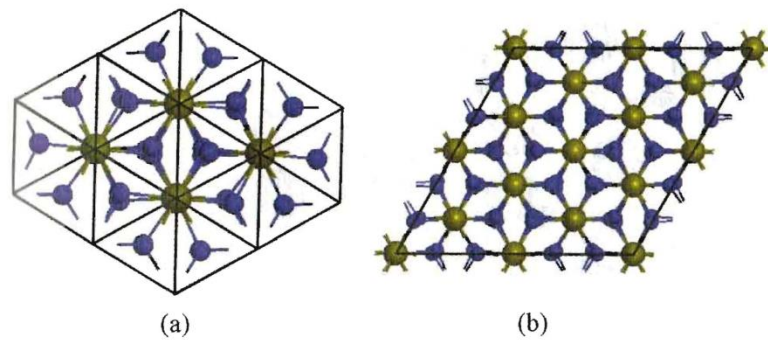


**Figure 2-28. perspective views in  $(2 \times 2 \times 1)$  unit cells: (a) along the  $[0001]$  direction in a rhombohedral unit cell; (b) along the  $[0001]$  direction in hexagonal unit cell. (After [84, 136])**

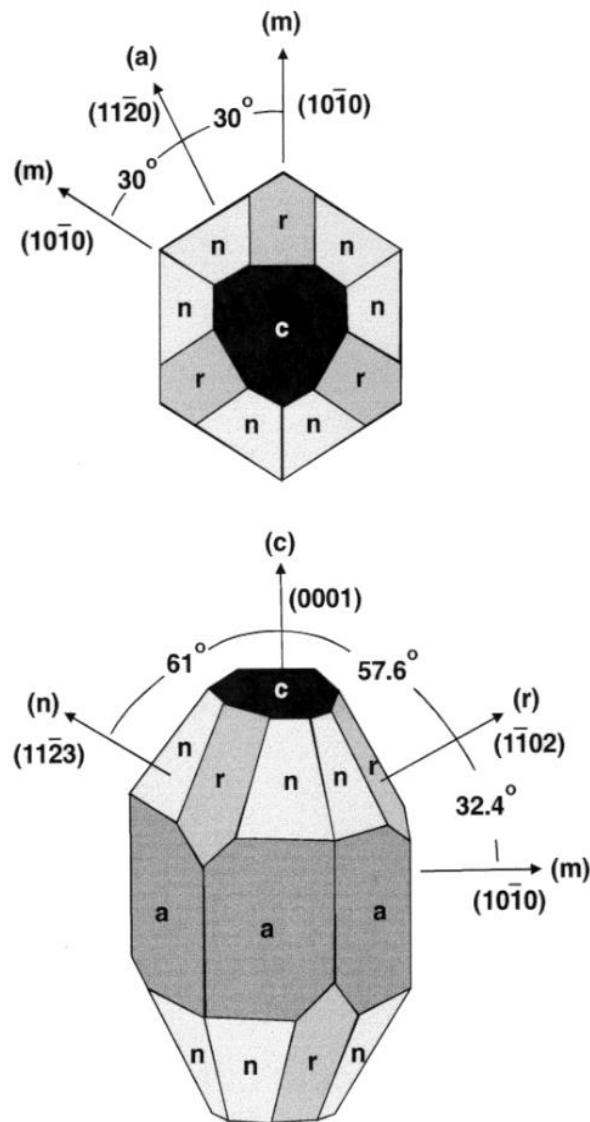


Figure 2-29. Rhombohedral structure and surface planes of sapphire[140].

The properties of sapphire related to GaN epitaxial growth are listed in Table 2-8. The crystallographic relationship between GaN films and sapphire substrates are listed in Table 2-9. Commercially available LEDs are based on the GaN growth on the basal plane of sapphire. The theoretical lattice constant mismatch between *c*-plane GaN and *c*-plane sapphire is 33%. In fact, the smaller cell of Al

atoms on the basal-plane rotates 30° away from the larger sapphire unit cell [84, 141] as shown in Figure 2-30. Then the actual lattice constant mismatch between GaN and sapphire can be calculated as:

$$\frac{\sqrt{3}a_{\text{wGaN}} - a_{\text{sapphire}}}{a_{\text{sapphire}}} \times 100\% = 15.9\% \quad (2.10)$$

**Table 2-8. Properties of sapphire [136].**

Property	Value	Range
Lattice constant (Å)	$a=4.765, c=12.982$	20 °C
Melting point (°C)	2030	
Density (g/cm <sup>3</sup> )	3.98	20 °C
Thermal expansion coefficient (K <sup>-1</sup> )	$6.66 \times 10^{-6}$    <i>c</i> -axis	20-50 °C
	$9.03 \times 10^{-6}$    <i>c</i> -axis	20-1000 °C
	$5.0 \times 10^{-6}$ ⊥ <i>c</i> -axis	20-1000 °C
Percentage change in lattice constants	$a/a_0=0.83, c/c_0=0.892$	Heating from 293 to 1300 K
Energy band gap (eV)	8.1-8.6	300 K, experimental value
Resistivity (Ω·cm)	$>10^{11}$	300 K

**Table 2-9. Crystallographic relationship between GaN film and sapphire substrates (reproduced from [136, 142]).**

Crystal plane	Miller indices $(h j k l)$ or $(h k l)$	GaN plane // sapphire plane	GaN direction // sapphire direction	References
<i>c</i>	(0001) <b>or</b> (001)	(0001)	$[\bar{1}2\bar{1}0] \parallel [\bar{1}100]$	<b>[141, 143]</b>
<i>a</i>	$(11\bar{2}0)$ <b>or</b> (110)	(0001); <b>or</b> $(10\bar{1}0)$	$[11\bar{2}0] \parallel [1\bar{1}00]$  $[11\bar{2}0] \parallel [0003]$	<b>[141, 144-146]</b>
<i>r</i>	$(10\bar{1}2)$ <b>or</b> (102)	$(11\bar{2}0)$	$[0001] \parallel [1\bar{1}01]$  $[0001] \parallel [\bar{1}011]$  $[1\bar{1}00] \parallel [11\bar{2}0]$	<b>[141, 147]</b>
<i>m</i>	$(10\bar{1}0)$ <b>or</b> (100)	$(10\bar{1}3)$ <b>or</b> $(1\bar{2}12)$	$[1\bar{2}10] \parallel [0001]$  $[10\bar{1}0] \parallel [1\bar{2}10]$	<b>[148]</b>

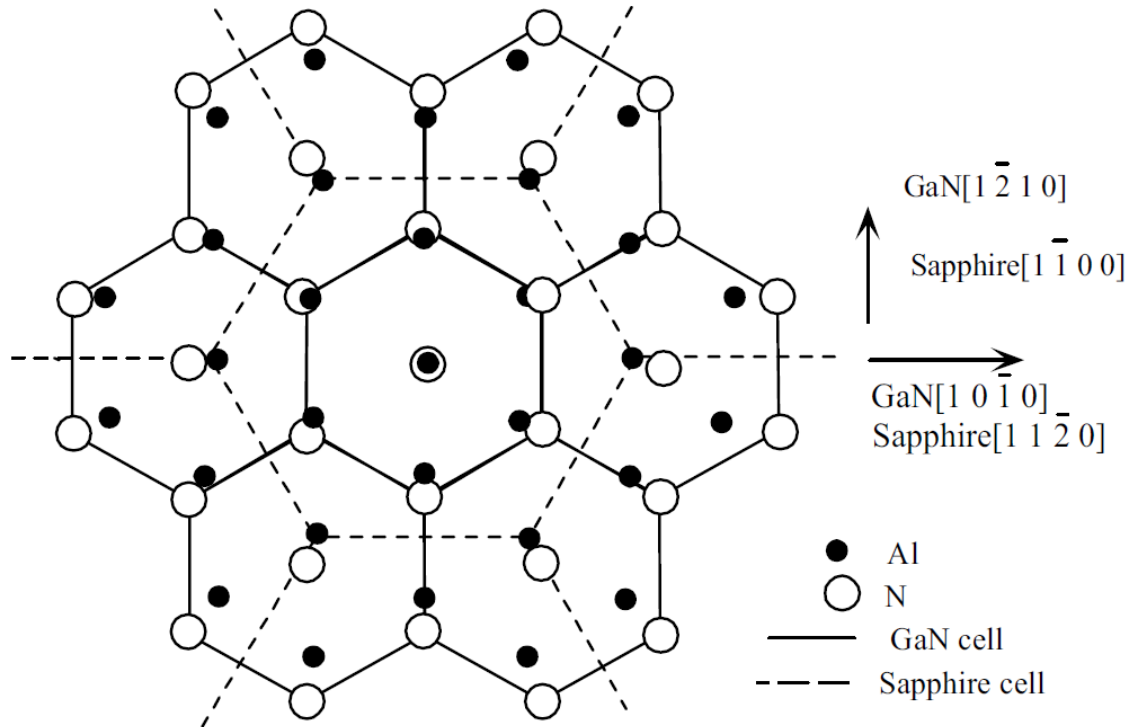


**Figure 2-30. Projection of bulk basal plane sapphire and GaN cation positions for the observed epitaxial growth orientation. The circles mark Al-atom positions and the dashed lines show the sapphire basal plane unit cells. The open circles mark the N-atom positions and solid lines show the GaN basal plane unit cell. The Al atoms on the sapphire plane sit at positions approximately 0.5 Å above and below the plane position [141].**

#### 2.2.4.2 Silicon Carbide

Compared with sapphire, silicon carbide has several advantages. The lattice constant mismatch between GaN and SiC is 3% for (0002) oriented GaN films, which is much smaller than the lattice constant mismatch between GaN and sapphire (16% after 30 degree rotation respect to *c*-axis). Thermal conductivity of silicon carbide (3.8 W/cm·K) is much higher than that of sapphire (0.23 W/cm·K)

for  $c$ -axis, 0.25 W/cm·K for  $a$ -axis), thus the thermal dissipation of devices based on SiC can be much faster than the devices based on sapphire. Device structure can be simplified because the electrically conductive nature of SiC has paved a way to make electrical contacts to the backside of the substrate, which can reduce the size of a chip in LEDs and avoid current crowding effects [149]. Unlike for sapphire substrates [150], GaN thin film on SiC does not rotate around the  $c$ -axis. In-plane and out-of-plane crystalline alignment of GaN are identical with the SiC substrate, so thin film planes can be well-registered and a cleaved facet can be easily formed in laser for light resonance [151].

SiC has more than 250 polytypes, however the basic structural unit for all polytypes is a tetrahedron of Si atoms with a C atom at its center as shown in Figure 2-31. The bonding between Si and C atoms is covalent. The distance between neighboring silicon or carbon atoms is approximately 3.08 Å (designated as  $a$ ) for all polytypes. Different stacking sequences of Si-C double layers lead to different SiC polytypes, which also result in different  $c$  values of each corresponding unit cell. In terms of 2H-, 4H-, and 6H-SiC polytypes, the corresponding  $c/a$  ratios are 1.641, 3.271, and 4.908 respectively. Properties of 3C, 2H, 4H and 6H SiC related to GaN thin film growth are listed in Table 2-10. The stacking sequences of Si-C double layers of the four most common SiC polytypes (3C-, 2H-, 4H-, and 6H-) are shown in Figure 2-32. The  $(11\bar{2}0)$  plane view of these polytypes are shown in Figure 2-33.

**Table 2-10. Properties of SiC at room temperature (reproduced from [136, 152]).**

Properties		Polytype	Value	Reference
Lattice constant (nm)		3C	$a=0.43596$	[153]
		2H	$a=0.30753, c=0.50480$	
		4H	$a=0.30730, c=1.0053$	
		6H	$a=0.30806, c=1.51173$	
Density (g/cm <sup>3</sup> )		3C	3.166	[154]
		2H	3.214	
		6H	3.211	
Thermal conductivity (W/cm·K)		4H	3.7	[155]
		6H	3.8	
Linear thermal expansion coefficient (X10 <sup>-6</sup> K <sup>-1</sup> )		3C	3.9	[156]
		6H	4.46 <i>a</i> -axis	
			4.16 <i>c</i> -axis	
Percentage change in lattice constants (300-1400 K)		6H	$\Delta a/a_0: 0.4781, \Delta c/c_0: 0.4976$	[157]
		3C	$\Delta a/a_0: 0.5140$	
Bandgap (eV)		3C	2.4	[158]
		6H	3.02	
		4H	3.26	

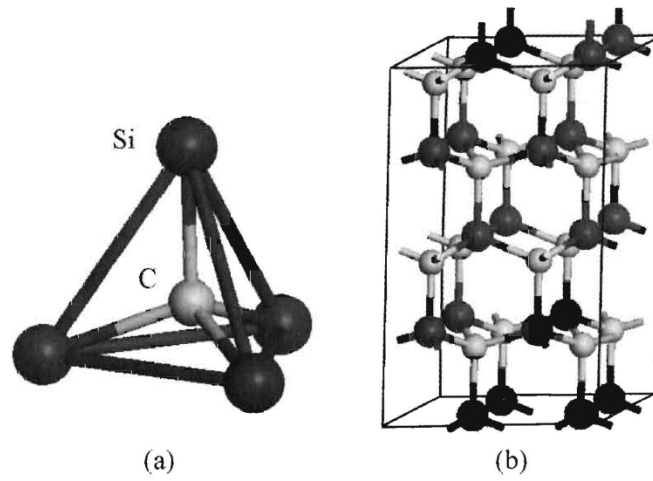


Figure 2-31. a, tetragonal bonding of a carbon atom with its four nearest silicon neighbors. The bond lengths depicted with  $a$  and C-Si (the nearest neighbor distance) are approximately 3.08 and 1.89 Å, respectively. b, three-dimensional structure of 2H-SiC structure[84].

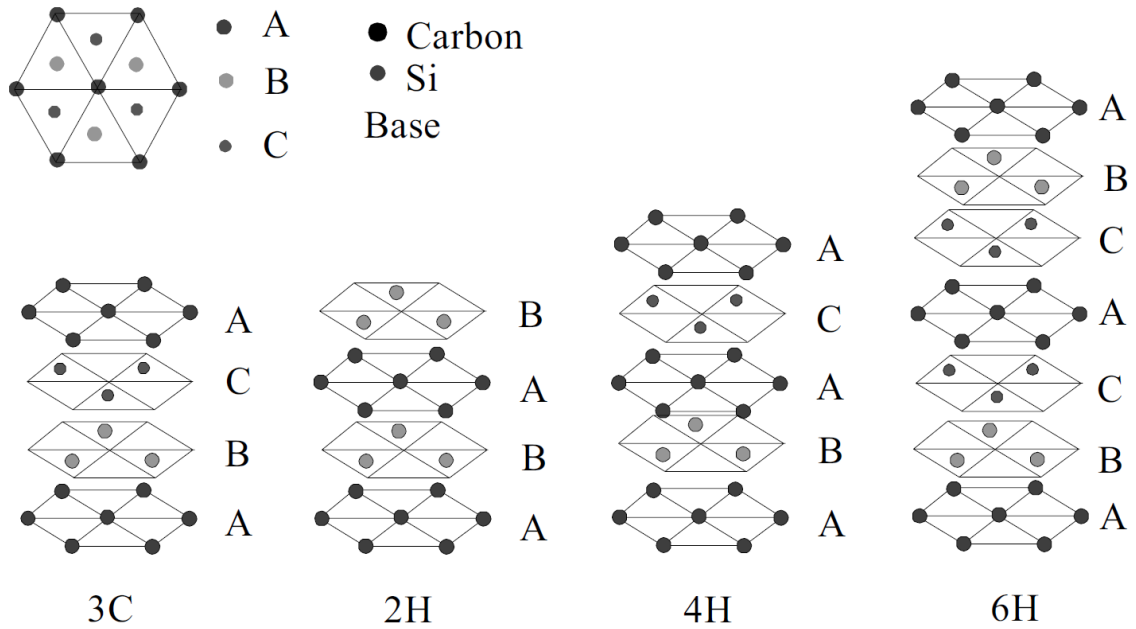


Figure 2-32. Stacking sequence of 3C-, 2H-, 4H-, and 6H-SiC [159].

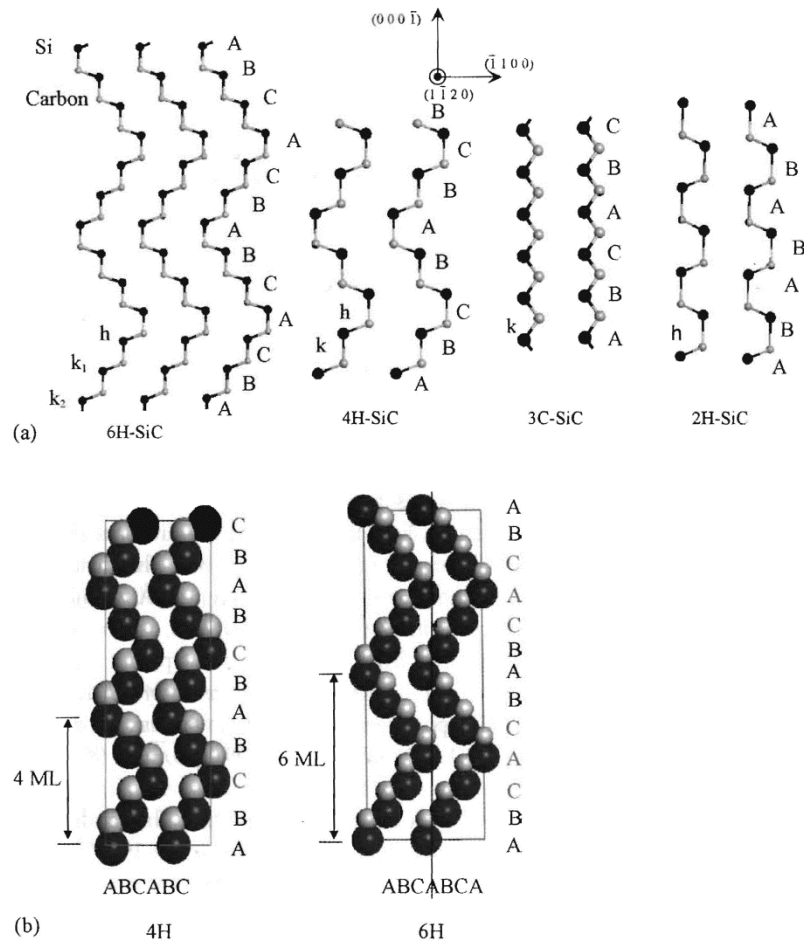


Figure 2-33.  $(11\bar{2}0)$  plane view of 3C-, 2H-, 4H-, and 6H-SiC polytypes [160].

Bulk SiC single crystal growth is achieved by a modified Lely process [136, 161]. Si, Si<sub>2</sub>C, and SiC<sub>2</sub> were used as the source of SiC. A SiC seed crystal is used to determine the orientation and polytype of the as-grown SiC. Mass transport is achieved via vapor transport from the SiC source zone to the growth zone. The growth temperature is 2200°C. Argon gas is used to protect the growth. Commercially available 4H- and 6H-SiC substrates are made by this technique [136].

Epitaxial relationship of GaN with 4H- or 6H-SiC is simple since the lattice mismatch between GaN and SiC is only 3%. In principle,

$$(0002)_{\text{GaN}} \parallel (0006)_{6\text{H-SiC}} \text{ or } (0004)_{4\text{H-SiC}}, \quad [11\bar{2}0]_{\text{GaN}} \parallel [11\bar{2}0]_{\text{SiC}}.$$

### 2.2.4.3 Silicon

Silicon is an attractive substrate for GaN thin film growth [136], as silicon wafers are low in cost, high in quality, and mature in manufacturing know-how. It is very easy to integrate GaN-based devices with other silicon electronics if silicon is used as the substrate [162]. However, GaN growth on Si is still a challenge as the lattice constant and thermal expansion coefficient mismatch between GaN and silicon is large (16.9% for lattice constant mismatch). As a result, the quality of GaN grown on (111) oriented Si is low, and the radiative carrier recombination efficiency is reduced by the existence of defects. Although GaN growth on Si has met many obstacles, many devices based on GaN are grown on Si substrates [136].

Silicon belongs to the cubic-crystal family. It has a similar lattice structure with diamond. Two sets of fcc sublattices are interpenetrated with a displacement of a quarter of body diagonal length of the cube ( $\sqrt{3}a/4$ , where  $a=0.543$  nm). The perspective views of silicon along [001], [011], and [111] directions are shown in Figure 2-34. The properties of silicon at room temperature are listed in Table 2-11.

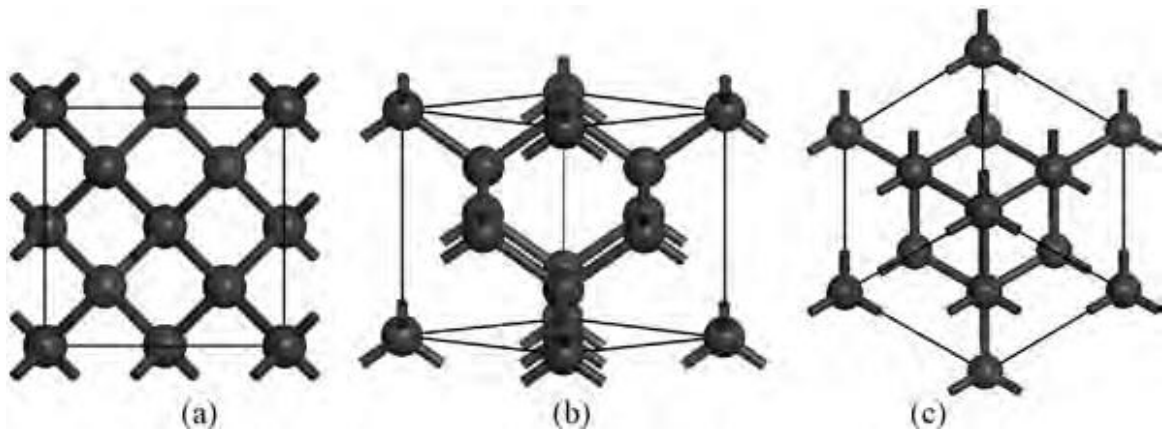


Figure 2-34. The perspective view along (a) the [001], (b) [011], and (c) [111] directions of a silicon cell [84].

Table 2-11. Properties of Si at room temperature [136].

Properties	Value	Reference
Lattice constant (nm)	0.543102	[163]
Density (g/cm <sup>3</sup> )	2.3290	[163]
Thermal conductivity (W/cm-K)	1.56	[164]
Thermal expansion coefficient (linear, X10 <sup>-6</sup> K)	2.616	[165]
Percentage change in lattice constant ( $\Delta a/a_0$ ):	0.3995	[166]
Energy bandgap (eV)	1.124	[167]

As mentioned above, the manufacturing technique of silicon wafers is quite mature. Bulk single crystal silicon is grown by either the Czochralski method or

the float zone method. To make commercial silicon wafers a series process of shaping, slicing, lapping, etching, polish, cleaning and inspection is employed after a single crystal silicon ingot is produced.

GaN epitaxial growth usually takes place on (111) oriented Si, and the epitaxial relationship of GaN on Si is  $\text{GaN } (0001) \parallel \text{Si } (111)$ , and  $\text{GaN } \langle 2\bar{1}\bar{1}0 \rangle \parallel \text{Si } \langle 011 \rangle$ .

## 2.3 Silicon Carbide Whiskers and Their Alignment

### 2.3.1 Materials Properties

Silicon carbide whiskers ( $\text{SiC}_w$ ) are beta phase silicon carbide (cubic) in the form of (111) oriented whiskers. The cross section of each whisker is a (111) plane of beta phase SiC. The stacking sequence of a Si-C double layer in beta-SiC is ABCABC along the body diagonal of a cube as shown in Figure 2-33.  $\text{SiC}_w$  has excellent mechanical properties. The tensile strength of whiskers (4 to 6  $\mu\text{m}$  diameter, 10 mm long, grown by vapor-liquid-solid process in Los Alamos National Laboratory) can be as high as 8.40 GPa (1, 220, 000 psi), and the elastic modulus is 581 GPa (84, 300, 0000 psi) on average [168]. Such a high performance of mechanical properties indicates that SiC whiskers can be excellent candidates as short-fiber reinforcement elements for a ceramic matrix [168].

### 2.3.2 Synthesis of SiC Whiskers

Silicon carbide whiskers can be synthesized by pyrolysis of rice hulls demonstrated by Lee and Cutler [169]. Sharma and Williams characterized the location of silica in rice hulls and realized that silica is primarily located within the outer epidermis toward the middle of the hull structure [5]. They also synthesized SiC whiskers from rice hulls. At the beginning the volatile constituents of rice hulls were driven out by coking without air contact at 900°C for 2h, then the specimens were reacted in argon between 1100°C and 1400°C. Excess carbon was burned off at 700°C for 2hr in air. Scanning electron micrographs as shown in Figure 2-35 demonstrated the formation of SiC whiskers. The whiskers were 0.2-0.5  $\mu\text{m}$  in diameter and up to 100  $\mu\text{m}$  in length.

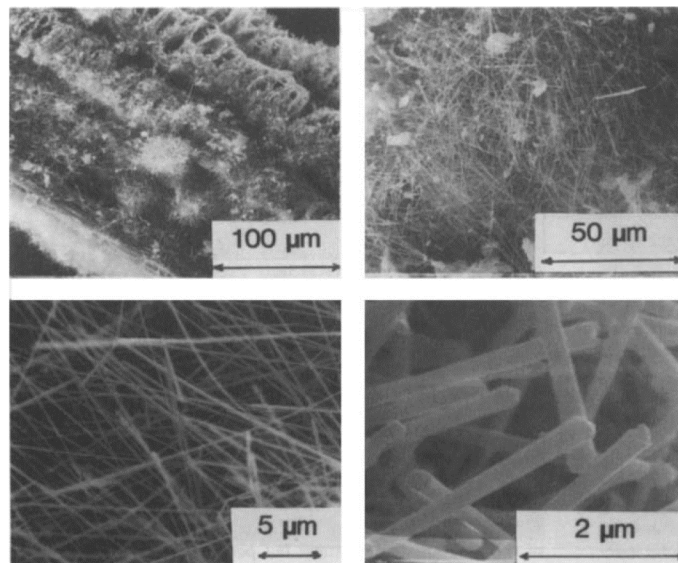


Figure 2-35. Scanning electron micrographs of SiC whiskers produced by pyrolysis of rice hulls[5].

On the other hand, Milewski *et.al* have grown beta-silicon carbide whiskers by vapor-liquid-solid (VLS) process [170]. A special reactor for VLS growth of SiC whiskers is shown in Figure 2-36. 30  $\mu\text{m}$  304 stainless steel was used as the catalyst which can also control the diameter of SiC whiskers. Carbon and silica were placed in an impregnated porous brick as raw materials. The reaction was in the atmosphere of methane, which is diluted by  $\text{H}_2$ ,  $\text{CO}$ , and  $\text{N}_2$ . SiO gas was formed by the reaction between C and  $\text{SiO}_2$ . When the reactor was heated in a large quartz tube furnace at  $1400^\circ\text{C}$ , SiO and  $\text{CH}_4$  reacted with the catalyst. Si and C dissolved in the solution of catalyst and precipitated in the form of SiC whiskers when supersaturated. The process is shown in Figure 2-37. The scanning electron micrograph of the product is shown in Figure 2-38.

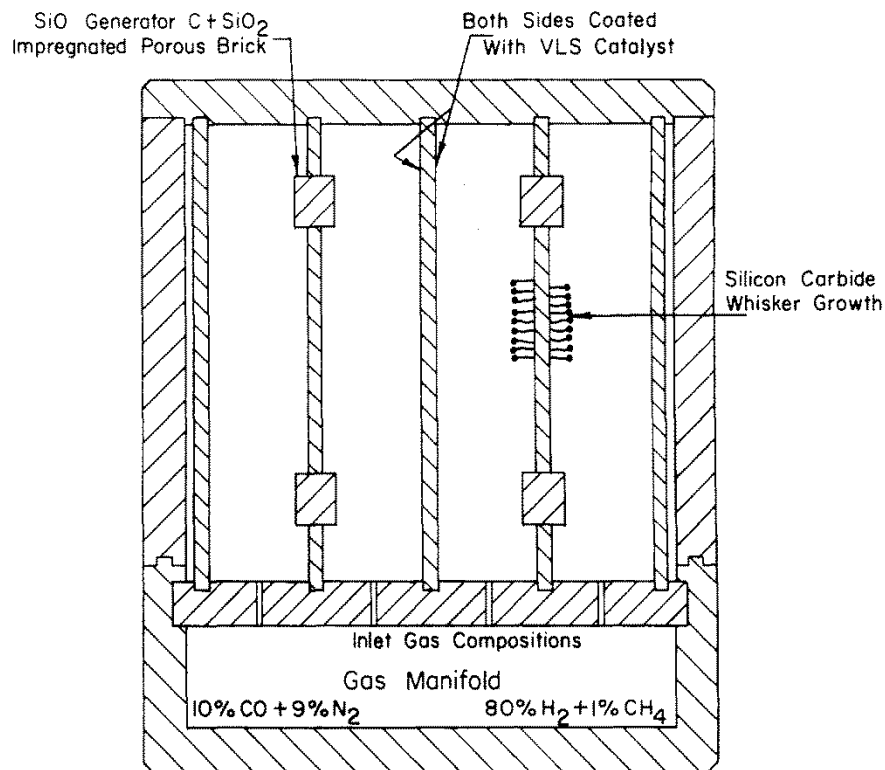


Figure 2-36. Cross-sectional view of whisker growth reactor[170].

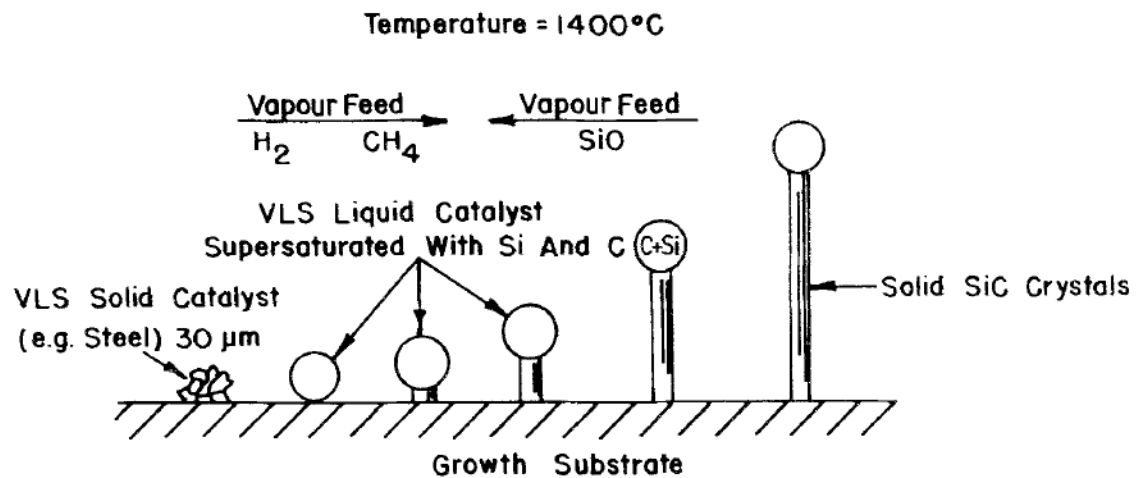


Figure 2-37. Illustration of the VLS process for SiC whisker growth [170].

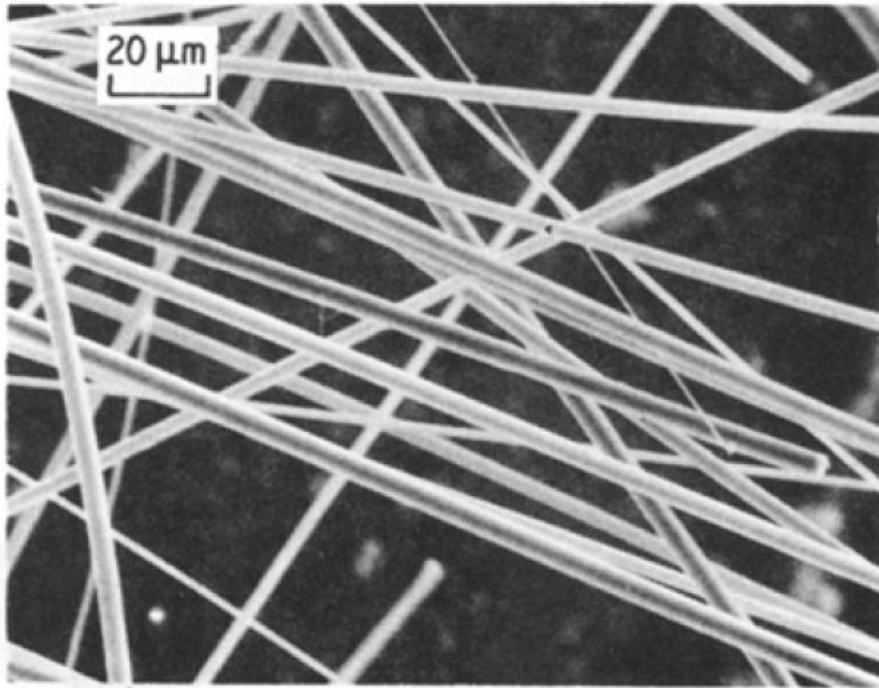


Figure 2-38. Scanning Electron Micrograph of SiC whisker grown by VLS process [170].

### 2.3.3 Alignment of SiC Whiskers in Ceramic Matrix by Extrusion for Toughening Effect

SiC whiskers-reinforced alumina matrix composites demonstrated that whisker reinforcement can toughen a brittle matrix [171-173]. Toughening behavior of silicon carbide whiskers embedded ceramic matrix depends on the crack deflection and bridging effect of whiskers. The fracture strength and toughness of unidirectionally oriented whiskers embedded ceramic matrix are higher than randomly oriented whiskers embedded ceramic matrix [8]. Faber and Evans

pointed out that the effect of crack deflection can be optimized when the whiskers are perpendicular to the crack plane [174]. The bridging effect of whiskers also requires the perpendicular relationship between whisker orientation and the crack plane [173].

Hasson et.al achieved the alignment of silicon carbide whiskers in an aluminum matrix by extrusion [175] in 1985. 20vol% SiC whiskers were blended with commercially available Al 6061 powders by cold compaction. As-pressed billets of the composite were formed by hot pressing. The billet was then transformed into a tube by extrusion.

After the previous work in metal matrices, Goto and Tsuge fabricated SiC-whisker-reinforced  $\text{Si}_3\text{N}_4$  by extrusion and hot-pressing in 1993 [8]. 20wt% of SiC whiskers were added into commercial-grade  $\text{Si}_3\text{N}_4$  powder together with sintering additives. The composition was mixed homogeneously by ball milling for 12hr. The green sheet was formed by extrusion in a vacuum pugmill. Sintering of the green sheet was accomplished by hot-pressing in a carbon die between 1600-1750°C at 40 MPa for 60 min in nitrogen. They concluded that the degree of alignment was controlled by varying the thickness of the green sheet.

## 3 Research Methodology

### 3.1 Manipulation and Alignment of SiC whiskers

#### 3.1.1 Morphology of As-received SiC whiskers

The appearance of as-received SiC whiskers from Alfa Aesar is shown in Figure 3-1. The average dimension of the as-received whiskers is 1.5  $\mu\text{m}$  in diameter, 18  $\mu\text{m}$  in length. The whiskers are (111) plane oriented. In Figure 3-1(a), we can clearly find the (111) planes of the whiskers. For the employment of SiC whiskers as the GaN epitaxial growth templates, the whiskers need to be aligned and embedded into a rigid ceramic matrix for polishing. The final concept product is illustrated in Figure 3-2.

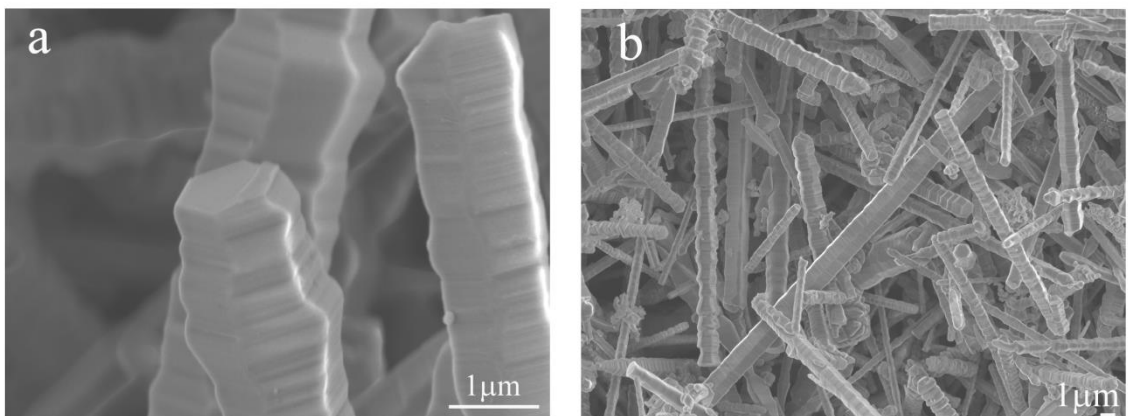


Figure 3-1. SEM images of as received SiC whiskers.

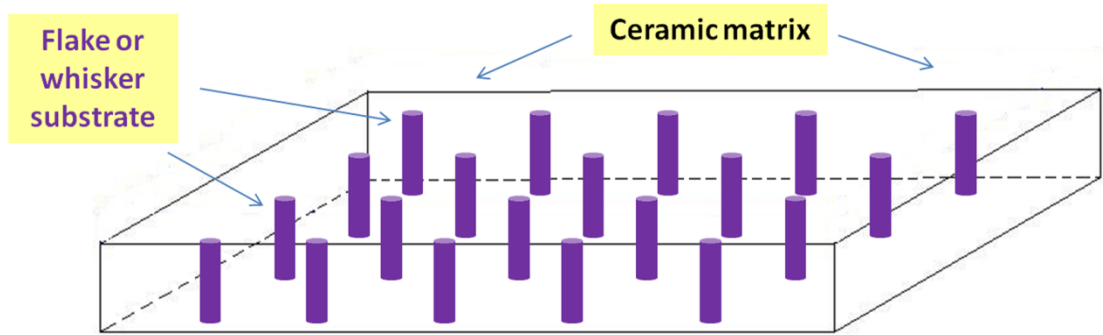


Figure 3-2. The concept of ceramic matrix embedded with aligned SiC whiskers.

### 3.1.2 Alignment Template

A 3M Vikuiti™ Brightness Enhancement Film (BEF) is used as the alignment template for SiC whiskers. This film is originally designed to be used together with liquid crystal display panels it serves as a brightness enhancement film in LCD displays. It utilizes a prismatic structure to provide up to a 60% brightness gain and saves power. In principle, it refracts light within the viewing cone (up to 35° off the normal line of BEF) toward the viewer, and it also can reflect the light outside this angle back into the film and recycle it until it exists at the proper angle (within the viewing cone) [176]. The operation principle is shown in Figure 3-3.

The detailed structure of microreplicated prism of as-received 3M Vikuiti™ BEF is characterized by optical microscopy (Nikon Eclipse LV100) as shown in Figure 3-4. As shown in the microscope images, the surface of 3M BEF is patterned with

periodical parallel grooves. From the cross section point of view, the prism angle is  $90^\circ$ . The distance between two adjacent prisms is  $24\ \mu\text{m}$ . With the small distance between two adjacent prisms and sharp angle at the bottom of each groove, a narrow space is ready at the bottom of each groove for the placement of single whiskers. The results of aligned SiC whiskers are shown in Chapter 5.

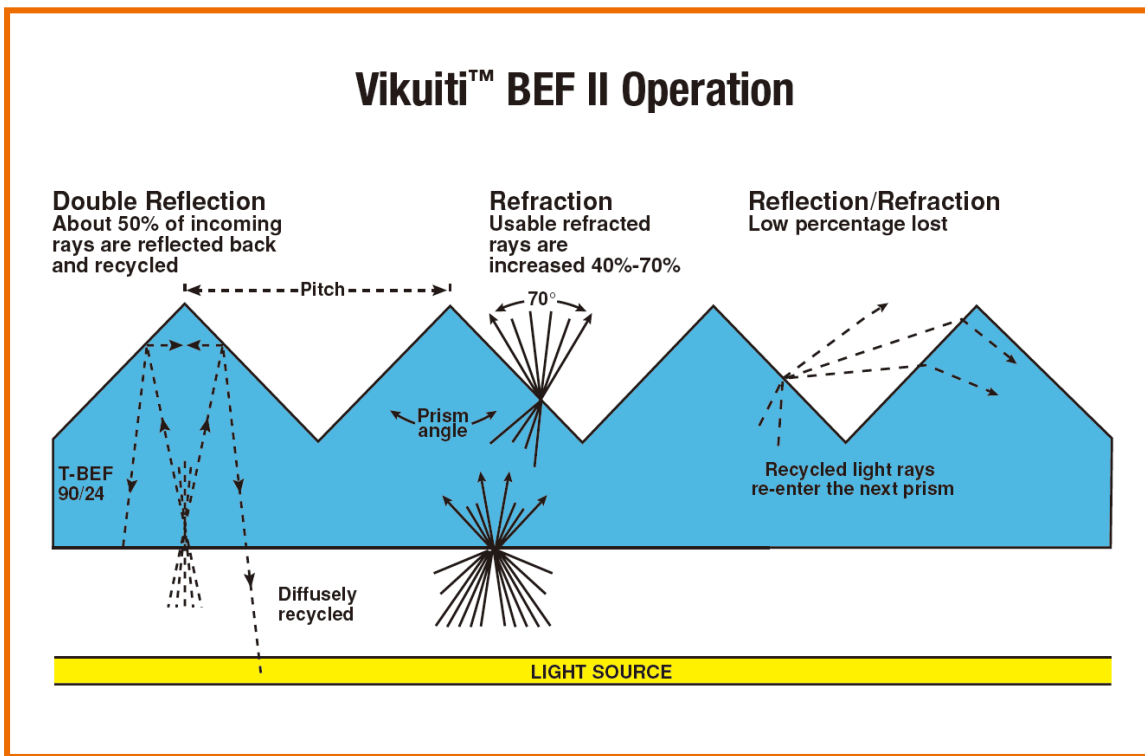
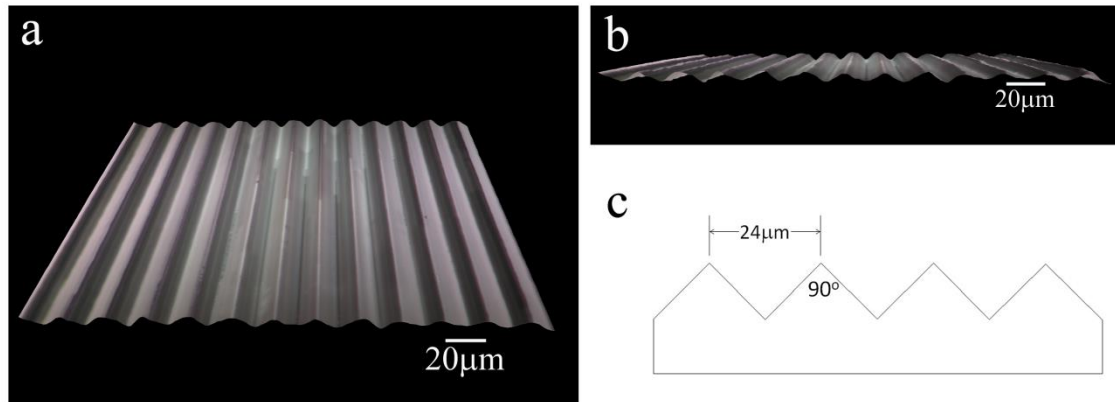


Figure 3-3. Operation Principle of 3M Vikuiti™ BEF 90/24 [176].



**Figure 3-4. a) Top view of 3M Vikuiti™ BEF; (b) Cross section view of 3M Vikuiti™ BEF; (c) Sketch of 3M BEF cross section.**

### 3.1.3 Tape Casting

The aligned SiC whiskers on 3M brightness enhancement film are transferred into an alumina matrix by using the tape casting technique. Aluminum oxide slip is tape casted directly on the surface of 3M brightness enhancement film. The aligned silicon carbide whiskers are surrounded by the aluminum oxide slip after tape casting. Once the slip is dry, the whiskers can stay in the alumina tape and eventually can be peeled off from the 3M BEF together with the alumina tape.

#### 3.1.3.1 Preparation of Aluminum Oxide Slip

A poly vinyl butyral binder system is used in the preparation of aluminum oxide slip. The batch formulation used in this work is shown in Table 3-1.

**Table 3-1. Tape casting batch formulation and corresponding function of each component**

Component	Weight Percentage (%)	Weight (g)	Function
Part 1:			
Aluminum oxide	57.35	28.675	
Menhaden fish oil, blown Z-3	1.15	0.575	Dispersant
Xylene	17.88	8.94	Solvent
Ethyl alcohol, anhydrous denatured	17.88	8.94	Solvent
Part 2:			
Poly (vinyl butyral), grade B-98	2.86	1.43	Binder
Butylbenzyl phthalate, S-160	1.44	0.72	Plasticizer
Poly (alkylene glycol)	1.44	0.72	Plasticizer
Total	100	50	

The batching procedure is listed as following:

1. Dry the aluminum oxide powder at 90 to 100°C for 24 hours;

2. Weigh and dissolve the fish oil in the xylene and add to a mill jar;
3. Weigh and add the ethyl alcohol to the mill jar;
4. Weigh and add the hot aluminum oxide powder;
5. Disperse mill by rolling at 60 rpm for 24 hours;
6. Weigh and add the plasticizers;
7. Weigh and add the binder;
8. Mix and homogenize by rolling for another 24 hours at 60 rpm, then the slip is ready for tape casting.

### **3.1.3.2 Direct Tape Casting on 3M BEF**

The tape casting was carried out on an 8" laboratory caster (manufactured by Cladan Technology Inc., Model 133A). 3M BEF was placed on top of silicone-coated Mylar film as the carrier of the tape casting machine. A doctor blade with adjustable gap as shown in Figure 3-5 was used in this work. The gap between the doctor blade and the carrier is adjusted by a micrometer. The thickness of the alumina green sheet was controlled at approximately 300  $\mu\text{m}$ . The tape casting speed was 3 cm/s. After tape casting, it took approximately 2 hours for the organic solvent to evaporate. When the green sheet became dry, it was ready for sintering.

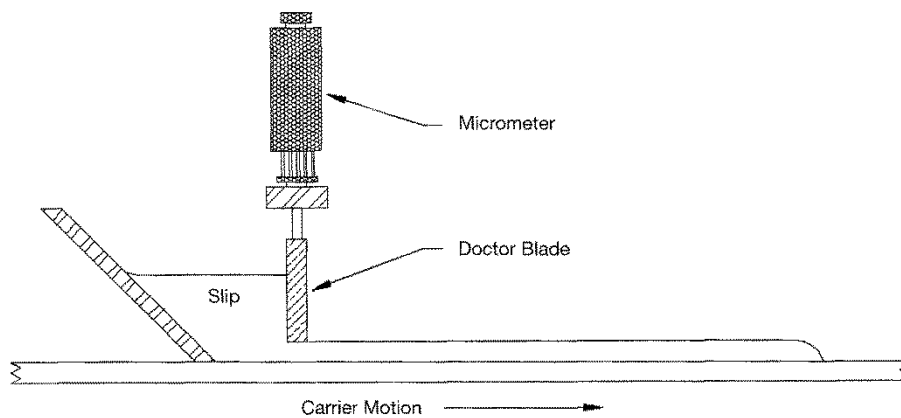


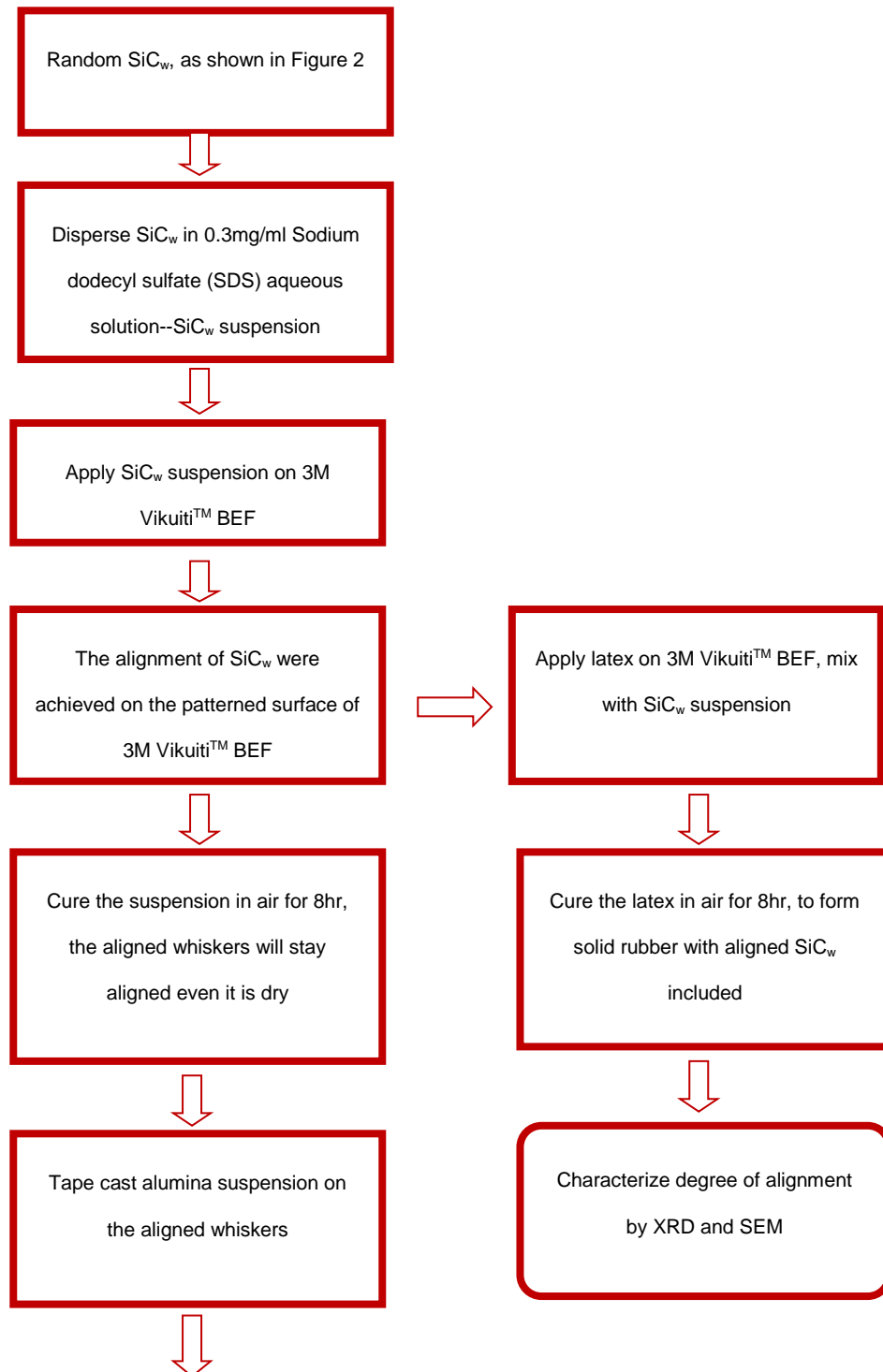
Figure 3-5. Standard doctor blade assembly with adjustable blade [177].

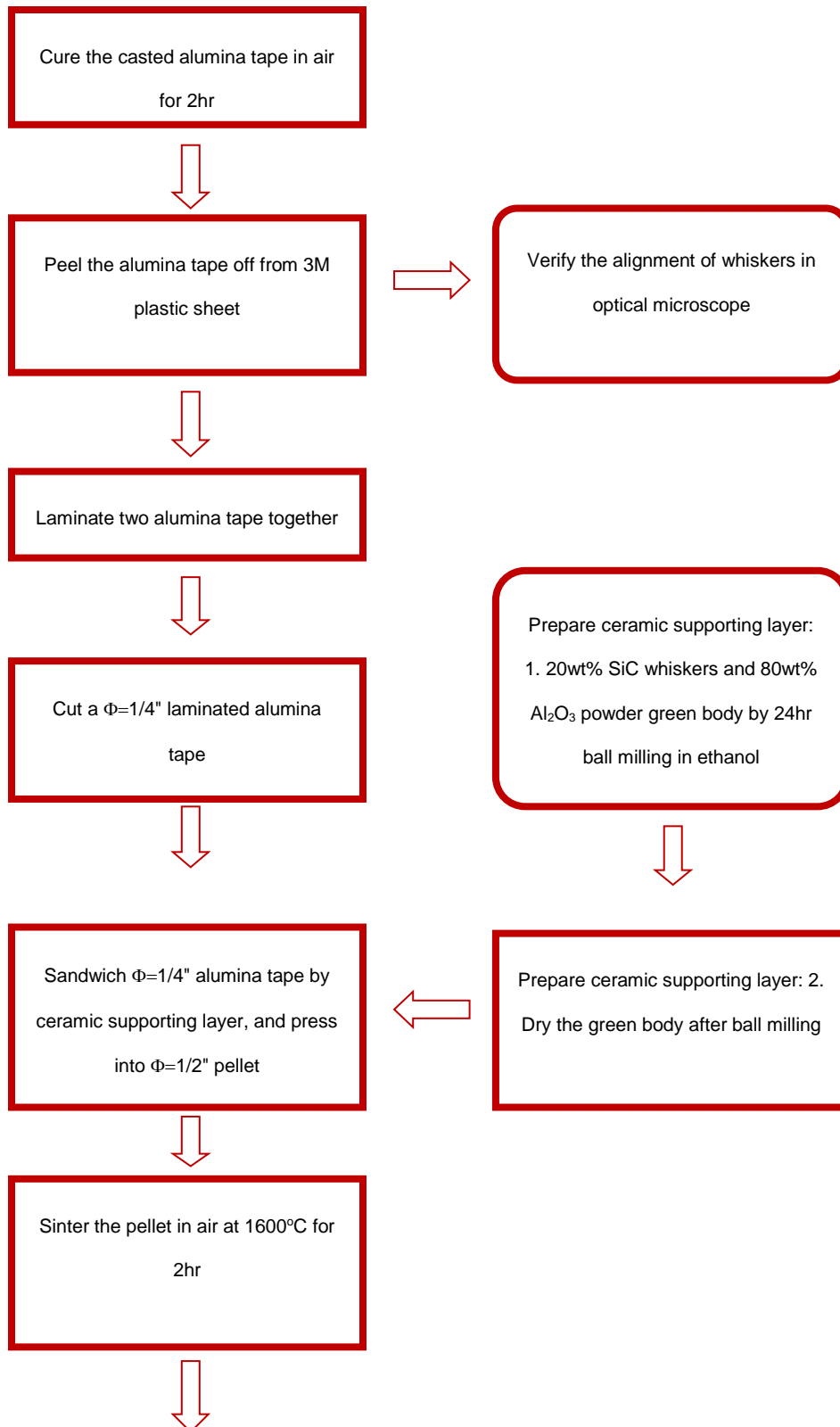
### 3.1.4 Sintering of Aligned SiC Whiskers in Alumina Green Tape

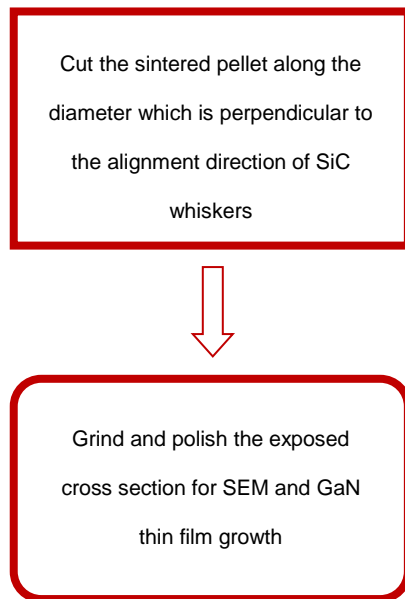
To avoid the oxidation of SiC whiskers, the sintering of tape-casted green sheet was protected in a mixture of alumina and SiC whiskers (weight ratio:  $\text{Al}_2\text{O}_3/\text{SiC}=4:1$ ). The mechanism of this protection is discussed in Chapter 5. A 1/4" diameter round green sheet was cut from the large tape-casted green sheet of alumina embedded with aligned SiC<sub>w</sub>, and then the 1/4" diameter green sheet was sandwiched between ceramic supporting layers composed of a mixture of alumina and SiC<sub>w</sub> and pressed into small cylindrical pellets (1/2" in diameter, 5 mm high) for sintering at 1600°C in air for 2 hr (Carver Laboratory Press, Model C, manufactured by Fred S. Carver Inc.; CM Inc. 1700 Series Rapid Temp horizontal tube furnace). A diamond wire saw (Well, Model 3032 Precision

Horizontal Diamond Wire Saw) was employed to cut the sintered pellet along the diameter. The exposed cross section of the pellet was polished by a diamond suspension and colloidal silica for characterization by XRD (Bruker D8 Advance Powder diffractometer, Cu K alpha1 radiation) and SEM (JEOL 7000F FE-Scanning Electron Microscope). The exposed pellet cross section was ready for III-nitride thin film growth at this point.

Since the alignment and manipulation of SiC whiskers involved many steps, a flow chart is shown in Flow Chart 3-1 to illustrate the process clearly.







**Flow Chart 3-1. Manipulation and alignment of SiC whiskers.**

## **3.2 Magnetron Sputtering Growth of GaN Thin Films**

### **3.2.1 Sputtering System**

A reactive sputtering system designed for III-nitride thin films growth is shown in Figure 3-6. A 6-inch diffusion pump (Varian, VHS-6, Serial # V182) was used to evacuate the chamber to high vacuum ( $1-2 \times 10^{-5}$  Torr) for thin film deposition. A residual gas analyzer (RGA 200, Stanford Research System) monitored the residual gas composition of the system in vacuum. The 2-inch diameter target was Ga metal (Alfa Aesar, 99.999%), and it was placed in a machined graphite cup (Graphite Machining, Inc., impurity level 5 ppm). The graphite cup with Ga metal was placed on the cathode of the magnetron gun (Angstrom Sciences,

ONYX<sup>®</sup>-2 Circular Magnetron). The power of the magnetron was controlled by a DC power supply (Advanced Energy Industries, Inc., MDX500). A substrate heater as well as a substrate holder (Detailed information is discussed in Section 3.2.3) was assembled for the high thin film deposition temperature requirement in this work (up to 1000 °C). The distance between target and substrate is 8cm. Ar and N<sub>2</sub> (Air Liquide Canada, 99.999%) were introduced into the system through a feedthrough which is in the center of the chamber's top plate so as to flow directly around the heated substrate.

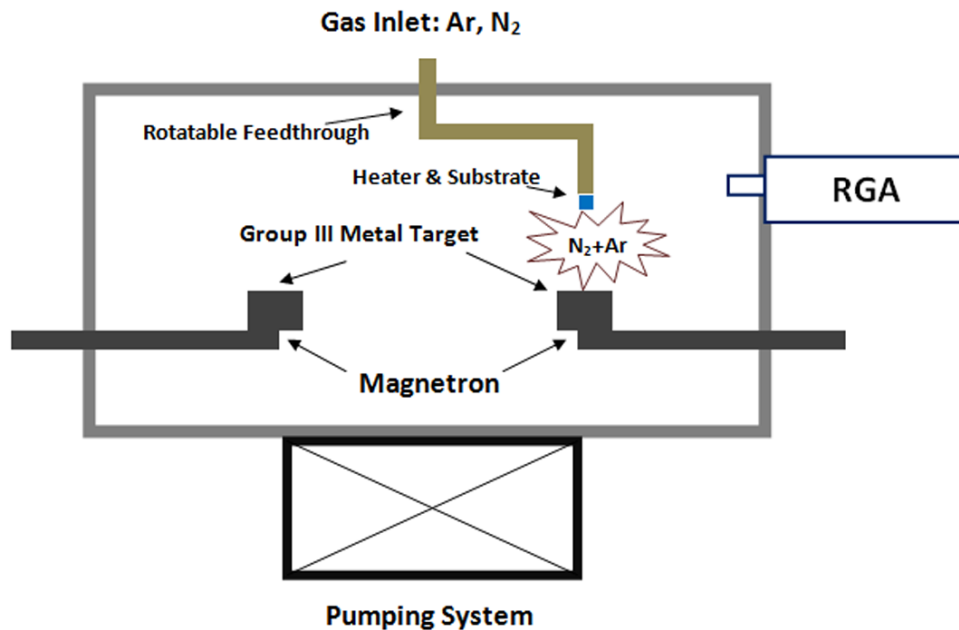


**Figure 3-6. Reactive DC-magnetron sputtering system for III-nitride thin films.**

Note that the feedthrough in the center of top plate is rotatable. This feature is designed for the deposition of multi-layer III-nitride thin films on the same substrate. Four magnetrons could be installed in the system, such that up to four

kinds of metal targets can be put on the cathode of each magnetron, respectively. For the deposition of InGaN thin film, In-Ga alloy can be used as the target. For the deposition of p-type GaN thin film, Ga-Mg alloy is the candidate of target. For the deposition of n-type GaN thin film, Ga-Si alloy is the candidate of target. In this thesis, however only one Ga target was employed.

### **3.2.2 Gallium Target Preparation and Target Container Selection**

Gallium is a metal with a low-melting point of 29.77 °C. The risk of placing gallium metal directly on the cathode of magnetron is melting. Freely flowing liquid gallium cannot be tolerated by the magnetron gun. Thus, a proper container was used for the placement of gallium.

Copper has excellent performance in terms of thermal and electrical conductivity. Oxygen-free high thermal conductivity copper cup (Angstrom Sciences, 99.99%, 2" diameter X 0.250" thick) was selected as the container for gallium metal. However, copper was found in the deposited GaN thin film by energy-dispersive X-ray spectroscopy (EDX) in SEM. This gave us a clue that copper might have diffused the gallium target. EDX results on the gallium target clearly showed that it is contaminated by copper. Thus, we stopped using a copper cup and switched to a graphite cup for gallium metal. The details are discussed in Section 5.1.

### 3.2.3 Substrate Heater

An alumina ceramic and tungsten based substrate heater was designed and assembled for GaN thin film growth. A diagram of the heater is shown in Figure 3-7. A tungsten heating basket is the core part of the heater. An alumina crucible was used as the heat shield. Two slots were drilled on the sidewall of an alumina crucible. The substrate was slid into the slot for GaN growth. Thus, the tungsten heating basket and alumina crucible made up a furnace for the substrate. The furnace was supported by two stainless steel rods as shown in Figure 3-7. Two copper rods were used to provide mechanical support to the stainless steel rods. The electrical power was also supplied by copper rods as they were connected to the electrical feedthrough of the chamber. A 1/4" stainless steel tube, directed from the rotatable feedthrough to the furnace, was used as the inlet for Ar and N<sub>2</sub>. The mechanical supports for the copper rods were achieved by stainless steel pins which penetrated through the copper rods to connect the 1/4" stainless steel tube. Thus, the whole substrate holder was mechanically supported by the rotatable feed through. In addition, to protect the magnets in the magnetron, a molybdenum plate was used as the heat shield to isolate the blackbody radiation from the tungsten heater.

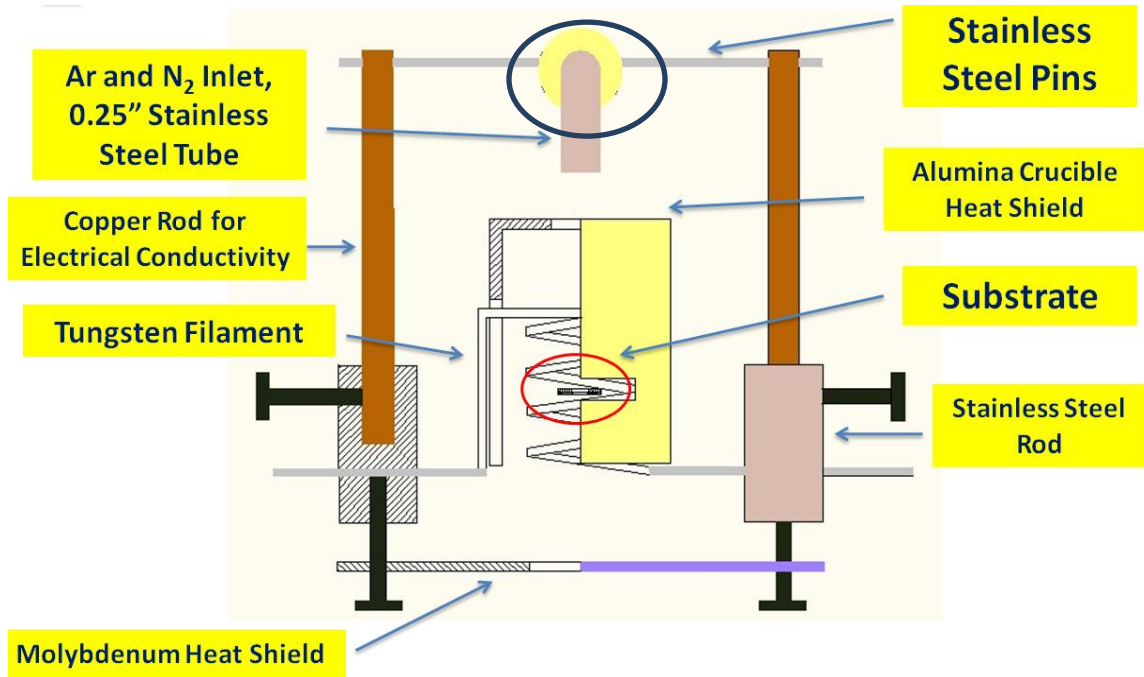
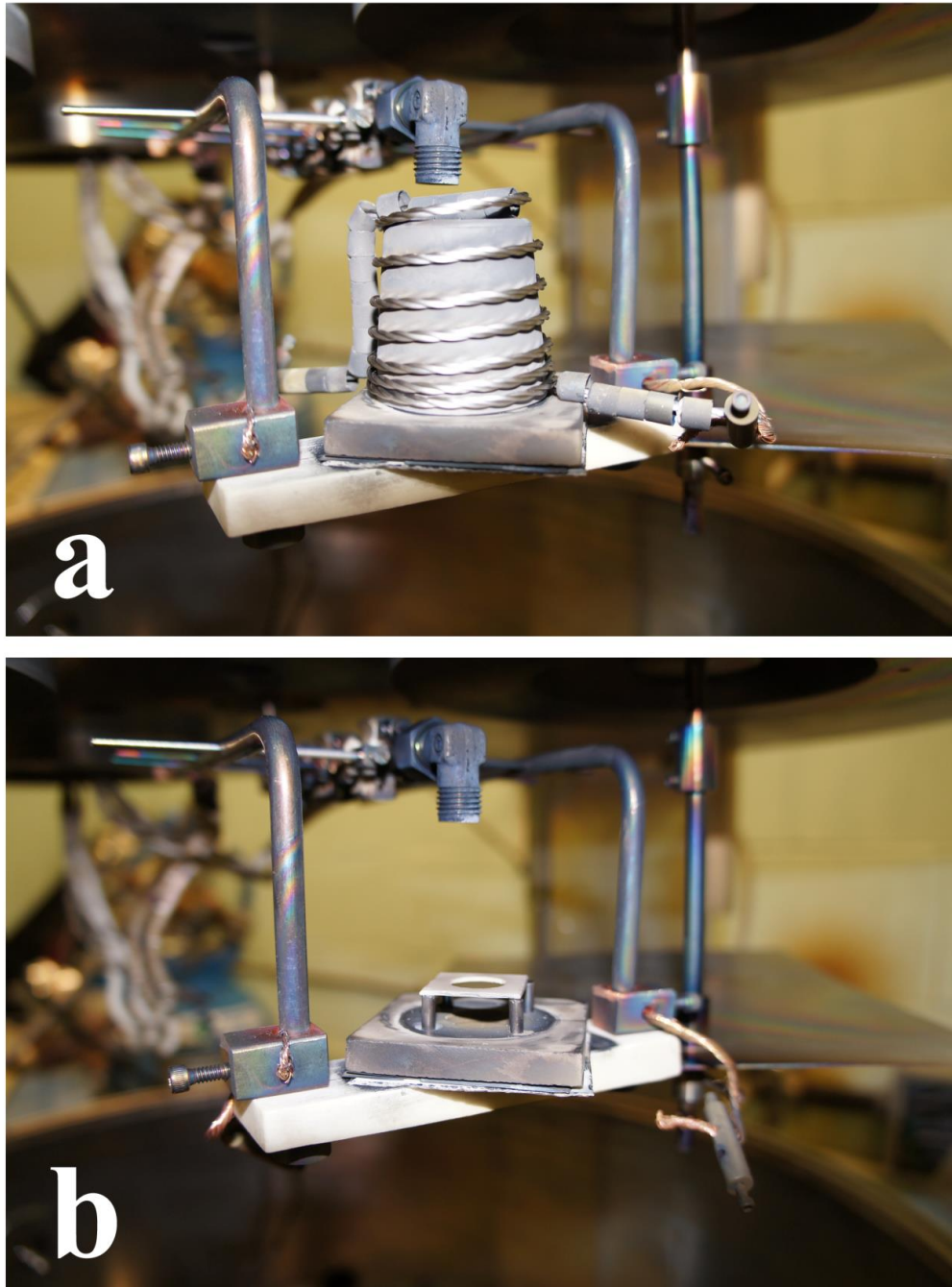


Figure 3-7. Design of substrate heater for GaN thin film growth.

A few problems arise during the growth of GaN thin films by using the initial design of the substrate heater: 1. Contamination of tungsten in the films, since there was no shield between the tungsten basket and the substrate; 2. Brittleness of alumina screws, because molybdenum is conductive, metallic screws cannot be used to assemble the molybdenum shield to avoid short circuit. Alumina screws were used instead of metallic ones, however, due to the brittleness of alumina, these screws were quite easy to break. Thus, a few modifications were made to the substrate heater [178].

As shown in Figure 3-8, an alumina crucible was placed in the tungsten heating basket as the shield. No slots were drilled on the sidewall of the crucible to avoid the contamination of tungsten. The substrate holder, as shown in Figure 3-8b was redesigned at this point, as the holder needed to be placed inside the alumina crucible. Four alumina posts were placed to support an alumina plate, which was the substrate holder. Meanwhile, to avoid the use of brittle alumina screws, an alumina support beam made using an alumina boat was used to replace the molybdenum plate.



**Figure 3-8. The substrate heater for GaN thin films growth (modified from the design as show in Figure 3-7). a, the alumina crucible was placed in the tungsten heating basket as the insulation shield; b, the substrate holder.**

### 3.2.4 GaN Thin Film Growth Procedure

The growth procedure of GaN thin film in the reactive magnetron sputtering system is summarized as following:

1. Substrate cleaning: wash sapphire wafer, Si wafer, SiC wafer, or ceramic substrates in acetone, methanol, ethanol, sulfuric acid, hydrochloric acid;
2. HF treatment: Dip Si wafer, SiC wafer, or ceramic substrate into HF buffer solution ( $\text{NH}_4\text{F} : \text{HF} = 10 : 1$ ) before load into vacuum chamber to clean native oxide layer on the surface;
3. Load the substrate into the chamber;
4. Pump the system to  $1\sim 2 \times 10^{-5}$  Torr as the base pressure;
5. Heat the substrate up to  $800^\circ\text{C}$ - $900^\circ\text{C}$ , to eliminate residual oxide on the substrate;
6. Introduce Ar, keep shutter closed, presputter Ga target for 5min to get rid of any contamination on the target;
7. Reduce the substrate temperature to  $650^\circ\text{C}$ , open the shutter, presputter a Ga nucleation layer on the substrate for 5min;
8. Close the shutter, increase the substrate temperature to  $700^\circ\text{C}$ , introduce  $\text{N}_2$ , adjust working pressure to 9mTorr, set magnetron power at 100W;
9. Turn on the power supply of magnetron, check the status of plasma, open the shutter if the plasma is stable, start GaN thin film growth;

10. After growth, turn off power supply and substrate heater, cool the growth system down to room temperature in N<sub>2</sub> atmosphere.

## 3.3 Characterization

### 3.3.1 XRD

In this work, powder XRD scan mode (Bruker D8 Advance Powder diffractometer, Cu K alpha1 radiation) was used to determine the phase and in-plane orientation of GaN thin films. It was also used for the characterization of the degree of alignment of SiC whiskers and ceramic substrate sintering behavior. The XRRC scan mode was used to determine the crystallinity of GaN thin films. Pole figures scanned by 2D-XRD (Bruker D8 Discover diffractometer with a Co sealed tube source, parallel focusing mirror, pinhole collimation, ¼ chi eulerian cradle, XYZ specimen stage, and a Vantec 500 area detector, 2θ range 29-59 degrees) were used to interpret the orientation relationship between GaN epilayers and SiC-substrates. The scanning methods of powder XRD, 2D-XRD, and XRRC are summarized below.

The setup for conventional XRD is shown in Figure 3-9. The diffraction measurement is limited by the detection circle, which is in the diffractometer plane. A point detector is usually used for the  $2\theta$  scan along the detection circle.

Thus, the variation of diffraction pattern, which is considered as the diffraction signal along the Z-direction, cannot be collected by the point detector in the detection circle. The X-ray beam comes in the form of a line focus (a solar slit is used to achieve this, the width of the line focus is also called the size of the X-ray beam). The diffraction pattern collected in a conventional diffractometer is considered as a superposition of several layers of the diffraction pattern within the diffractometer. It is quite obvious that the diffraction data out of the diffractometer plane cannot be detected by the point detector [179].

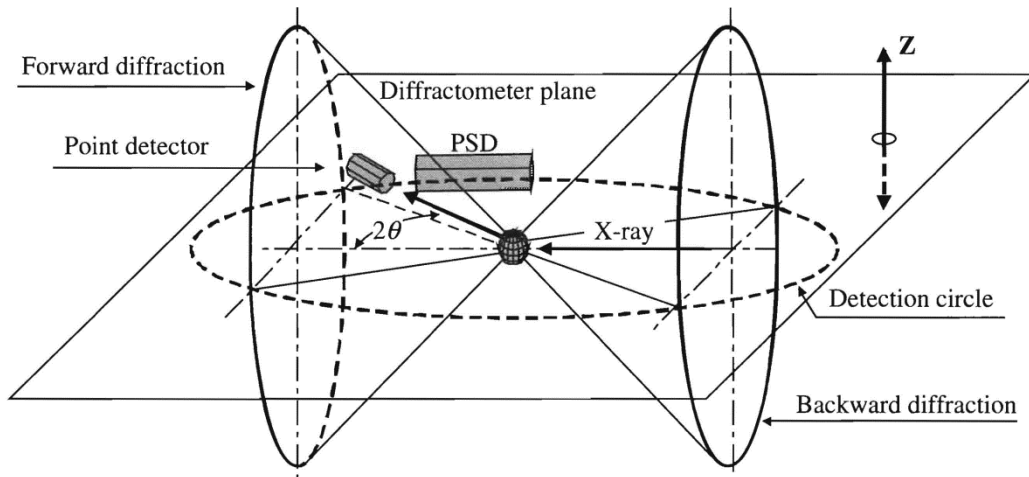


**Figure 3-9. Diffraction patterns in 3D space from a powder specimen and the diffractometer plane [179].**

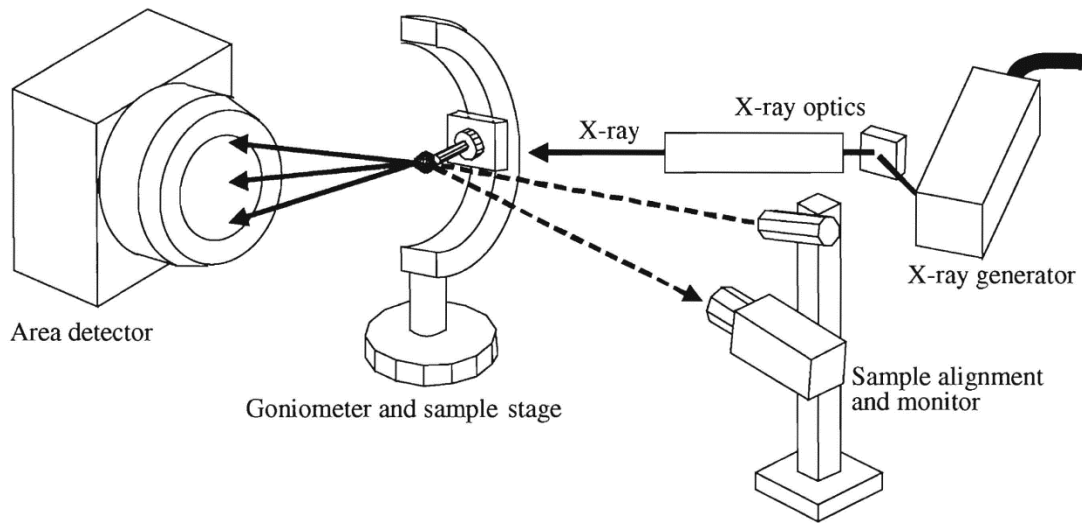


**Figure 3-10. Five basic components in a 2D-XRD system: X-ray source; X-ray optics; goniometer and specimen stage; specimen alignment and monitor; area detector [180].**

Since the actual diffraction pattern is distributed in 3D space around the specimen being diffracted, a two-dimensional X-ray diffraction (2D-XRD) technique has been developed with a two-dimensional detector. A typical 2D-XRD system usually comprises five basic components [180] as shown in Figure 3-10:

- X-ray Source: X-rays with required energy, focal spot size and intensity are produced from the source;
- X-ray Optics: tunes the X-ray beams to the desired wavelength, beam focus size, beam profile, and divergence;
- Goniometer and Specimen Stage: establishes and manipulates the geometric relationship between primary beam, specimen, and detector;

- Specimen Alignment and Monitor: aids users with positioning the specimen into the center of the instrument and monitors the status of the specimen during scanning;
- Area Detector: records the diffracted X-rays from a specimen, and saves the diffraction pattern in the form of 2D frame.

In addition, the XRRC is considered as an effective tool to characterize the crystallinity of single crystal thin films. In a conventional powder diffraction mode, specimen and detector both rotate to maintain  $\theta$ - $2\theta$  relationship. For the measurement of an XRRC, the detector does not rotate to keep a required  $2\theta$  angle with the X-ray source, but the specimen does rock within the diffractometer plane. The starting point of specimen rocking is the position which satisfies the  $\theta$  angle of the interested diffraction peak.

### **3.3.2 SEM**

The topographic information of specimens in this work was characterized by secondary-electron imaging in JEOL JSM-7000F field-emission scanning electron microscope. Backscattered electron imaging technique, together with energy-dispersive X-ray spectroscopy were used to characterize compositional information in the specimen. To improve the electron conductivity of the

specimens, they were mounted on the SEM stub by a two-sided carbon tape, and coated with a thin layer of carbon or platinum.

### 3.3.3 STEM

In this work, a STEM (aberration-corrected FEI Titan 80-300 Cubed microscope) was used to characterize the GaN/SiC interface status, as well as detailed crystal structural information of GaN thin films and 6H-SiC substrates. The cross sections of STEM specimens were prepared by multi-preparation method.  $\{11\bar{2}0\}$  planes of 6H-SiC wafers were selected as the observation plane in STEM. One piece of 6H-SiC wafer with GaN deposited was cut into two pieces along a  $(11\bar{2}0)$  plane, and then the two pieces were glued together on the GaN side with the alignment of  $\{11\bar{2}0\}$  planes by epoxy. After that, it was cut into 1mm X 2mm X 0.7mm flakes using a diamond wire saw and then glued on a TEM wedge thinning paddle. All of the flakes were polished on the  $\{11\bar{2}0\}$  planes via Allied MultiPrep™ equipment with polishing papers having 9 μm, 6 μm, and 3 μm particle size, respectively. Once the polish on one side of the flakes was done (mirror finish), they were rotated top (shiny) side down and polished down to 300 μm thickness on the other side with the same polish sequence as on the first side. After that, the flakes were tilted by 4° to create a low polish angle, and the thickness of the wedge of the flake continued to be reduced by polishing with 1

$\mu\text{m}$  polish paper. When the thickness of the wedge was reduced to a few hundred nanometers, the polish was finished and the wedge specimens were transferred and glued onto a molybdenum ring by epoxy. Finally, the specimens were ion milled with 0.25-1.5 KeV  $\text{Ar}^+$  ions in a Gentle Mill™ to make the specimens transparent to the electrons.

In a STEM, a sub nanometer (or atomic size) probe is used to scan over the specimen in a raster. A high-angle annular detector is employed in the STEM to collect signals from high-angle elastically scattered (Rutherford-like [181]) electrons for high-angle annular dark-field (HAADF) images, which directly relate to the atomic number of each atom ( $\sim$ proportional to  $Z^{1.7}$ ) [182]. On the other hand, HAADF imaging is not strongly affected by dynamical diffraction effects, defocus, and sample thickness variations [183]. Thus, in this work, HAADF imaging can provide atomic level characterization of GaN/SiC interfaces, GaN thin films, and 6H-SiC substrates. Annular bright field (ABF) imaging is also employed in this work for phase contrast since HAADF imaging is insensitive to light weight atoms and atoms in an amorphous phase. The central signal with highest intensity is collected by a parallel electron energy-loss spectrometer (Gatan 866 model) for electron energy-loss spectroscopy (EELS). Typically an electron energy-loss spectrum includes three parts [182]: 1) zero-loss peak, generated by elastic scattering and no-loss electrons, and it also includes phonon losses ( $<0.1$  eV); 2) low-loss peaks ( $<50$  eV), inter- and intra-band transitions, together with plasmon excitations; 3) core loss peak ( $>50$  eV), corresponding to

the excitation energy of atomic electrons in inner shells by transmitted electrons. In this work, the inner-shell ionization edge (from 50eV to a few KeV) in the EELS spectrum are used to identify which elements are present in the GaN/SiC interface since core-electron binding energies differ for each element and each type of shell [184].

## **4 Results and Discussion: Manipulation and Alignment of SiC Whiskers for GaN Thin Film Growth**

### **4.1 Alignment of SiC Whiskers**

As mentioned in Chapter 3, in order to apply SiC<sub>w</sub> on a 3M plastic sheet, a dilute SiC<sub>w</sub> aqueous suspension (2mg SiC<sub>w</sub> in 10mL suspension) with surfactant concentration of 0.3mg/ml was prepared. SDS (known as a surfactant), in an ultrasonic bath, was used to improve the dispersion of the whiskers in the suspension. The whiskers in aqueous suspension were applied onto the surface of 3M plastic sheet by a dropper. As shown in Figure 4-1, the whiskers in the suspension would line up along the direction of the parallel grooves on the 3M sheet. Due to the narrow space at the bottom of this 3M template (see Figure 3-4 for detailed cross section), only one individual whisker will be allowed to sit there, and the sidewalls of the groove can provide sufficient lateral force onto the individual whisker. With the advantage of the small space of the groove, together with the sufficient lateral force, the SiC<sub>w</sub> can line up along the groove spontaneously.

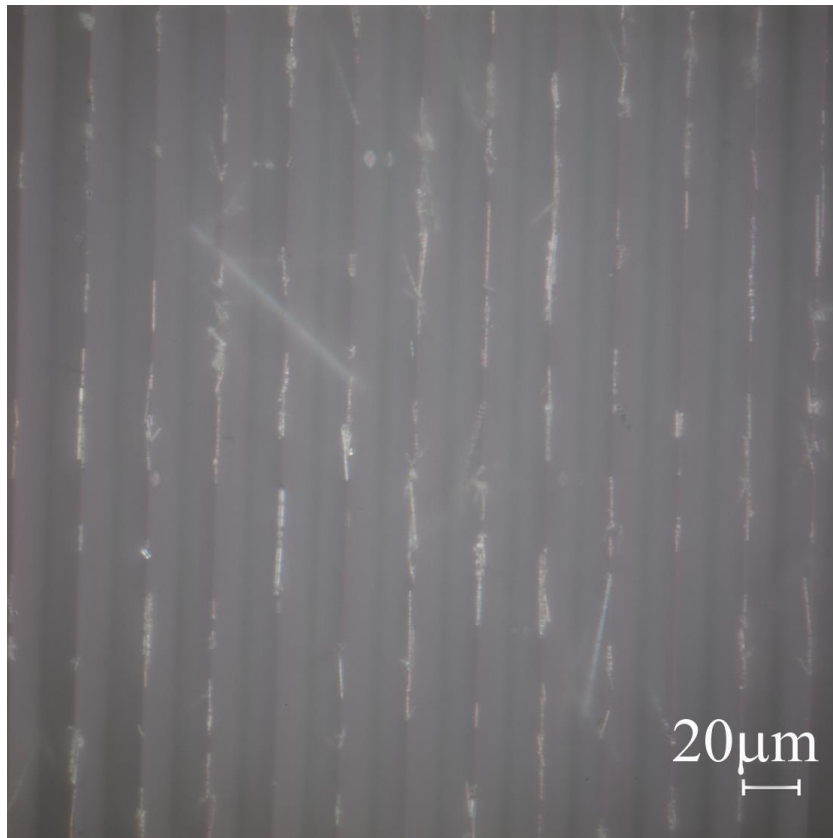


**Figure 4-1. The aligned SiC<sub>w</sub> on the surface of 3M 90/24 BEF. The whiskers are driven down by gravity all the way to the bottom of the groove.**

For comparison, the SiC<sub>w</sub> suspension was also applied onto the surface of another template with wider parallel grooves as shown in Figure 4-2. This template has an obtuse angle at the bottom, and the width of the groove is 200 μm. Unlike 3M 90/24 BEF, this template can provide a large space at the bottom, which can facilitate the whiskers to distribute randomly. In summary, a small angle at the bottom is essential for a template to line up SiC whiskers precisely.

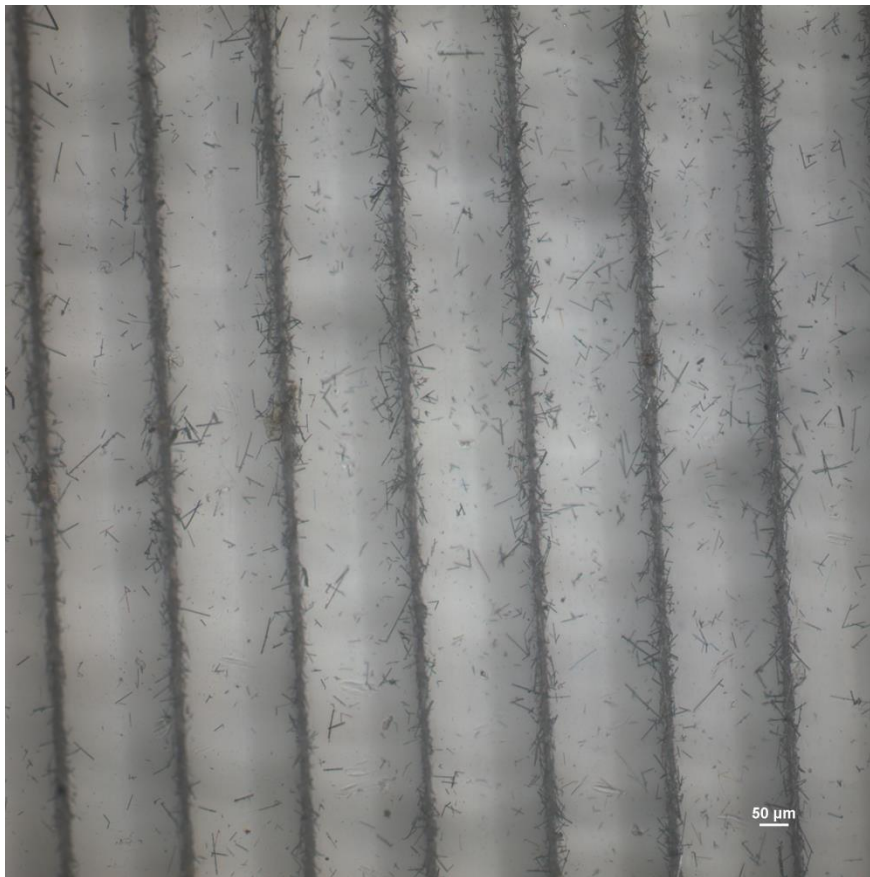


**Figure 4-2. SiC whiskers on the surface of a plastic sheet template with wider parallel grooves and larger bottom angle than 3M BEF plastic sheet. Note that the whiskers on this template appear more randomly than whiskers on 3M as shown in Figure 4-1.**

To characterize the alignment degree of SiC whiskers on the 3M BEF plastic sheet by XRD and SEM, an aqueous environment is not suitable for handling and operation, as the XRD sample stage is rotatable during  $\theta$ - $2\theta$  scanning, and sample room for the SEM is in ultra high vacuum. Latex rubber was used in this work to form a solid matrix for the aligned whiskers prior characterization by XRD and SEM. Latex can mix with water homogeneously, and it can be cured in air to

form a solid gel. Once it is cured, it can be peeled off from the 3M BEF plastic sheet while maintaining whisker alignment. The surface pattern of the 3M plastic sheet can be duplicated onto the latex surface as well. For XRD characterization, no diffraction peaks can be detected from latex as latex does not contain any crystalline phase, so the diffraction signal from SiC whiskers can be clearly identified.

The mechanism of alignment degree estimate of SiC whiskers by XRD is shown in Figure 4-3. The  $\theta$ - $2\theta$  scan of XRD can detect the diffraction signals from the crystalline planes which are parallel to the sample holder. Once the whiskers are well aligned, (111) planes of cubic SiC are not detectable by XRD as they are not parallel to the sample holder, but perpendicular to it. However, (220) planes of 3C-SiC, which are equivalent to  $(2\bar{2}0)$  planes, are perpendicular to the (111) planes (thus parallel to the XRD sample stage) and are detectable by XRD. Thus, we can use the peak area ratio of XRD peaks corresponding to (111) and (220) planes of 3C-SiC ( $I_{(220)}/I_{(111)}$ ) to characterize the degree of SiC whisker alignment. This value for powder 3C-SiC is 0.35 according to standard XRD pattern of 3C-SiC (PDF #29-1129), and it will increase due to a higher degree of SiC whisker alignment. In this work, integrated peak intensities for (111) and (220) planes of SiC whiskers are 0.090 and 0.373, respectively. Thus,  $I_{(220)}/I_{(111)}$  increased to 4.14 according to the diffraction pattern shown in Figure 4-4. This whiskers alignment degree value is higher than the alignment degree value of SiC whiskers achieved

by extrusion ( $I_{(220)}/I_{(111)}=2.3$ , reading from Fig. 3 in paper [8]) by Goto and Tsuge [8].

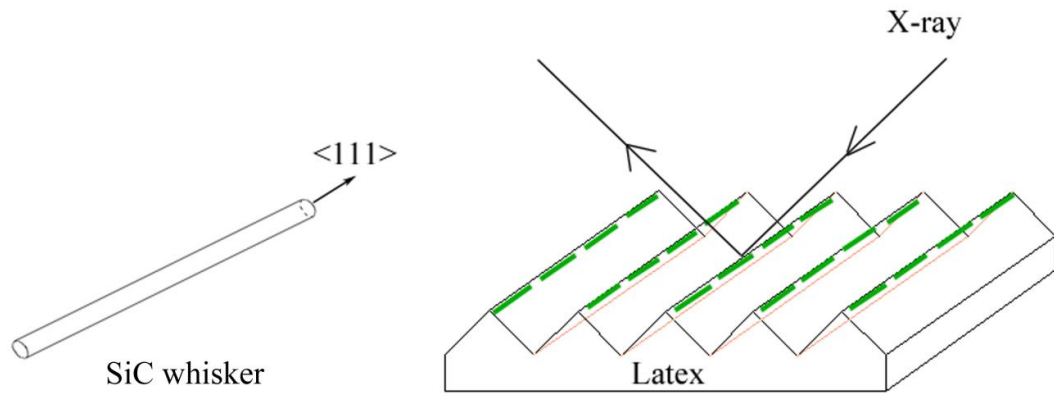


Figure 4-3. Set up for XRD characterization for the alignment degree of SiC whiskers (redrawn from [8]).

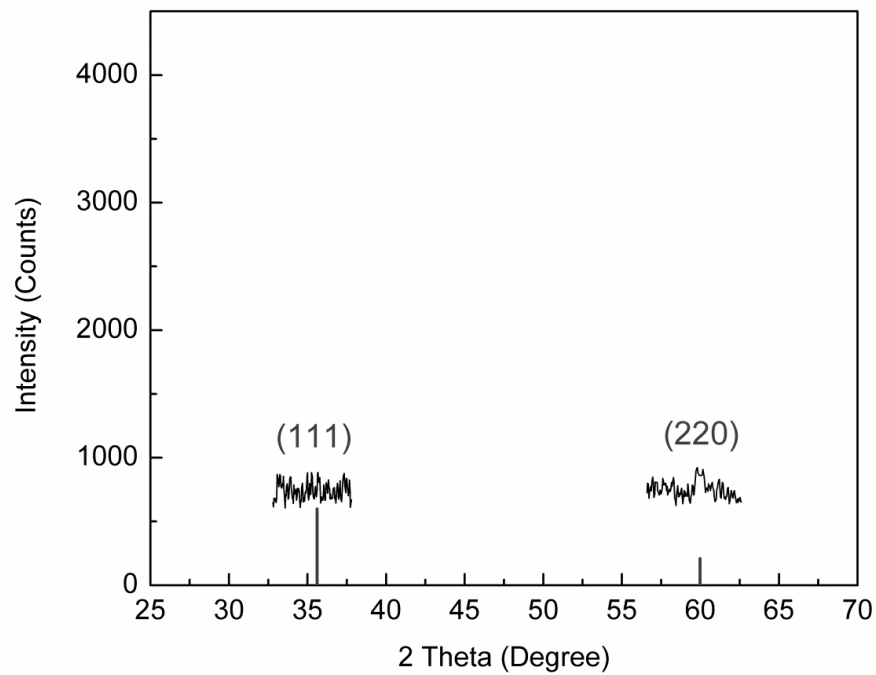


Figure 4-4. XRD pattern of aligned SiC whiskers.

As the  $I_{(220)}/I_{(111)}$  ratio does not reflect the difference between unidirectional alignment and two-dimensional orientation, optical microscopy and SEM were used to provide further information regarding unidirectional alignment as shown in Figure 4-5 and Figure 4-6 respectively. In Figure 4-5, we can see that the whiskers and latex rubber have a stronger contrast in an optical microscope image than the contrast between whiskers and aqueous layer as shown in Figure 4-1. In Figure 4-5, it is clear that most whiskers can stay aligned with the direction of a latex groove which is duplicated from the 3M plastic sheet (this duplication provides us an alignment reference). In detail, once the surface pattern of the 3M BEF plastic sheet was duplicated onto the latex rubber, the ridge on the rubber corresponds to the bottom of the groove of the 3M BEF plastic sheet. Thus, we are able to find the aligned whiskers along the ridges of latex rubber. In the SEM image as shown in Figure 4-6, we can see that the aligned whisker in the center is parallel to the direction of the grooves and ridges. Note that the number of whiskers in the secondary electron image (SEI) of the SEM is less than that in optical microscope image, but it is normal as SEI only reflects topographic information (10nm deep) of the specimen. Thus, with the quantitative analysis of the XRD pattern, together with the direct observation of unidirectionally aligned whiskers along the direction of a groove, we can conclude that  $\text{SiC}_w$  can be lined up along its growth direction, which is consistent with the  $\langle 111 \rangle$  crystalline direction.

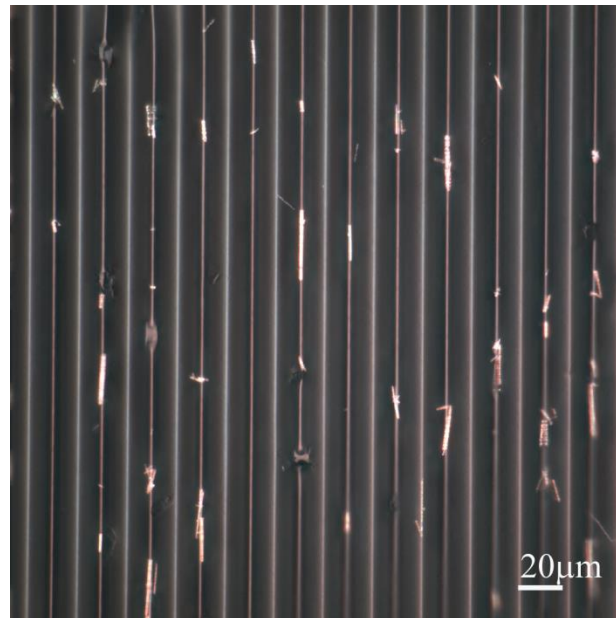


Figure 4-5. Optical microscope image of the aligned SiC whiskers in latex rubber.

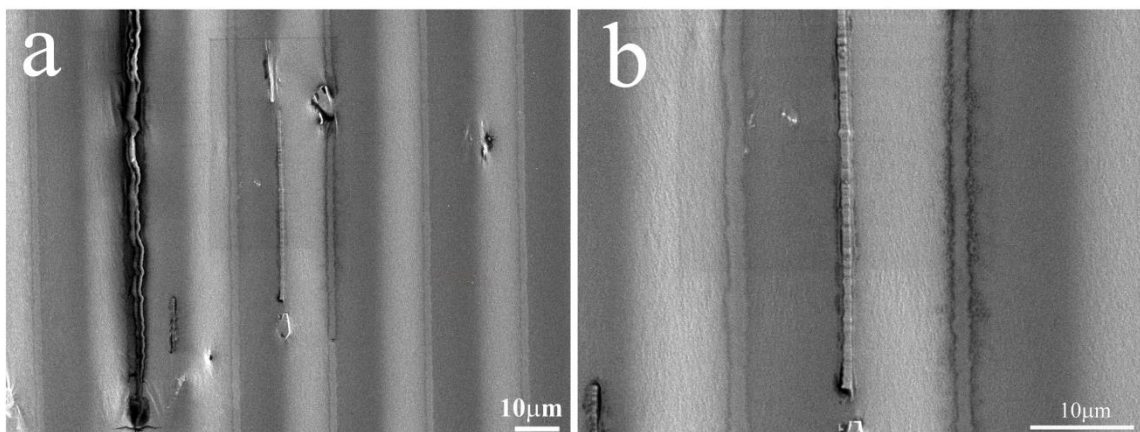


Figure 4-6. SEM images of aligned SiC whiskers in latex rubber. Note that the ridge of rubber latex corresponds to the bottom of the 3M BEF plastic sheet, thus the aligned whiskers stay on the ridge of rubber latex. Because the secondary electron images in SEM can only reflect topographic information, the amount of visible whiskers in SEM images is less than that in optical microscope images.

## 4.2 Transfer of Aligned SiC Whiskers

Latex rubber is not a suitable candidate for the use of the aligned SiC<sub>w</sub> for III-nitride thin film growth at an elevated temperature. A high temperature-compatible matrix is essential to hold the aligned whiskers instead of the latex rubber. Alumina is a good candidate to hold the aligned whiskers for III-nitride thin film growth. It's thermally stable up to 2000°C, and it has very low vapor pressure which is ideal for vacuum based thin film growth technique. By sintering, alumina can become a rigid ceramic matrix for safe handling. Thus, at this point, to transfer aligned whiskers into an alumina matrix, one viable method needs to be developed for the transfer of aligned whiskers from either latex rubber or 3M BEF plastic sheet surface.

It is difficult to transfer the aligned whiskers from the latex rubber, as the whiskers are embedded into the rubber matrix. Scotch® tape, epoxy, or Gel-Pak® film was used in an attempt to pick up the whiskers from the rubber but failed, as the adhesive force between these materials and the whiskers is not sufficient to remove the whiskers from the latex rubber. Thus, it is not a good idea to transfer the aligned whiskers from the latex rubber.

The other option is to transfer the aligned whiskers from the 3M BEF plastic sheet surface. The challenge in this option is the aqueous environment, which is difficult to handle due to its fluidity. Fluidity is a potential disruptive factor which can destroy the alignment of the whiskers. To eliminate the aqueous environment, the

specimen was placed in air for the water to evaporate. After approximately 8 hours, the specimen became totally dry. Optical microscope images were taken on the dried specimen indicate that most of the dried whiskers can stay aligned on the 3M BEF plastic sheet as shown in Figure 4-7.

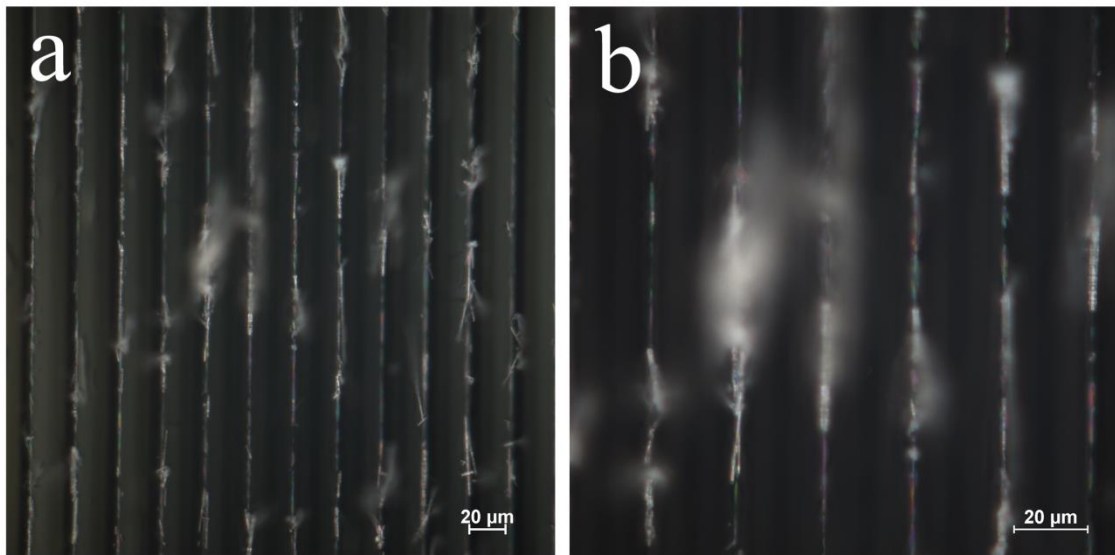


**Figure 4-7. Optical microscope images of dried SiC whiskers on 3M BEF plastic sheet. Note that the whiskers stay aligned at the bottom of the parallel groove on 3M plastic sheet.**

Tape casting was selected to apply alumina slurry onto the 3M BEF plastic sheet to transfer aligned whiskers. Several tape casting experiments were conducted on silicone-coated Mylar film for a slurry preparation study. As the image shown in Figure 4-8a, the tape-casted sheet from nano-alumina [average particle size (APS) 45-55 nm powder, Alfa Aesar] always tends to crack after curing due to its large surface area (30-40 m<sup>2</sup>/g). Thus, alumina with a smaller surface area (<1

$\mu\text{m}$  APS powder, surface area=10  $\text{m}^2/\text{g}$ , Alfa Aesar) was used instead of nano-alumina for tape casting and the image in Figure 4-8b demonstrated that the casted sheet is intact. The recipe used for alumina slurry preparation is listed in Section 3.1.3.1.

Alumina slurry was directly applied onto the 3M BEF plastic sheet by tape casting. After 2hr curing, the alumina green tape can be peeled off from the 3M BEF plastic sheet with aligned whiskers embedded in it as shown in Figure 4-9. Note that the tape-casted alumina green sheet can effectively duplicate the surface pattern of the 3M plastic sheet. The aligned silicon carbide whiskers are shown parallel to the direction of the grooves which is evidence for the alignment.

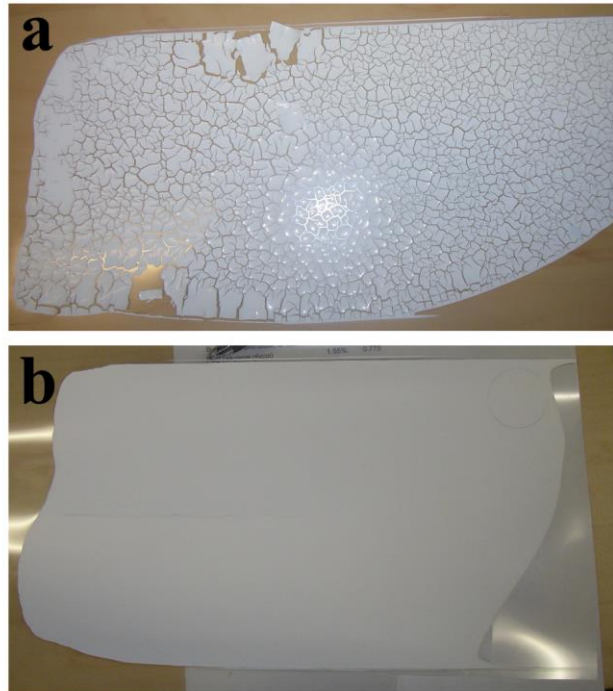


**Figure 4-8. Tape-casted alumina green sheet on silicone-coated Mylar film. a, nano-alumina (45-55 nm APS powder, surface area = 30-40 m<sup>2</sup>/g) is the raw material; b, micron-alumina (<1 μm APS powder, surface area = 10 m<sup>2</sup>/g) is the raw material.**

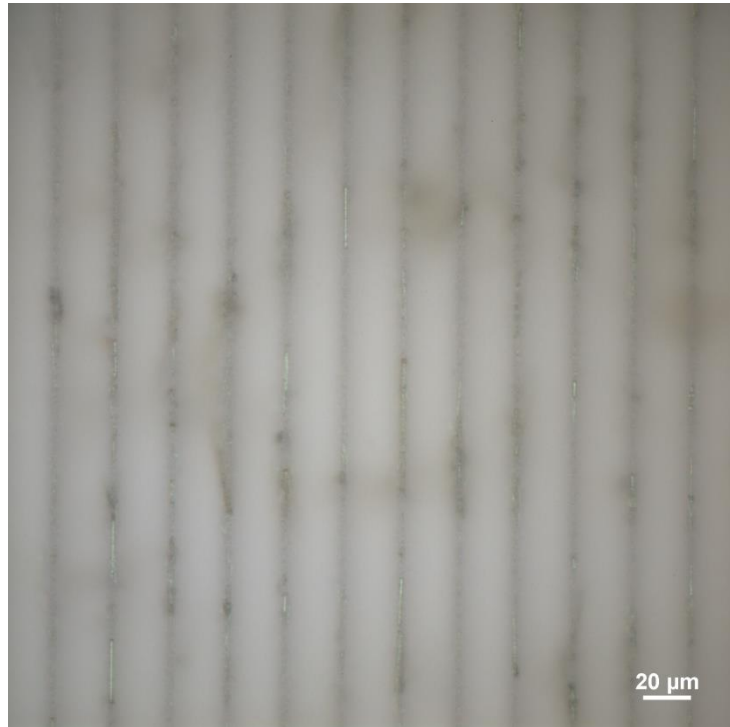


**Figure 4-9. Optical microscope image of aligned silicon carbide whiskers in alumina green tape. The whiskers are aligned vertically in the image.**

### **4.3 Sintering Behavior of SiC Whiskers in Alumina Matrix**

Sintering is an essential step to prepare a high-density, alumina ceramic-based rigid substrate. The main challenge for sintering in this work is the oxidation of SiC whiskers in air (SiC started to be oxidized in air at 700°C). On the other hand, alumina tape is too thin and too brittle to handle safely, so it is ideal if the alumina tape can be transferred into a ceramic pellet for easy manipulation. Thus, a

proper way to sinter the alumina tape with aligned SiC whiskers was developed in this work.

#### **4.3.1 Development of Self-Regulating Sintering Technique of Random Silicon Carbide Whiskers in Alumina Matrix**

We started the study of SiC sintering behavior with randomly distributed SiC whiskers. A sintering experiment was designed as follows to investigate sintering behavior of SiC whiskers in an alumina matrix in air:

- 1) Mix SiC whiskers with alumina powder in a weight ratio of 1:4 by ball milling for 25 hr, and then press the mixture into pellet (1/2" in diameter, 5 mm high);
- 2) Sinter the pellet in air at 1600°C for 2hr. The color of the pellet shell changed from green to white by sintering;
- 3) Grind the pellet down by 3mm.

A top view drawing of the ground sample is shown in Figure 4-10. The outside shell of the sintered pellet is white, which was changed from green by sintering. However, after grinding, the center part of the sintered pellet still appears green (area 1 in Figure 4-10). Three phases are found in the sintered pellet by XRD as shown in Figure 4-11: 3C-SiC, Al<sub>2</sub>O<sub>3</sub>, and mullite. The existence of 3C-SiC phase in the sintered pellet directly demonstrates SiC in the pellet has not been

completely oxidized by sintering, which implies unoxidized SiC is protected by some unknown mechanism from being oxidized during sintering. Alumina still exists (or at least partially exists, to be rigorous) in the pellet after sintering. Moreover, mullite ( $\text{Al}_6\text{Si}_2\text{O}_{13}$ , white), which does not exist in the green pellet, was found in the sintered pellet by XRD.

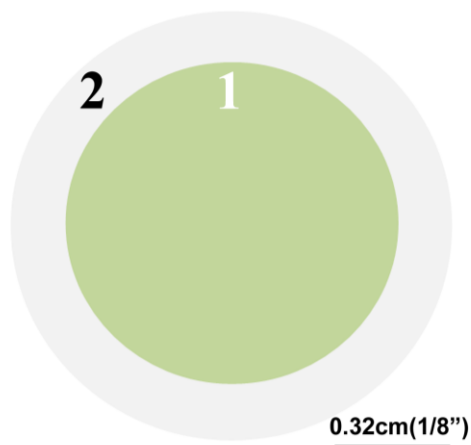


**Figure 4-10. Top view drawing of the sintered pellet after grinding. Area 1, sintered SiC whiskers in alumina matrix; area 2, mullite formed by sintering.**

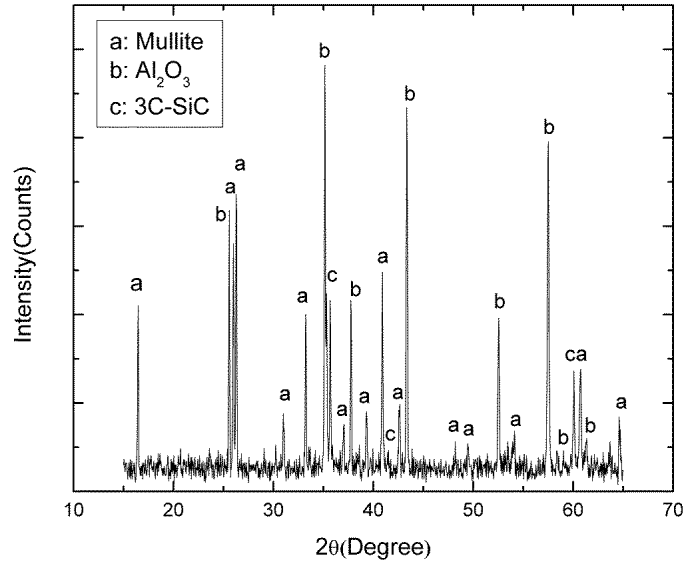


**Figure 4-11. XRD patterns of the sintered pellet.**

From a color point of view, SiC should stay in the green area of the pellet, which corresponds area 1 as shown in Figure 4-10. Mullite probably corresponds to area 2 in Figure 4-10, which is the white ring area in the pellet. EDX was used to study elemental distributions in the sintered pellet in SEM. Figure 4-12 shows the EDX results on the green/white area interface the sintered pellet. The green area sits on the left hand side of the image while the white area is on the right hand side. By carefully studying the results, we can find: 1. The peaks in Si and C spectra appear in the same position (on the left hand side of the scan line in the electron image in Figure 4-12), but Al and O signals are weaker in that position, which indicates that there is SiC in that position; 2. On the right hand side of the scan line, there are a few pits on the specimen surface, which result in the signal intensity drop in all of the elemental spectra at the same time; 3. Ignoring the influence of topography, the distribution of Al and O does not change dramatically

along the scan line. Another set of EDX line scan results as shown in Figure 4-13 also demonstrates the observation in Figure 4-12.

The observation of the EDX line scan on the green/white area interface demonstrates that the distribution of SiC in the sintered pellet does coincide with the green area distribution. EDX mapping together with a backscattered electron (BSE) image in the SEM were conducted on the green area of the sintered pellet to find a detailed image of the existence of SiC whiskers and the results are shown in Figure 4-14. Si and C are essentially concentrated in areas labeled as 1 in the images, Al and O are essentially concentrated in areas labeled as 2 in the images. The appearance of areas 1 coincides with the appearance of SiC whiskers (large aspect ratio). This directly demonstrates the existence of SiC whiskers in the green area of the sintered pellet.

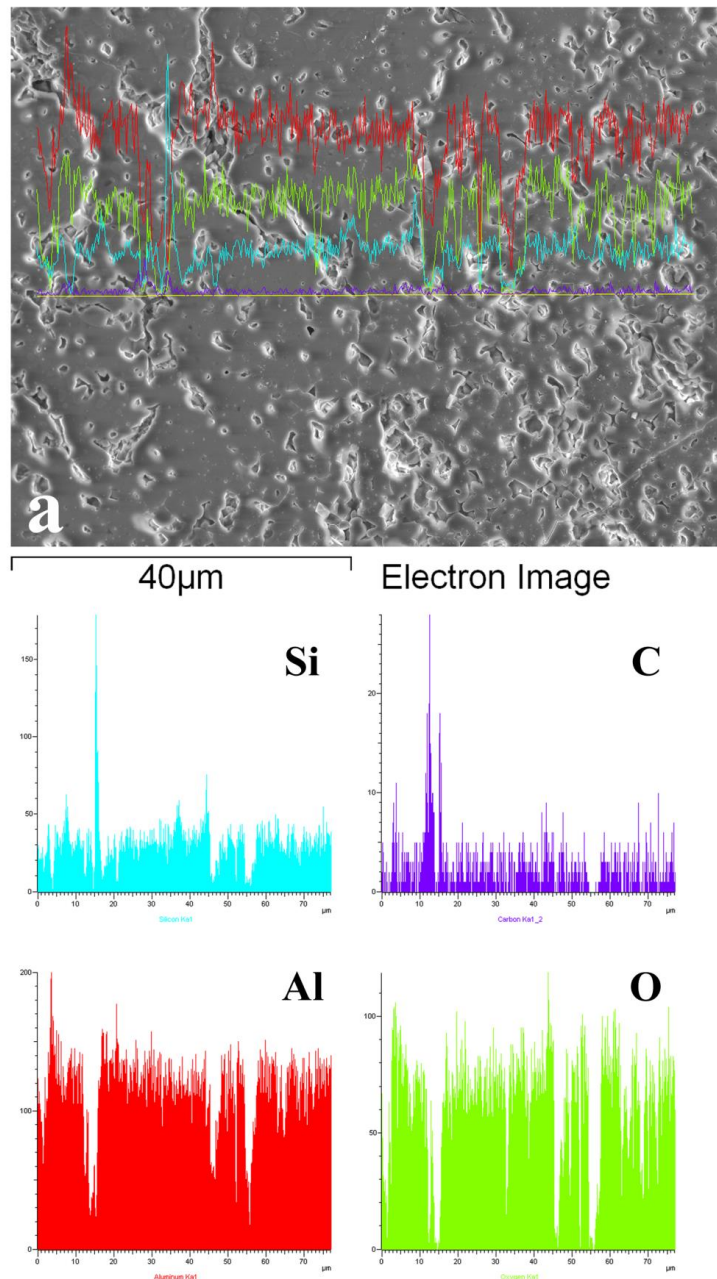


Figure 4-12. EDX line scan at the interface between  $\text{Al}_2\text{O}_3\text{-SiC}_w$  mixture and mullite. a. EDX line scan results shown in the electron image of the scanned area; EDX spectra of Si, C, Al, and O are shown below figure a, respectively.

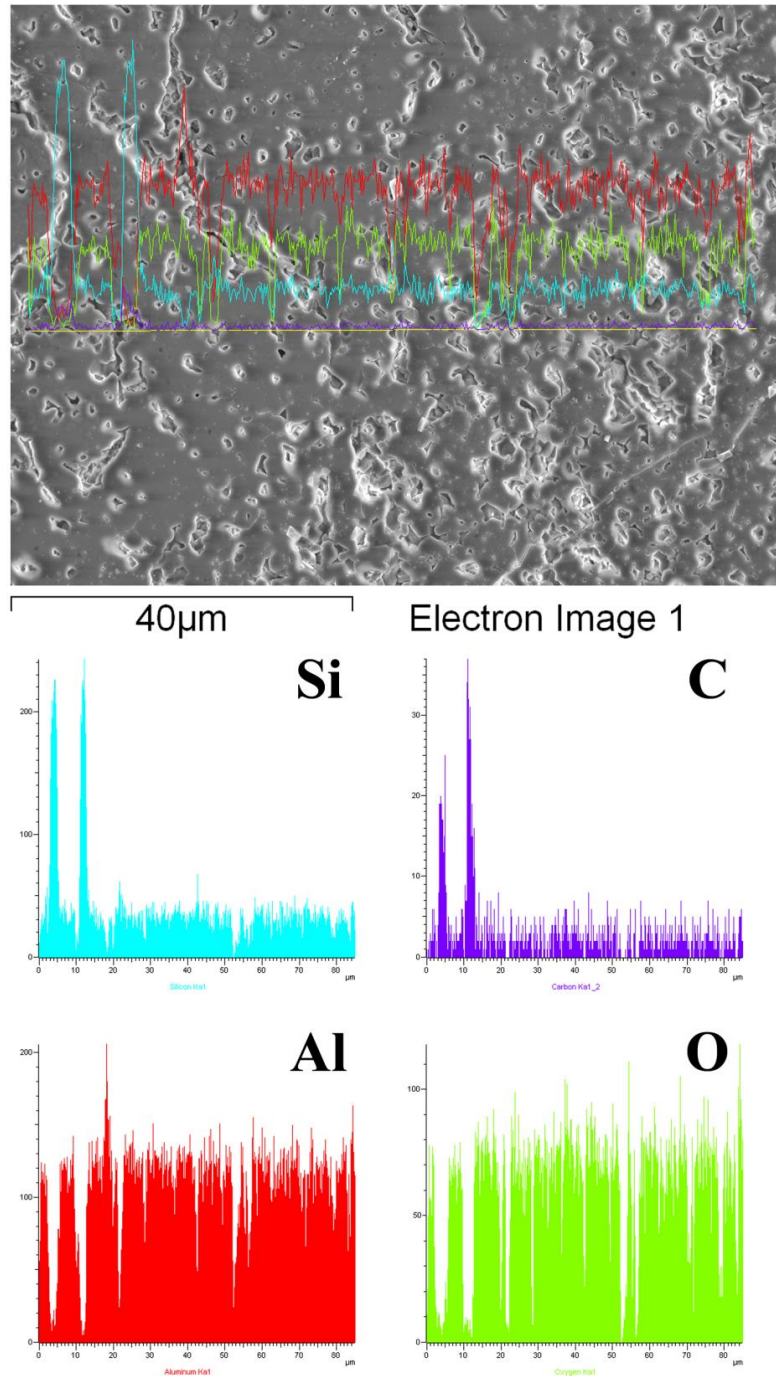
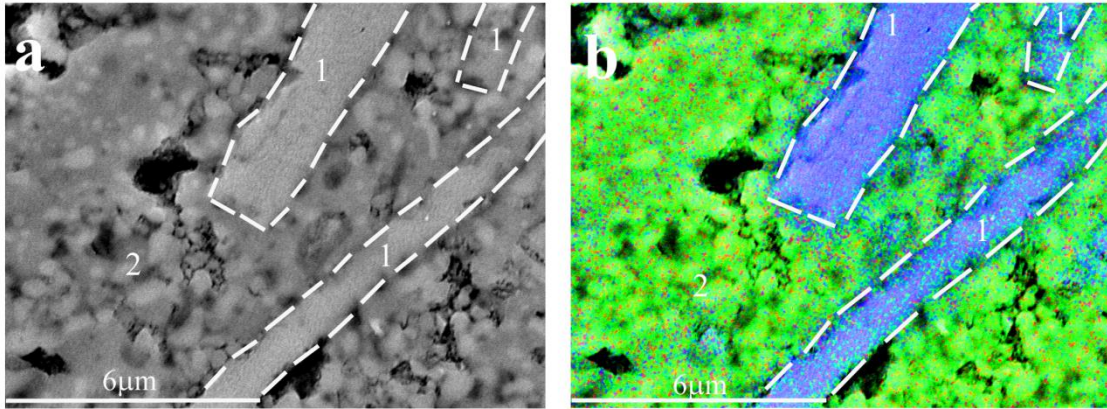


Figure 4-13. EDX line scan at the interface between  $\text{Al}_2\text{O}_3\text{-SiC}_w$  mixture and mullite (different area from Figure 4-12). a. EDX line scan results shown in the electron image of the scanned area; EDX spectra of Si, C, Al, and O are shown below figure a, respectively.



**Figure 4-14. a, Back scattered electron image. b, EDX mapping of silicon carbide whiskers in sintered pellet. Areas 1 are corresponding to SiC whiskers, and areas 2 are corresponding to alumina.**

On the other hand, SiC whiskers originally in the white area of the pellet were oxidized during sintering by air, and the final product of oxidization is mullite according to XRD results, since mullite has Si in its formula. The chemical reaction for the formation of mullite in this work is:  $2\text{SiC} + 3\text{Al}_2\text{O}_3 + 4\text{O}_2 = \text{Al}_6\text{Si}_2\text{O}_{13} + 2\text{CO}_2$ . The original weight ratio of  $\text{Al}_2\text{O}_3$  and SiC in the green pellet is  $\text{Al}_2\text{O}_3/\text{SiC}=4$ , which is equivalent to  $\text{Al}_2\text{O}_3/\text{SiC}=1.56$  by mole. This value reasonably matches the mole ratio of  $\text{Al}_2\text{O}_3$  and SiC in the chemical reaction formula ( $\text{Al}_2\text{O}_3/\text{SiC}=3/2=1.5$ ). Although the amount of alumina is a little bit more than required by the chemical reaction, it does not impede the formation of mullite because excess alumina is present. In summary, the discussion above gives us a proper explanation for the formation of mullite in the pellet.

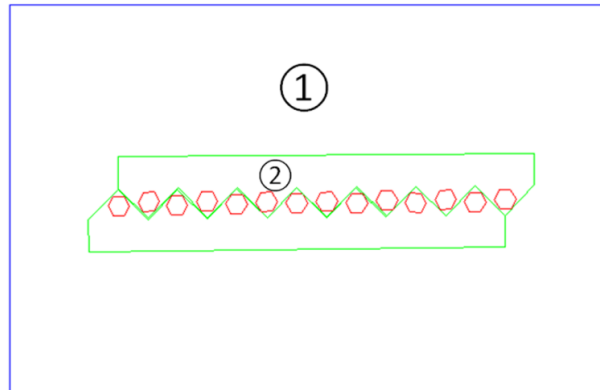
During sintering, the oxidization reaction of  $\text{SiC}_w$  will take place from the outside layer of the pellet, since the outside "shell" surrounding the pellet has the largest contact area with oxygen in air. As discussed above, the oxidization of SiC whiskers will induce the formation of mullite because of the existence of alumina in the green body. The mullite will favorably form on the outside layer of the pellet and eventually form a mullite shell as the surface of the sintered pellet due to the availability of oxygen. With the formation of such a dense mullite layer, the diffusion paths for the oxygen to diffuse from atmosphere to the inner layer of the pellet was blocked. Thus, it is the formation of a "mullite shell" which protects the inner silicon carbide whiskers from being oxidized. As a result, a self-regulating sintering technique for SiC was developed at this point.

#### **4.3.2 Sintering of the Aligned $\text{SiC}_w$ by Self-regulating Sintering Technique**

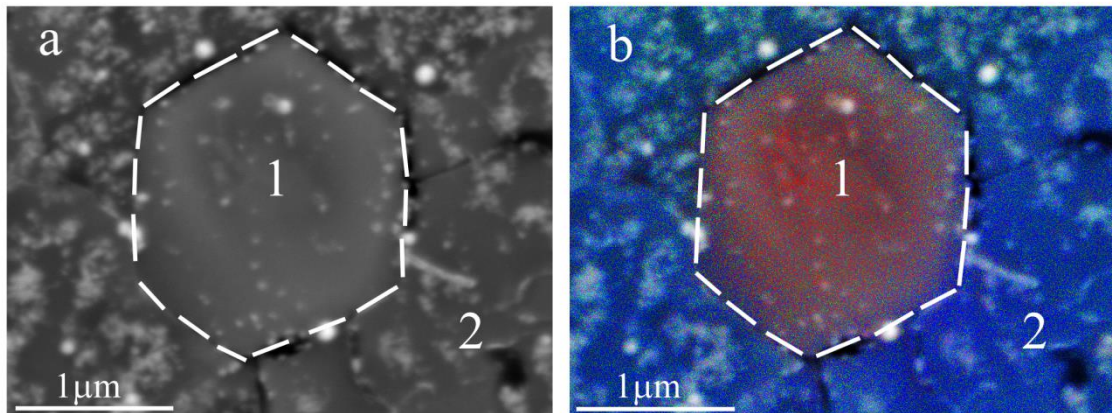
The results in Section 4.3.1 have demonstrated a self-regulating sintering technique for SiC whiskers. For the sintering of alumina tape with aligned SiC whiskers, it may be a good choice to select this sintering technique to protect the aligned whiskers from being oxidized. Figure 4-15 shows us a schematic diagram of a green pellet with a sandwich structure for the sintering of alumina green tape with aligned whiskers. Two circular pieces of alumina tapes ( $\Phi=1/4"$ ) were

laminated together by pressing and then sandwiched by alumina and SiC whiskers mixture ( $\text{Al}_2\text{O}_3/\text{SiC}=4$  by weight, the same weight ratio as the alumina-SiC mixture in Section 4.3.1) to form a green pellet 1/2" in diameter and 5mm in height. After the pellet was sintered, it was cut along the direction which is perpendicular to the alignment direction of SiC whiskers to create a cross section of aligned whiskers for EDX characterization.

The BSE image and EDX elemental mapping results are shown in Figure 4-16. As the pellet was cut along the direction perpendicular to the alignment direction of whiskers, (111) hexagonal planes of the whiskers are exposed after cutting and polishing. EDX mapping results indicate that Si and C signals are concentrated in area 1, while Al and O signals are essentially from area 2. This directly demonstrates that carbon in the aligned SiC whiskers in alumina green tape has not been oxidized during sintering, which indicates the aligned SiC whiskers are protected from being oxidized by using alumina and  $\text{SiC}_w$  mixture as a protective layer for sintering in air. On the other hand, the aligned SiC whiskers can be rigidly and stably embedded into the dense alumina matrix by sintering. Thus, after solving the problems of alignment, transfer, and sintering of SiC whiskers, a rigid ceramic composite with the aligned SiC whiskers embedded in an alumina matrix was successfully developed as the substrate for GaN growth.



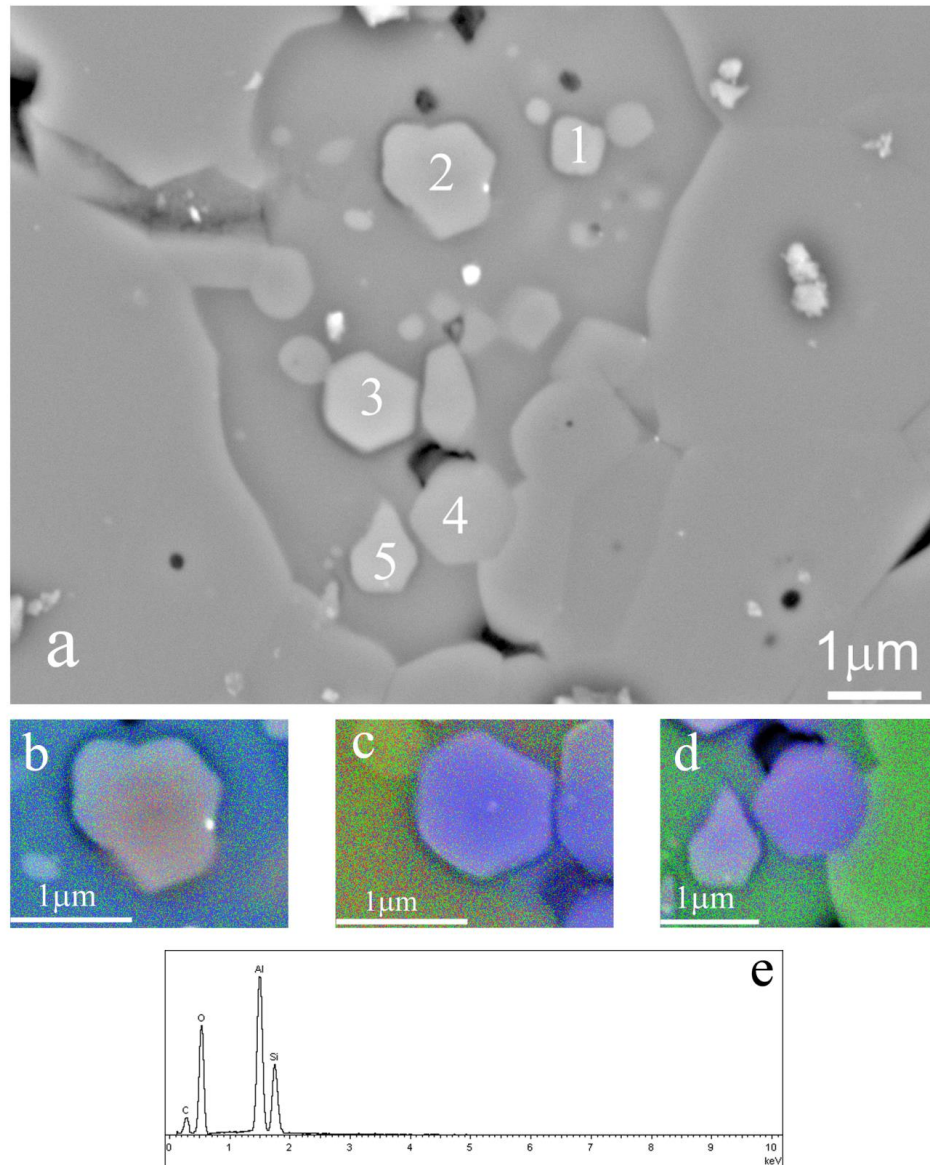
**Figure 4-15. Schematic diagram of "Sandwich" structure of "self-protective" green pellet for aligned SiC<sub>w</sub> sintering. Zone 1: mixture of SiC<sub>w</sub> and Al<sub>2</sub>O<sub>3</sub> (weight ratio Al<sub>2</sub>O<sub>3</sub>/SiC<sub>w</sub>=4); Zone 2: Alumina green tape with aligned SiC<sub>w</sub>. In order to show the details of the alumina tape, it is not drawn to scale.**



**Figure 4-16. a, BSE image of sintered alumina tape cross section; b, EDX mapping of the cross section of the sintered tape. Areas 1 are corresponding to the cross section of SiC whiskers, and areas 2 are corresponding to alumina.**

## 4.4 Study of GaN Thin Film Growth on SiC whiskers

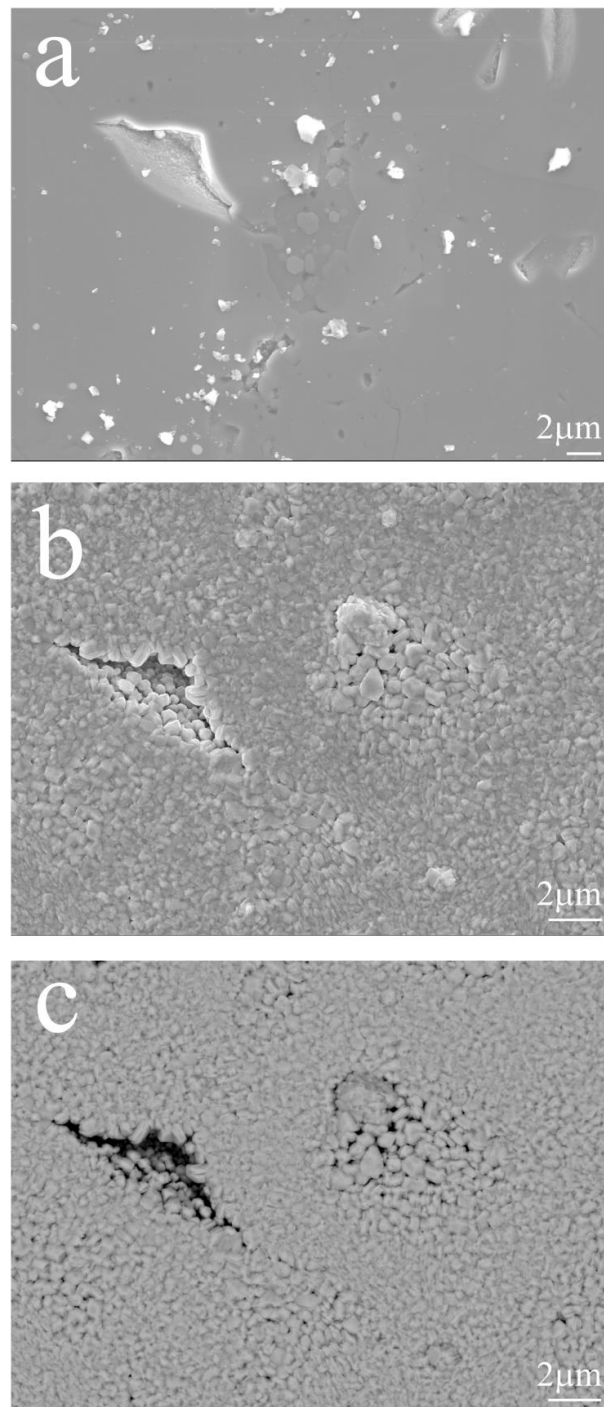
As mentioned in Chapter 3, GaN was deposited on ceramic substrate by magnetron sputtering. Before growth, the ceramic substrate used for this growth was characterized by EDX in the SEM for the determination of location of the SiC whiskers. This is an important step before growth, as once GaN is deposited on the substrate, it may become extremely difficult to find the whiskers underneath. Five whiskers (demonstrated by EDX mapping or point analysis) are found in the BSE image as shown in Figure 4-17. Whisker #2, #3 & #4 have a hexagonal cross section or a close-hexagonal cross section, so they can be good candidates for the investigation of GaN growth behavior on the (111) plane of 3C-SiC.



**Figure 4-17. BSE image of the cross section of SiC whiskers in alumina matrix and their corresponding EDX images/spectrum, the whiskers are labeled as 1, 2, 3, 4, and 5. a. BSE image; b. EDX mapping of whisker #2; c. EDX mapping of whisker #3; d. EDX mapping of whisker #4; e. EDX spectrum of whisker #1 (note that Al and O signals were also collected in this spectrum since the interaction volume of electron beam in the specimen is larger than whisker #1).**

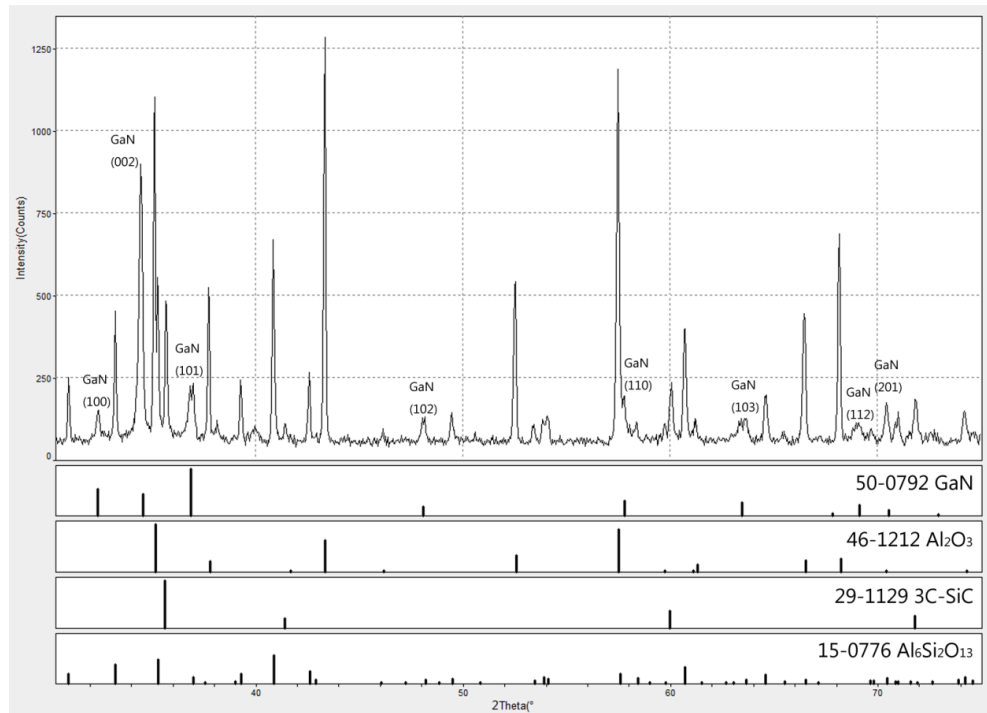
Topography of the ceramic substrate and GaN grown on the ceramic substrate is characterized by SEM as shown in Figure 4-18. From Figure 4-18a, we can find there are a few cavities in the alumina matrix due to the evaporation of residual solvent and plasticizer from tape casting. The contamination on the substrate surface can be washed away before growth by a series of steps as discussed in Section 3.2.4.

Figure 4-18b indicates that GaN growth behavior was related to the surface morphology of the ceramic substrate, which is reasonable because in most cases the orientation of epilayers depend on the substrate orientation and surface roughness. For example, the big cavity close to the upper left corner of Figure 4-18a can lead to a cavity in Figure 4-18b with similar shape. The BSE image in Figure 4-18c suggests that the composition of deposited GaN is homogeneous on the substrate, which indicates that the topography and composition variation cannot change the chemical composition of GaN thin films.



**Figure 4-18. SEM images: a. SEI of ceramic substrate with aligned SiC whiskers; b. SEI of GaN grown on ceramic substrate (same area as figure a); c. BSE image of GaN grown on ceramic substrate.**

The XRD patterns of GaN grown on the ceramic substrate are shown in Figure 4-19. From the overall point of view, XRD shows that GaN thin film is polycrystalline. The (002) reflection of GaN in this specimen is stronger than all other GaN diffraction peaks, which is different from the standard XRD pattern of GaN. This indicates that GaN must have a (002) growth orientation on a certain area of the ceramic substrate. The growth of GaN on (111) oriented SiC whiskers should have a (002) orientation because of the small lattice mismatch between GaN and SiC. On the other hand, the growth direction of GaN on an alumina matrix is random due to the polycrystalline nature of alumina. Thus, it is the combination of (111) orientation of SiC whiskers and the polycrystalline alumina matrix that determines the overall growth orientation of GaN as shown in the XRD pattern.



**Figure 4-19. XRD patterns of GaN thin films grown on ceramic substrate with (111)-oriented SiC whiskers.**

Furthermore, as the SiC whisker is tiny compared with the size of the bulk ceramic substrate, XRD and SEM cannot characterize the GaN thin film grown on an individual SiC whisker by a routine method. Thus, a specific specimen preparation method needs to be developed for the characterization of GaN growth behavior on individual SiC whiskers in the future to demonstrate the assumption proposed in the previous paragraph. A prospective method is to use a Focused Ion Beam to pick up a flake of GaN grown on an individual SiC whisker and another flake of GaN grown on the alumina matrix respectively as shown in Figure 4-20. A detailed investigation can be conducted on the

comparison between GaN growth behavior on the SiC whisker and on the alumina matrix in TEM.

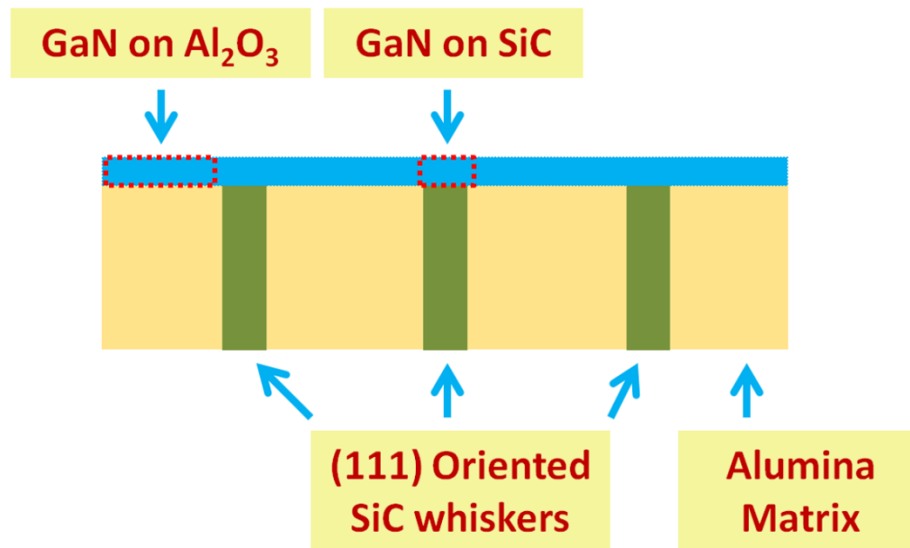


Figure 4-20. Schematic drawing of GaN thin film growth on (111) oriented SiC whiskers embedded in alumina matrix.

## 5 Results and Discussion: Magnetron Sputtering

### Growth of GaN Thin Films

As mentioned in Section 4.4, a specific specimen preparation method needs to be developed for the characterization of GaN growth behavior on aligned (111)-oriented SiC whiskers. Since SiC whiskers are tiny and bulk 3C-SiC single crystal wafers are not commercially available, it is quite helpful to investigate the GaN sputtering growth behavior on bulk (0001)-oriented 6H-SiC wafers, as the (0001) plane of 6H-SiC has the same atomic arrangement as the (111) plane of 3C-SiC and has a very close lattice constant value to the (111) plane of 3C-SiC (the distance between neighboring silicon or carbon atoms is approximately 3.08 Å, in specific, it is 0.30832 nm for 3C-SiC and 0.30806 nm for 6H-SiC). The growth behavior of GaN on (0001)-oriented 6H-SiC can be directly considered as the growth behavior of GaN on (111) planes of 3C-SiC. Thus, the investigation of GaN growth behavior on (0001)-oriented 6H-SiC wafers can be considered as a prototype for the investigation of GaN growth behavior on (111) planes of 3C-SiC whiskers.

## 5.1 Control of Contamination in the Thin Film

### 5.1.1 Detection of Contamination

The XRD patterns of three GaN thin films (#32, #33, and #34) grown on 6H-SiC are shown in Figure 5-1. All of the three specimens were grown under the same growth conditions but the XRD results are irregular. None of them show a (0002) peak of GaN, and both #32 and #33 show a reflection from (11 $\bar{2}$ 0) planes, and #34 shows a weak reflection from (10 $\bar{1}$ 1) planes.

The irregular XRD patterns suggested that there might be some fundamental issues in the deposition chamber. For example, the growth procedure could always be contaminated by some unknown contaminations. EDX was employed to analyze chemical composition of GaN-#34 and the results are shown in Figure 5-2. The spectrum shows four peaks which correspond to carbon, nitrogen, oxygen and gallium respectively. Carbon was intentionally coated on the specimen for electrical conduction in SEM. However, the oxygen peak is significant and it is a contamination in the specimen.

Oxygen is likely to contaminate the thin film due to leaks. To find the source of oxygen, RGA was employed to analyze the composition of residual gas in the sputtering chamber at the time when Ar was introduced into the chamber, and at the time when N<sub>2</sub> was introduced into the chamber. The spectra are shown in

Figure 5-3. From Figure 5-3a we can see that when Ar was introduced,  $N_2$  and  $O_2$  were also leaked into the chamber. This also happened when  $N_2$  was introduced, as  $O_2$  was leaked into the chamber as shown in Figure 5-3b.

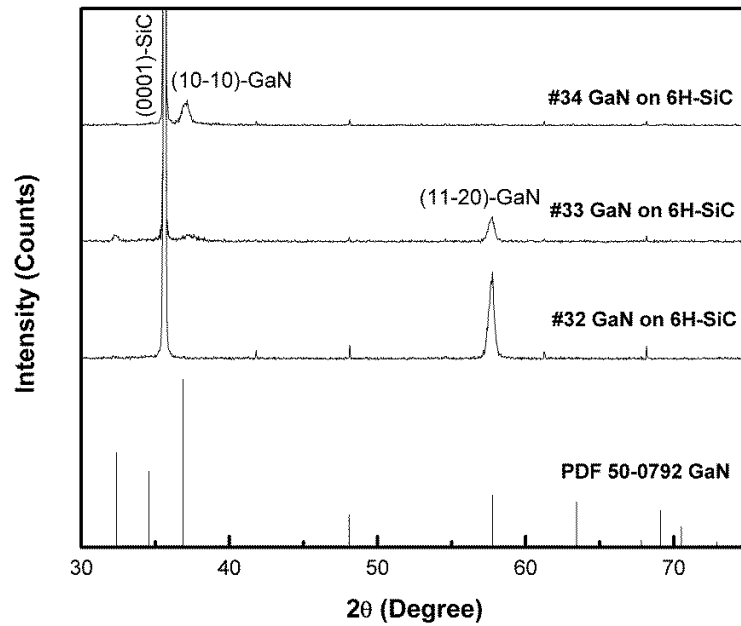
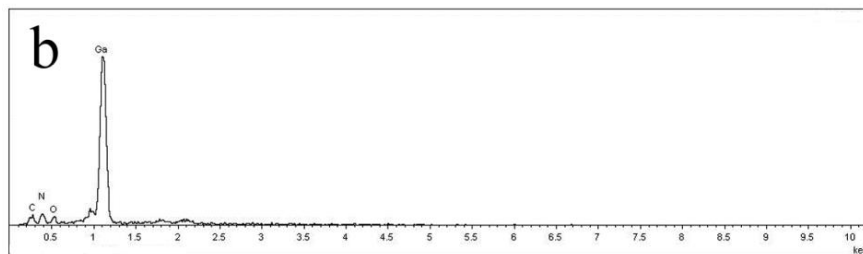
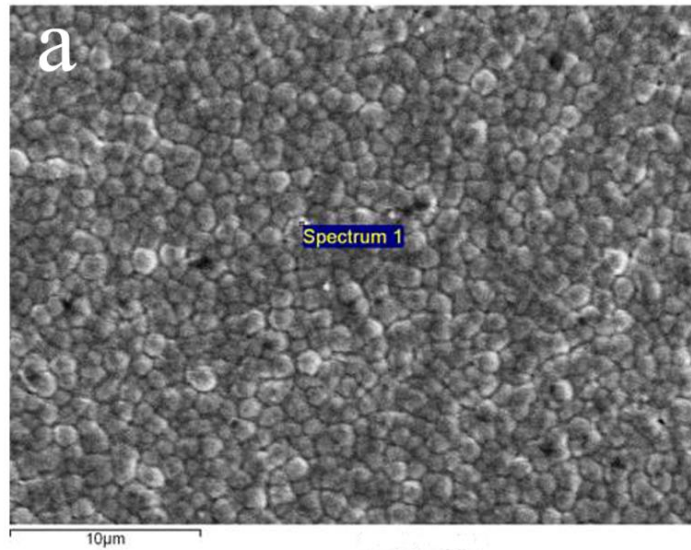
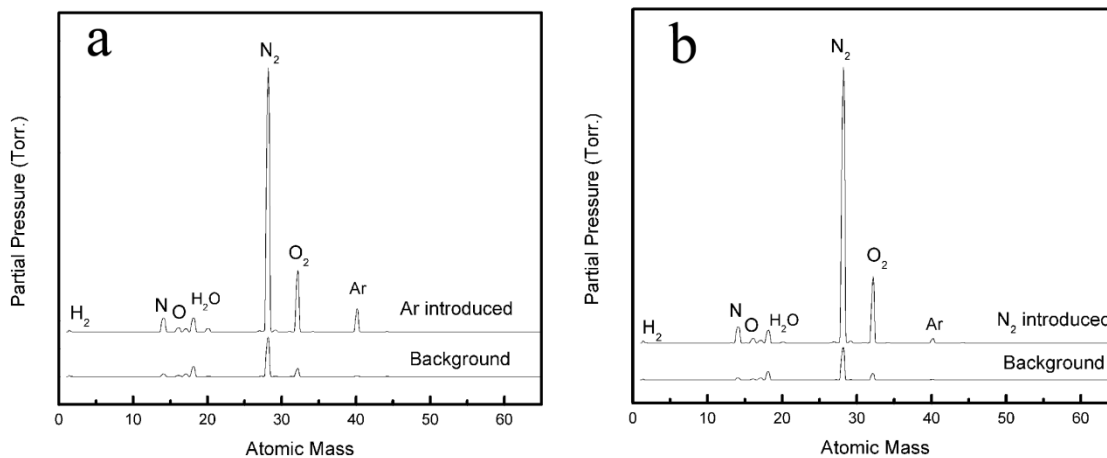


Figure 5-1. XRD patterns of GaN (#32, #33, and #34) grown on (0001)-oriented 6H-SiC substrates.



**Figure 5-2. a, SEM image of GaN-#34 grown on (0001)-oriented 6H-SiC substrate; b, EDX point analysis spectrum of "spectrum 1" in the SEM image.**



**Figure 5-3. Residual gas mass spectra. a, gas mass spectrum at background pressure versus gas mass spectrum at the time when Ar was introduced; b, gas mass spectrum at background pressure versus gas mass spectrum at the time when N<sub>2</sub> was introduced.**

On the other hand, EDX was also conducted on GaN-#42, which was grown on (111)-oriented Si substrate at a time later than GaN-#34. The results shown in Figure 5-4 clearly indicate that copper was incorporated into the thin film. As mentioned in Section 3.2.2, a copper cup was used to carry the gallium target as gallium is a low-melting point material. The Cu-Ga binary phase diagram as shown in Figure 5-5 indicates that several intermetallic compounds exist in the Cu-Ga binary system at room temperature. EDX was conducted directly on the gallium target and the results as shown in Figure 5-6 clearly demonstrate that copper was incorporated into gallium. Note that copper did not contaminate the thin film at an early stage (at the growth time of GaN-#32, #33, and #34) since it took some time for the copper to diffuse into gallium.



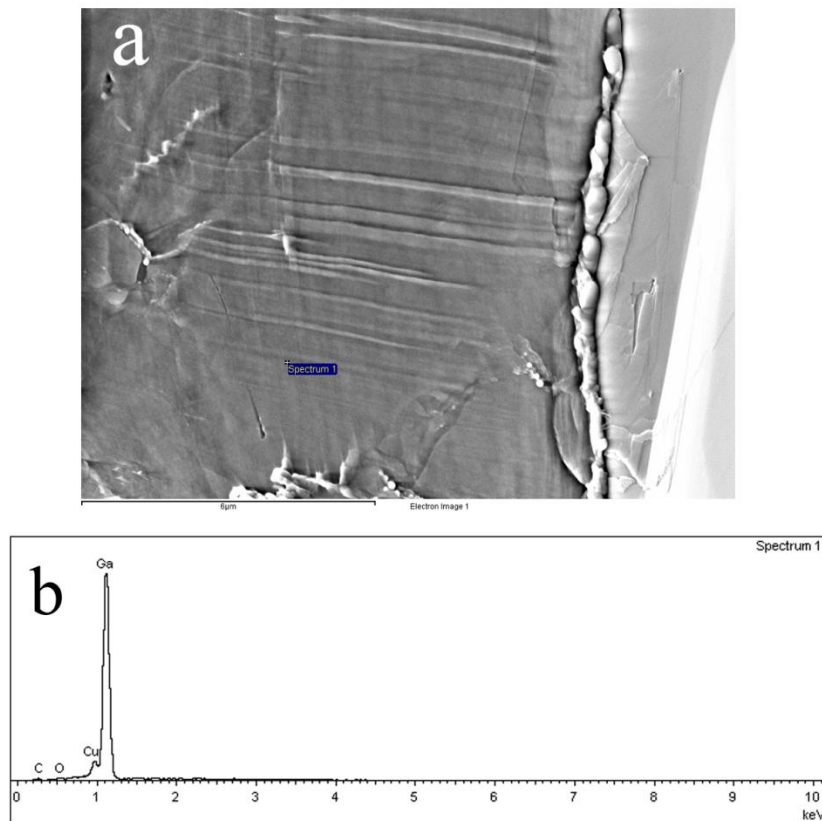


Figure 5-6. a, SEM image of Ga target carried by copper cup; b, EDX point analysis spectrum of "spectrum 1" in the SEM image.

### 5.1.2 Removal of Contamination

Polyethylene tubing was initially being used to introduce Ar and N<sub>2</sub> into the chamber, Due to its oxygen and water permeability polyethylene tubing was identified as the reason for the oxygen contamination. After the leakage was detected, all of the polyethylene tubing was replaced by smooth bore Polytetrafluoroethylene (PTFE) core 304 stainless steel hose (Swagelok) as

shown in Figure 5-7. PTFE is a material which is compatible with an ultra high vacuum environment [186]. The residual gas composition spectrum in Figure 5-8 shows that the oxygen peak is much weaker than the Ar peak when Ar was introduced into the chamber. Note that when polyethylene tubing was in use, the oxygen peak in the gas mass spectrum is stronger than the argon peak when argon was introduced as shown in Figure 5-3.



Figure 5-7. Smooth bore PTFE core stainless steel hose [187].

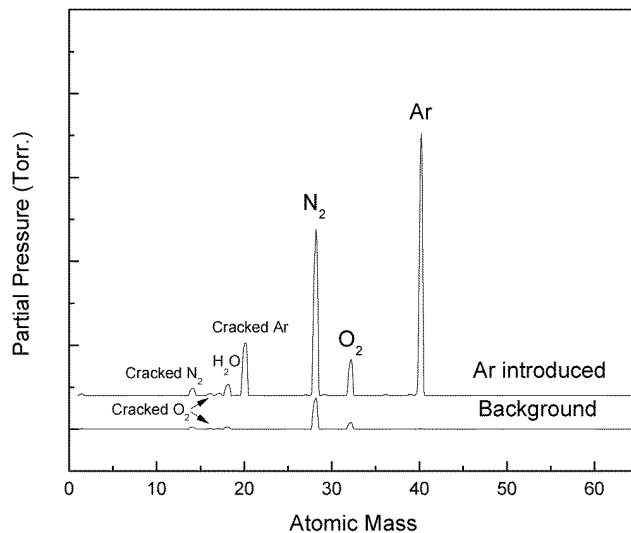
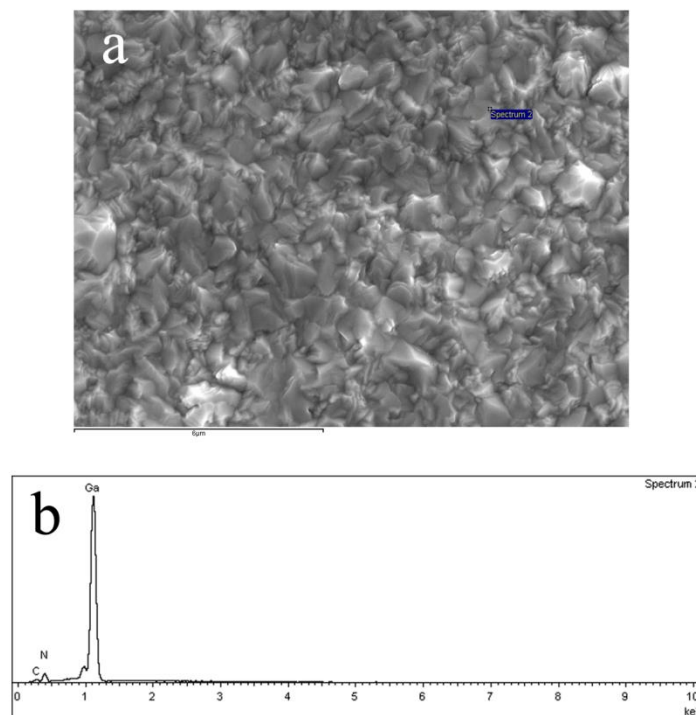


Figure 5-8. Gas mass spectrum at background pressure versus gas mass spectrum at the time when Ar was introduced after polyethylene tubing was replaced by smooth bore PTFE core hose.

To address the copper contamination issue, the copper cup was replaced by a graphite cup to carry the gallium target for sputtering. Graphite is compatible with a high vacuum environment, and it is immiscible with gallium. After the polyethylene tubing and the copper cup were both replaced, a GaN thin film (GaN-#57) growth was conducted on (111)-oriented Si substrate for the investigation of contaminations in GaN thin film. The EDX spectrum in Figure 5-9 shows there is no oxygen or copper peak any more. XRD pattern in Figure 5-10 shows the GaN thin film is (0002)-oriented.



**Figure 5-9. SEM image of GaN-#57 grown on (111)-oriented Si substrate after polyethylene tubing and copper cup were replaced; b, EDX point analysis spectrum of "spectrum 2" in the SEM image. Note that carbon peak in the spectrum is from the carbon coating for**

electrical conduction in SEM. No elements other than C, N, and Ga can be detected from the specimen.

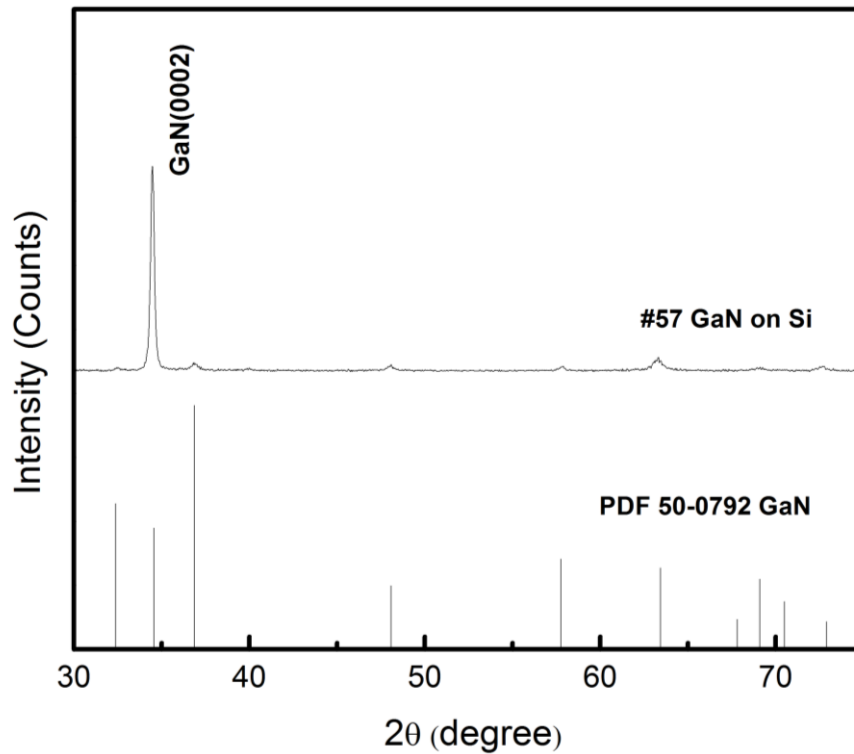


Figure 5-10. XRD pattern of GaN-#57 grown on (111)-oriented Si substrate after polyethylene tubing and copper cup were replaced.

## 5.2 Substrate Dependence

As the contamination in the thin film was eliminated, we refocused the GaN growth on the (0001)-oriented 6H-SiC substrate. GaN-#58 was grown on the 6H-SiC substrate with the same growth conditions and procedure as GaN-#57. XRD

patterns in Figure 5-11 show us GaN-#58 has a much stronger (0002) peak than GaN-#57. To be quantitative, the (0002) peak of GaN-#58 is 32 times as high as the (0002) peak of GaN-#57. In addition, GaN-#58 has a reflection peak from (0004) planes in the XRD pattern, which is a sign for a high degree of (0002) orientation.

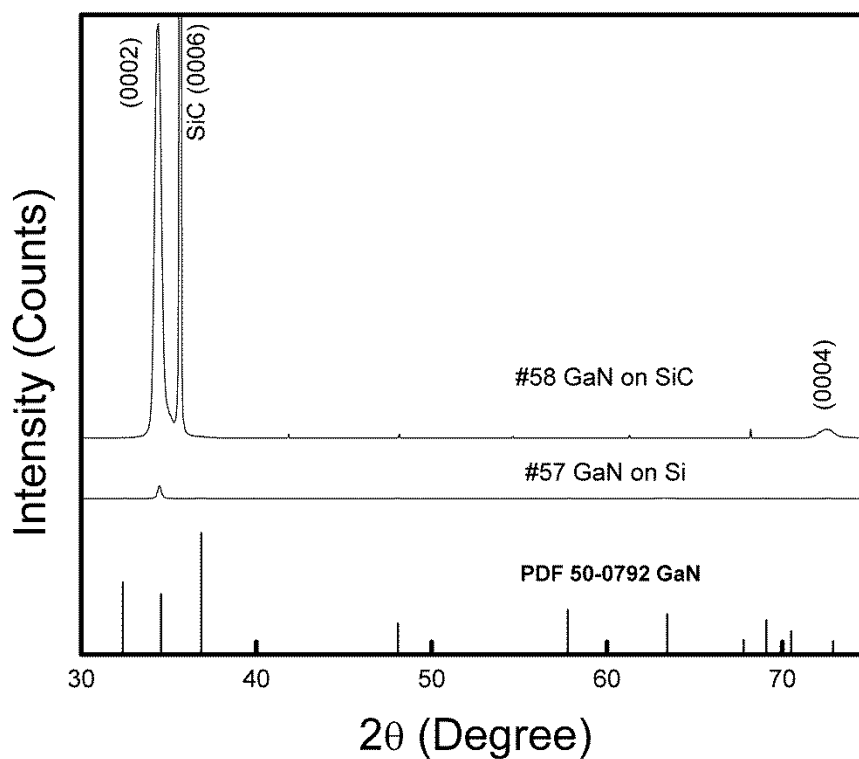
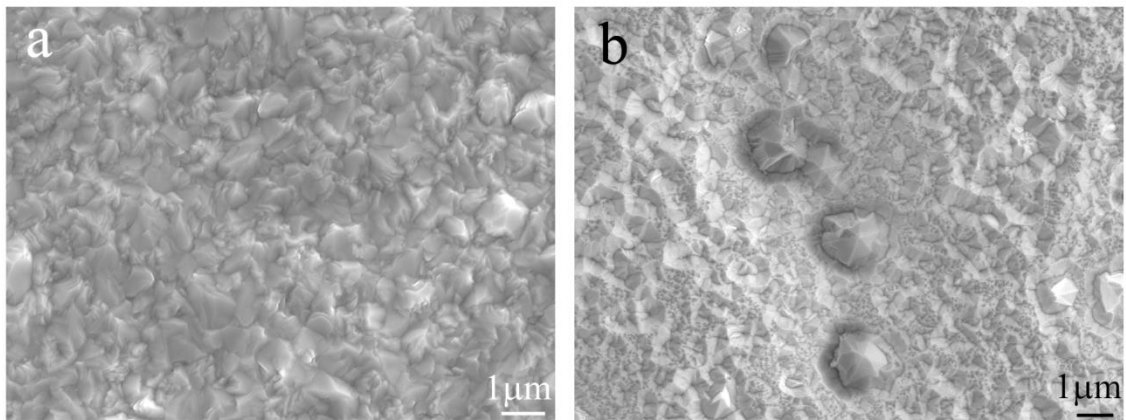


Figure 5-11. XRD patterns of GaN-#57 grown on Si substrate and GaN-#58 grown on SiC substrate.

The topography of GaN-#57 and #58 are shown in Figure 5-12. From the SEM images, we can see that GaN-#57 has a different surface morphology from GaN-#58. The appearance of the grains in GaN-#57 is random, and there is no preferred feature in topography. The grains in GaN-#58 have a pyramid appearance at the surface, although several grains have a larger grain size than others. The similarity of the grain appearance in GaN-#58 is a sign of a higher degree of orientation of GaN thin film on SiC substrate than that on a Si substrate.



**Figure 5-12. SEM images of GaN-#57 grown on Si substrate (a) and GaN-#58 grown on SiC substrate (b).**

As mentioned in Section 2.2.4.3, Si has a large mismatch in terms of lattice constant and thermal expansion coefficient with GaN. It is a challenge to grow high quality GaN on Si although it is quite attractive due to its low cost and compatibility with circuitry. According to the XRD patterns and the thin film topography in this work, we also demonstrated that Si cannot provide a growth

template for GaN which is as good as 6H-SiC. The focus of GaN thin film growth in this thesis will be using 6H-SiC substrates.

## **5.3 GaN Thin Film Growth on SiC Substrate in Ar and N<sub>2</sub> Atmosphere**

In order to optimize GaN thin film quality by sputtering, an elevated temperature at approximately 700°C is essential for sufficient kinetic energy of adatoms [7]. Here we have grown two samples at 700°C in Ar and N<sub>2</sub> with different sputtering times. The growth time for GaN-#58 is 40 mins, while it is 20 mins for GaN-#61. The nominal thin film thicknesses for GaN-#58 and GaN-#61 are 3 μm and 1.5 μm, respectively.

### **5.3.1 XRD Studies of GaN Thin Films**

The XRD patterns of these two samples are shown in Figure 5-13. The very strong peak at 35.64° is the (0006) reflection from the 6H-SiC single crystal substrate. The GaN (0002) reflection at 34.56° is broader and weaker from GaN-#58 compared to the one from GaN-#61. Even with a reduced film thickness, GaN-#61 has a strong (0002) peak of 56723 counts/sec, 8 times as high as the one attributed to GaN-#58 (6860 counts/sec). In addition, a much stronger (0004)

peak at  $72.84^\circ$  from GaN-#61 than that from GaN-#58 is detected. All these facts suggest that the crystalline quality of GaN-#61 is higher than that of GaN-#58.

On the other hand, XRRC characterization was conducted on GaN-#61 and the result is shown in Figure 5-14. The FWHM of the rocking curve is 50 arcmin, which indicates the crystalline quality of GaN-#61 is high among GaN thin films grown by sputtering.

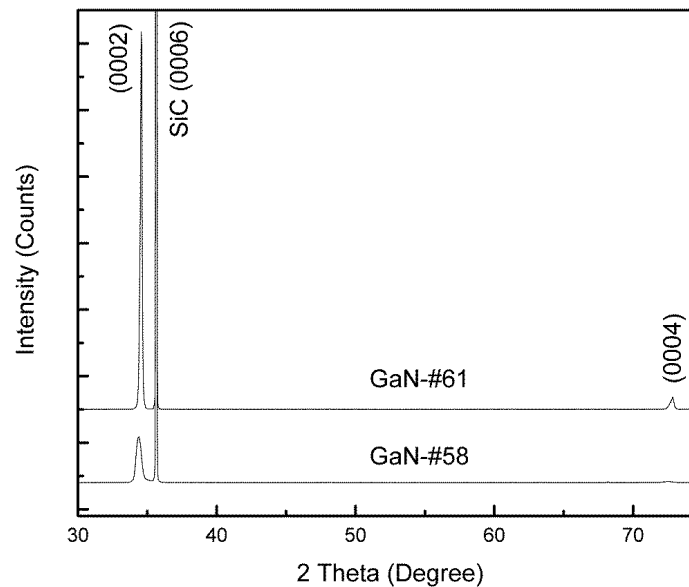


**Figure 5-13. XRD patterns of GaN thin films grown on 6H-SiC substrates with different thickness.**

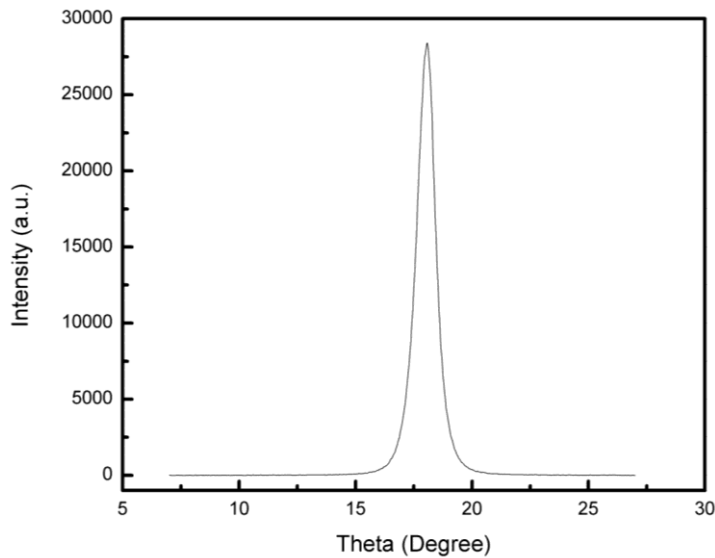


Figure 5-14. XRRC of GaN-#61. FWHM of the peak is 50 arcmin.

### 5.3.2 Surface Morphology of GaN Thin Films

The SEM micrographs of GaN-#58 and GaN-#61 are shown in Figure 5-15 and the corresponding grain size distributions are illustrated in Figure 5-16. With the existence of three hexagonal hillock-grains whose diameters are larger than 2  $\mu\text{m}$  in Figure 5-15a, GaN-#58 has a wider grain size distribution than that of GaN-#61. From Figure 5-16, we can also find that the average grain size of GaN-#61 is smaller than that of GaN-#58.

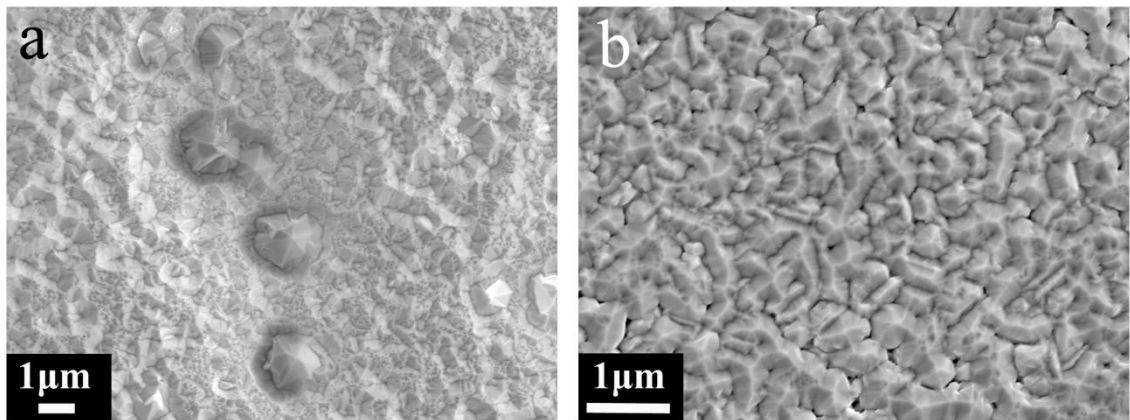
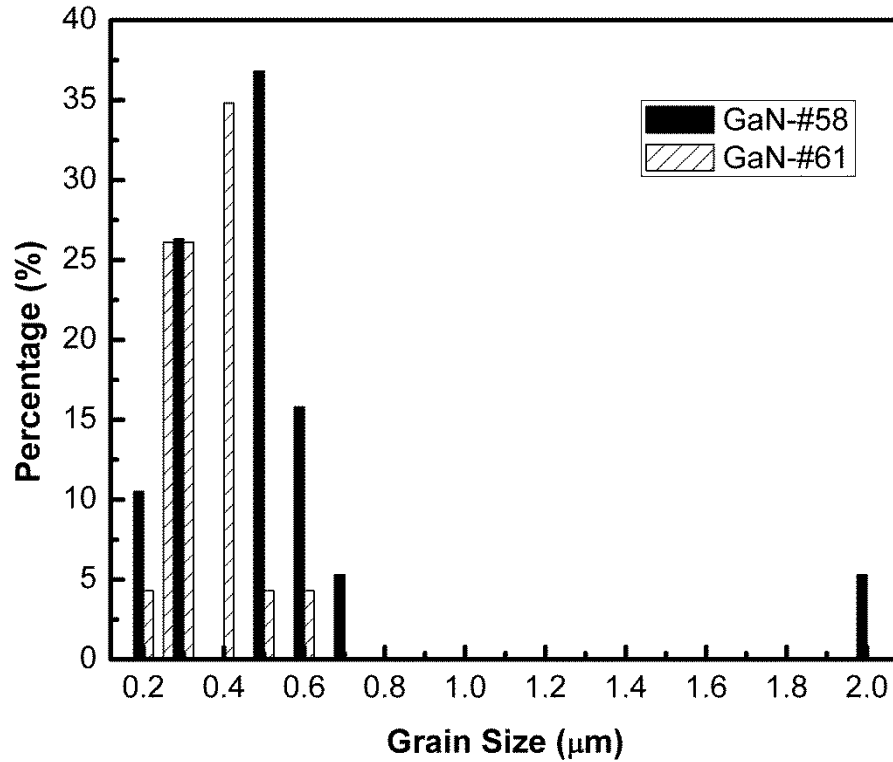


Figure 5-15. SEM micrographs of (a) GaN-#58 and (b) GaN-#61.



**Figure 5-16. Grain size distribution of GaN-#58 and GaN-#61 according to SEM micrographs.**

Since both GaN-#58 and GaN-#61 were grown under the same conditions except the sputtering time, it is the thickness effect that induces the crystalline quality and surface morphology differences between these two specimens. The main surface feature of GaN-#58 is the existence of hexagonal hillocks as shown in Figure 5-15a. Morkoç [188] proposed that the formation of hexagonal hillocks are induced by the surplus Ga during the deposition process as shown in Figure 5-17. If the substrate temperature is as high as 800°C, thermal desorption of surplus Ga would take place. We can speculate that since the growth temperature in this

work is 700°C the Ga atoms that do not participate in the formation of GaN prefer to migrate to surface sites with minimum surface energy. After this, Ga clusters are formed on the surface and they can also serve as preferred nucleation sites. The accumulated Ga atoms in each cluster can induce a locally accelerated GaN growth and thus form huge hexagonal hillocks on the thin film surface.

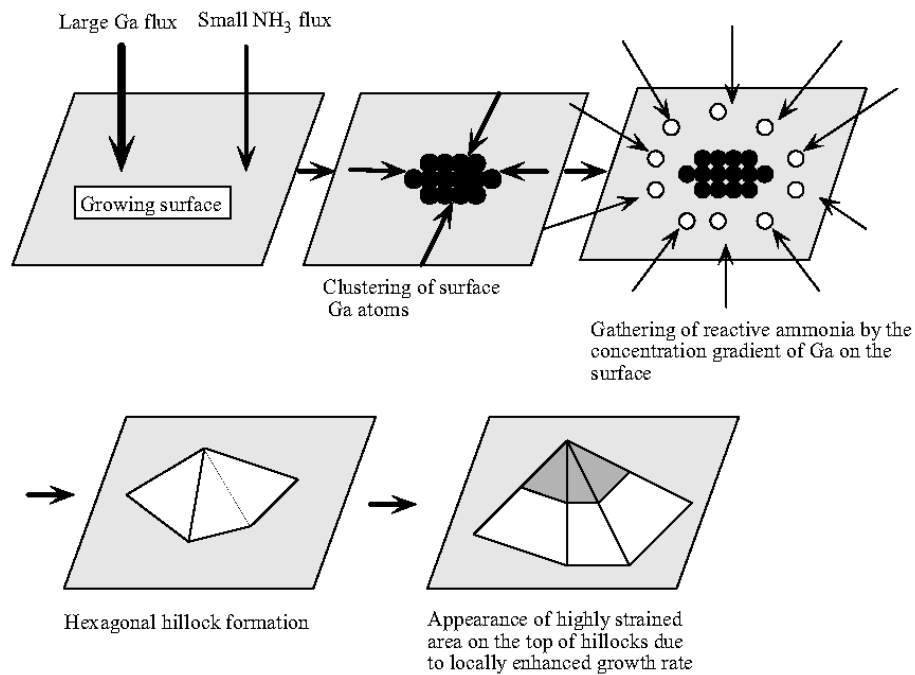


**Figure 5-17. A proposed pathway to hillock formation in the growth of GaN [189].**

At the beginning stage of GaN thin film growth on SiC substrates, the dimension of surplus Ga clusters is relatively small as the SiC substrate surface is smooth (roughness < 0.5nm), which suggests that it is not easy for Ga atoms to find a terrace to stay. However, as time goes by, GaN thin film starts to grow on the SiC

surface and the surface roughness increases. At this stage, the surplus Ga atoms easily to find a terrace with minimum surface energy to accumulate. On the other hand, if the growth time is long, adjacent small surplus Ga clusters can form a big Ga cluster by Ostwald ripening. In Figure 5-15a, as an evidence of Ostwald ripening, we can always find a dimple around a hexagonal hillock grain in GaN-#58, which indicates the formation of a hillock grain accompanied by the consumption of adjacent materials. The growth time of GaN-#58 is twice as long as the growth time of GaN-#61. We suggest that at the late thin film growth stage of GaN-#58, Ostwald ripening of surplus Ga atoms starts to take place as growth time is long at this stage. As the dimension of Ga clusters is large, it is reasonable to argue that Ga atoms in the inner layers of clusters cannot react with  $N_2$  sufficiently and thus the GaN thin films grown in this way can be nonstoichiometric. This also happened in the MBE growth of GaN, since Ga droplets can be observed in the SEM micrograph of GaN thin film grown under Ga-rich growth condition [190]. In summary, the nonstoichiometry and large surface roughness of GaN-#58 result in weaker (0002) reflections in the XRD pattern than from GaN-#61.

### 5.3.3 2D-XRD Pole Figures of GaN Thin Films

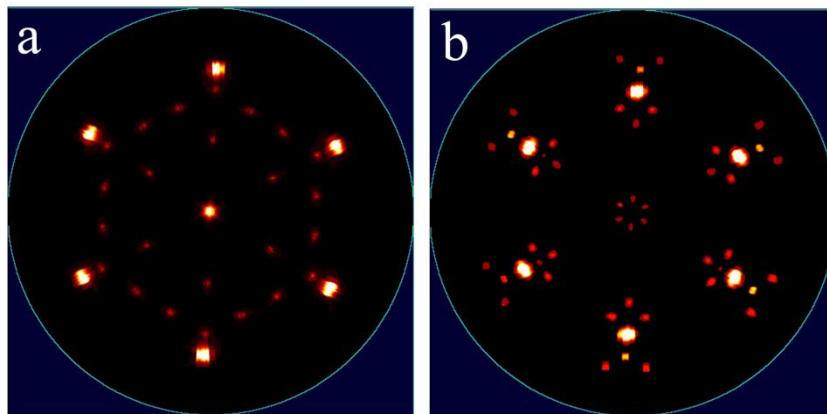


**Figure 5-18. Pole figures of GaN-#61 obtained by 2D-XRD. a, (0002) pole figure; b,  $\{10\bar{1}1\}$  pole figure.**

As shown in Figure 5-18, (0002) and  $\{10\bar{1}1\}$  pole figures GaN-#61 were generated using the reflections in the  $2\theta$  range of 29-59 degrees ( $39.4^\circ$ - $41.4^\circ$  for (0002) pole figure and  $42.1^\circ$ - $44.1^\circ$  for  $\{10\bar{1}1\}$  pole figure). In Figure 5-18a, the central bright pole is from the (0001) oriented wurtzite GaN and six bright poles with six fold symmetry correspond to the  $\{3\bar{3}02\}$  oriented wurtzite GaN,  $\{511\}$  oriented zinc-blende GaN,  $\{111\}$  oriented zinc-blende GaN and 6H-SiC substrate due to the fact that the  $2\theta$  range of the present (0002) pole figures covers the (0002) reflections from wurtzite GaN,  $\{111\}$  reflections from zinc-blende GaN, and  $\{10\bar{1}2\}$  reflections from 6H-SiC substrate. (See Figure 5-26a for the

simulated (0002) pole figure). Although the poles from  $\{111\}$  oriented zinc-blende GaN overlap with the others, we assume the existence of  $\{111\}$  oriented zinc-blende GaN because of the small lattice mismatch between the  $\{111\}$  crystallographic plane from zinc-blende GaN and the (0001) crystallographic plane from 6H-SiC substrates. The six weak poles next to the six bright poles with six-fold symmetry are from the 6H-SiC substrate. The remaining weak poles in the (0002) pole figures are attributed to  $\{511\}$ -oriented zinc-blende GaN. In Figure 5-18b, the six brightest poles with six fold symmetry correspond to (0001) orientated wurtzite GaN and 6H-SiC substrate. The following method can be used to find the reflections from 6H-SiC substrate: if we draw a diameter from the center of the circle through each  $\{10\bar{1}1\}$  pole, the diameters will pass through one small spot next to each of six  $\{10\bar{1}1\}$  poles, which sit just between each  $\{10\bar{1}1\}$  pole and the edge of circle. These poles are also from the 6H-SiC substrate. The remaining poles in Figure 5-18b, can be attributed to the  $\{3\bar{3}02\}$  oriented wurtzite GaN. The orientations of GaN-#61 are summarized in Table 5-1 according to the simulated patterns of pole figures as shown in Figure 5-26.

**Table 5-1. Summary of GaN-#61 thin film orientation on 6H-SiC substrate. (w-GaN: wurtzite GaN; z-GaN: zinc-blende GaN)**

Sample	Orientation-1	Orientation-2	Orientation-3	Orientation-4
GaN- #61	$(0001)_{\text{w-GaN}} \parallel (0001)_{\text{SiC}}$ $\langle 11\bar{2}0 \rangle_{\text{w-GaN}} \parallel \langle 11\bar{2}0 \rangle_{\text{SiC}}$	$\{111\}_{\text{z-GaN}} \parallel (0001)_{\text{SiC}}$ $\langle 01\bar{1} \rangle_{\text{z-GaN}} \parallel \langle 11\bar{2}0 \rangle_{\text{SiC}}$	$\{3\bar{3}02\}_{\text{w-GaN}} \parallel (0001)_{\text{SiC}}$ $\langle 11\bar{2}0 \rangle_{\text{w-GaN}} \parallel \langle 11\bar{2}0 \rangle_{\text{SiC}}$	$\{511\}_{\text{z-GaN}} \parallel (0001)_{\text{SiC}}$ $\langle 01\bar{1} \rangle_{\text{z-GaN}} \parallel \langle 11\bar{2}0 \rangle_{\text{SiC}}$

### 5.3.4 GaN/SiC Interfacial Structure and Chemical Composition

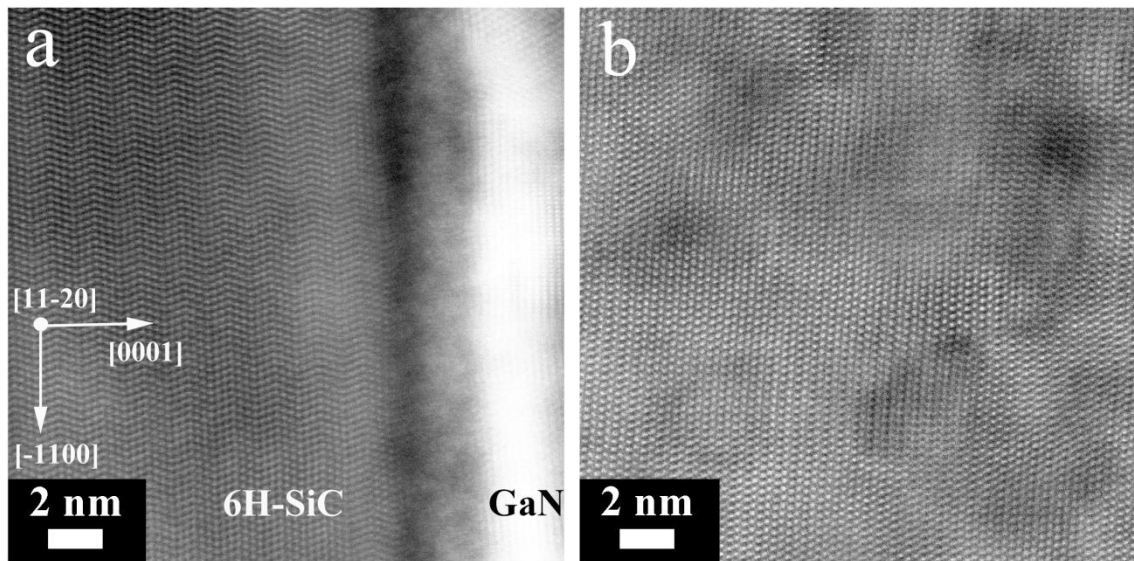


**Figure 5-19. HAADF micrographs of GaN-#58. a, GaN/SiC interface; b, as grown GaN thin film.**

The interfacial structure between GaN and the SiC substrate, reflecting the initial thin film growth stage, was characterized by HAADF imaging in a STEM. As shown in Figure 5-19a, a 3.5 nm thick amorphous layer, confirmed by the diffraction techniques, was recorded as the dark region between the 6H-SiC substrate and the GaN in the HAADF image. In the HAADF images, the amorphous layers have different contrast from crystalline layers due to either the channeling effect from the crystalline materials or the uneven removal of materials by ion milling or both. As shown in Figure 5-19b, GaN was stacked along  $\langle 0001 \rangle$  directions with ABAB stacking order. In order to investigate the elemental distribution across the GaN/SiC interface, chemical analysis was carried out with EELS and the elemental profiles are shown in Figure 5-20. We detect the presence of oxygen in the amorphous layer, and the amount of carbon gradually changes across the amorphous layer. This implies that the amorphous layer is the native oxide layer on the SiC substrate.

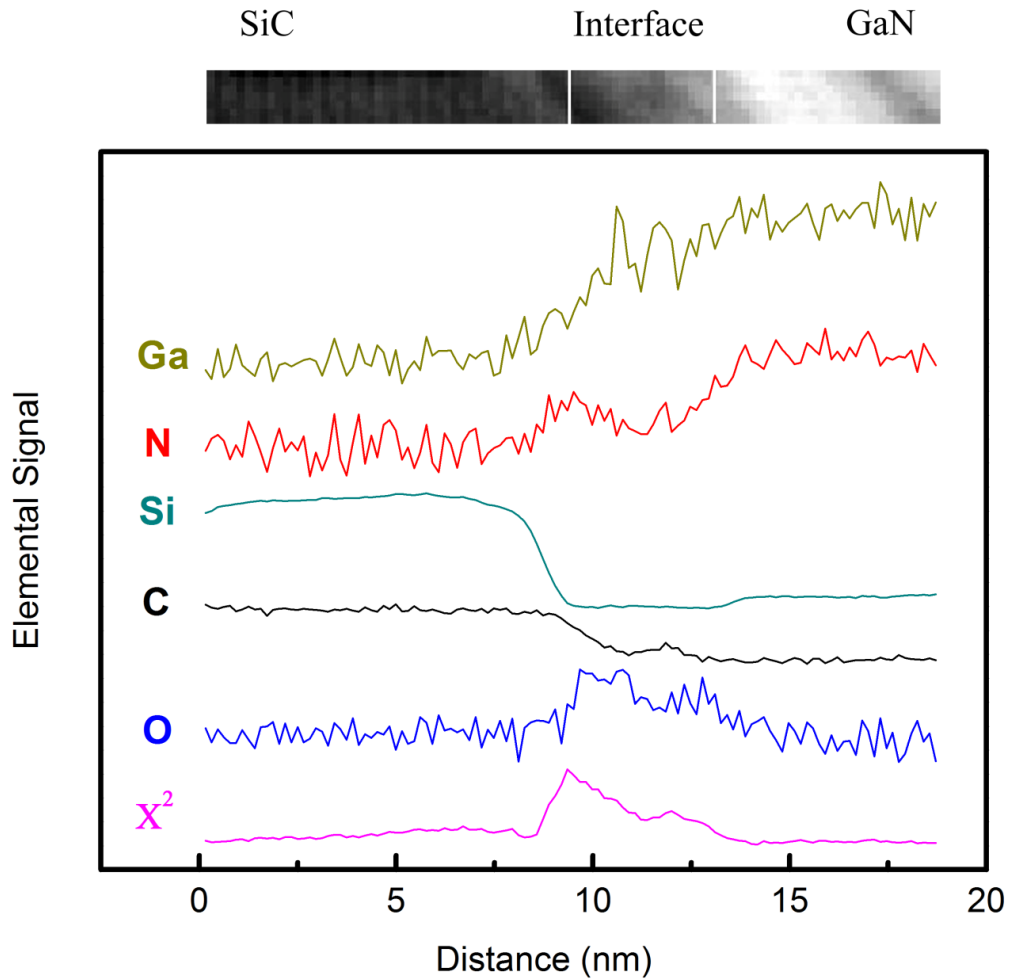


**Figure 5-20. Elemental profiles across GaN/SiC interface of GaN-#58 by EELS and HAADF image of scanned area. Ga  $L_{23}$  edge, N K edge, Si  $L_{23}$  edge, C K edge, and O K edge are used for each profile. Note that because the EELS spectral features of the Si  $L_{23}$  edge and the Ga  $M_{23}$  edge overlap, the Ga  $L_{23}$  edge signal is used instead of the Ga  $M_{23}$  edge signal to draw the Ga profile. The Si profile is obtained by the multiple linear least squares (MLLS) fitting from the overlapped Si  $L_{23}$  edge and Ga  $M_{23}$  edge peak. A chi-squared test was carried out to measure the degree of fitting, and a large difference between observed and expected outcome was found in the interface, which indicates the fitted Si profile in the interface is not accurate.**

The Si profile declines faster than the carbon profile across the GaN/SiC interface as the Si profile is obtained by the multiple linear least squares (MLLS) fitting

from the overlapped Si  $L_{23}$  edge and the Ga  $M_{23}$  edge in the EELS spectra of the interface as shown in Figure 5-21a (the threshold energy of the Si  $L_{23}$  edge is 99 eV, and the threshold energy of the Ga  $M_{23}$  edge is 103 eV, which overlap if Si and Ga coexist in the specimen). MLLS fitting also produces a smooth elemental profile. The Si  $L_{23}$  edge EELS from the SiC substrate and the Ga  $M_{23}$  edge EELS from the GaN thin film are considered as the standard signals to fit the Si profile at the interface. However, as the bonding configuration of Si at the interface is different from that in the bulk SiC, the threshold energy of the Si  $L_{23}$  edge may shift slightly in the high energy direction (the reason will be explained in the next paragraph) as shown in Figure 5-21a. Such a shift cannot be accounted for in the MLLS fitting, and thus the Si profile in the interface does not reflect the real situation.

As a means of obtaining a fingerprint of the chemical environment of elements in a specimen [191], the energy-loss near edge structure (ELNES) corresponds to the promotion of core shell electrons to vacant levels above the Fermi level, the wavefunctions of which are determined by the atomic species and its bonding environment [191, 192]. The Si  $L_{23}$  edge reflects the energy of the 2p core level relative to the vacant levels, which depend on the ionicity of the bond with the ligand atom. This is the underlying reason for the possible chemical shift of the Si  $L_{23}$  edge in different compounds [191, 193, 194]. The threshold energy of the Si  $L_{23}$  edge increases with the increase of electronegativity of the ligand atom due to the effect of charge transfer from silicon to the ligand atoms [191]. We can clearly

find the chemical shift of the Si L<sub>23</sub> edge in the GaN/SiC interface by approximately 3 eV as shown in Figure 5-21a, as oxygen in the native oxide layer of SiC in the GaN/SiC interface has a larger electronegativity than carbon. This chemical shift of this Si L<sub>23</sub> edge agrees well with the value reported in the literature [191].

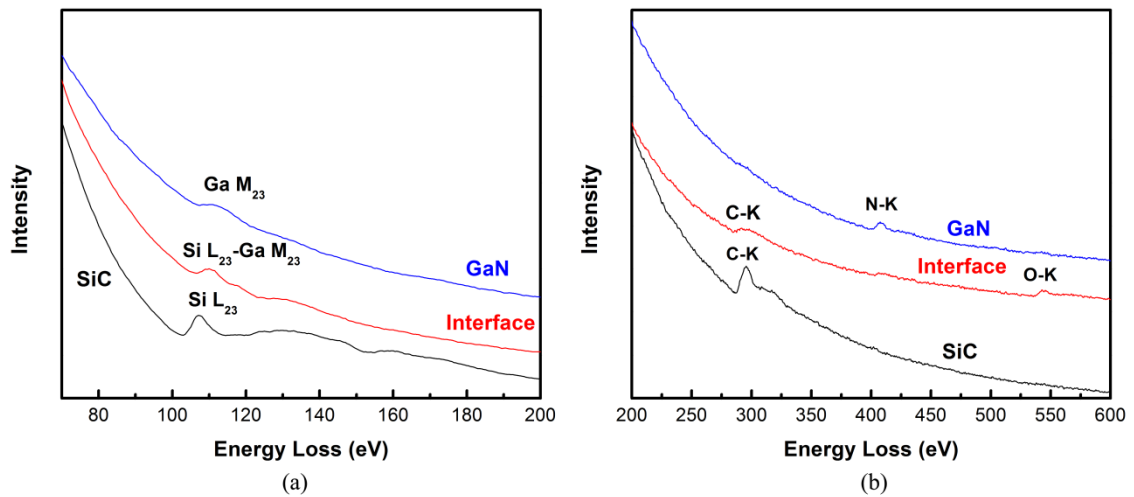


Figure 5-21. EELS spectra at GaN/SiC interface of GaN-#58.

On the other hand, as shown in Figure 5-21b, a sharp spectral feature of the carbon K edge EELS was observed in a perfect lattice in the SiC substrate. The broadening of this carbon K edge at the interface can be attributed to the fact that the coordinate of carbon is not well-defined compared to the coordination in the SiC substrate. The intensity of the carbon K edge EELS decreases from the SiC substrate to the GaN/SiC interface. The oxygen K edge EELS is detected in the GaN/SiC interface. The appearance of oxygen in the interface, together with the

aforementioned Si L<sub>23</sub> edge analysis, suggests that the amorphous layer is the native oxide layer on the SiC substrate.

The chemical analysis results by EELS together with 2D-XRD pole figures indicate that GaN thin films were grown epitaxially on 6H-SiC substrates even with the existence of an amorphous native oxide layer on 6H-SiC surface. This phenomenon was also observed if GaN was grown on (111) Si when an amorphous silicon nitride buffer layer was formed on the Si surface [195]. As the amorphous layer is only a few nanometers thick, the short-range coordination of each atom is somehow maintained, so it can transfer the crystal orientation of the substrate to the grown GaN layer. This is understandable, since G. R. Harp *et al.* inferred the distance of good short range order in native oxide layer on silicon is 40 Å by calculation of electron coherence length (comparable to good short range order distance) from X-ray absorption fine structure spectroscopy [196]. The measured amorphous layer thickness is 3.5 nm, which sits in the good short range order distance of the native oxide layer.

## **5.4 Effect of H<sub>2</sub> on GaN Thin Film Growth on SiC Substrate**

The formation of native oxide layer on SiC is recognized and pure hydrogen is widely used to remove surface oxide layers of SiC [197-200]. However, special procedures regarding safety handling of hydrogen need to be conducted for the

use of pure hydrogen. In this work, to simplify the operation procedure and to investigate the effect of hydrogen on the SiC surface treatment and GaN thin film growth, hydrogen was added into Ar and/or N<sub>2</sub> to form Ar: 5% H<sub>2</sub> and N<sub>2</sub>: 10% H<sub>2</sub> for the use of GaN thin film growth procedure. In addition, GaN thin films have rarely been grown at an elevated temperature in forming gas including hydrogen. In detail, GaN-#66 was grown in Ar: 5% H<sub>2</sub> and pure N<sub>2</sub> atmosphere and GaN-#67 was grown in Ar: 5% H<sub>2</sub> and N<sub>2</sub>: 10% H<sub>2</sub> atmosphere.

#### 5.4.1 XRD Studies of GaN Thin Films

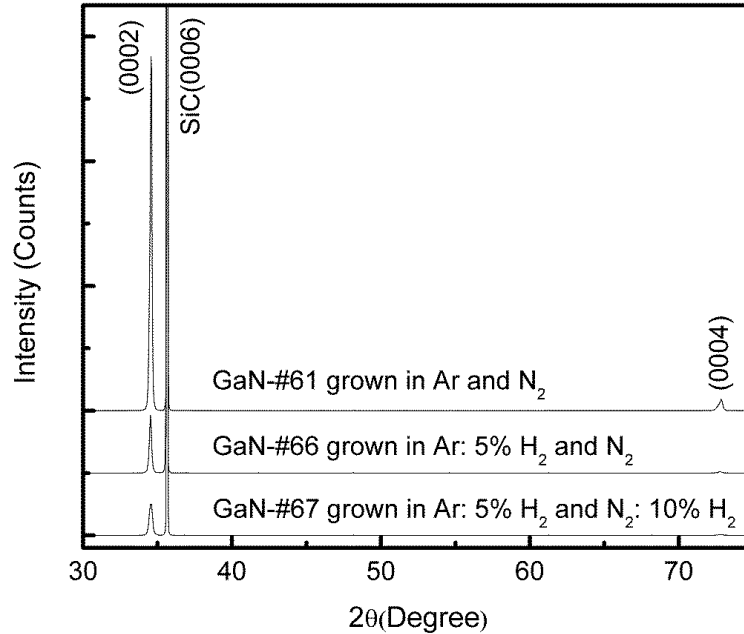


Figure 5-22. XRD patterns of GaN-#61, GaN-#66, and GaN-#67.

XRD patterns of GaN-#61, GaN-#66 and GaN-#67 are shown in Figure 5-22. The very strong peak at  $35.64^\circ$  is the (0006) reflection from the 6H-SiC single crystal substrate. GaN (0002) reflection intensity decreases by adding H<sub>2</sub> into the growth system. As mentioned in Section 5.3.1, the intensity of the (0002) peak of GaN-#61 is up to 56723 counts/sec, but it drops to 9238 counts/sec by adding 5% H<sub>2</sub> into Ar, and eventually goes down to 5002 counts/sec by adding 5% H<sub>2</sub> into Ar and 10% H<sub>2</sub> into N<sub>2</sub>. On the other hand, the GaN (0004) reflection intensity also decreases with the same trend as GaN (0002) reflection intensity by adding H<sub>2</sub>. All these factors suggest that adding H<sub>2</sub> into Ar and/or N<sub>2</sub> does not help to improve crystalline quality of GaN thin films.

#### 5.4.2 Surface Morphology of GaN Thin Films

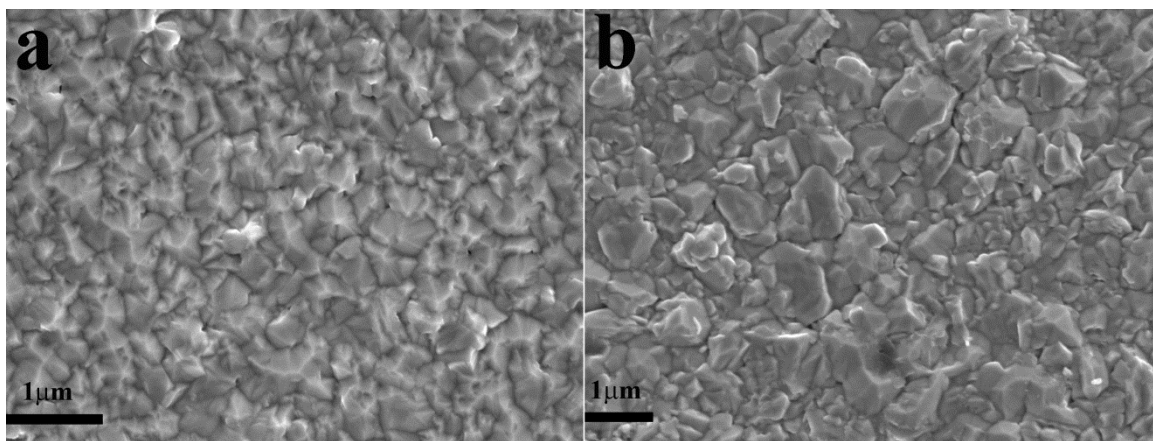


Figure 5-23. SEM micrographs of GaN-#66(a) and GaN-#67(b).

The surface morphology of GaN-#66 and GaN-#67 are shown in Figure 5-23. Unlike the surface morphology of GaN-#58 and GaN-#61 as shown in Figure 5-15, quite a number of the grains in GaN-#66 and GaN-#67 do not have a hexagonal hillock appearance. In addition, GaN-#67 appears more random than GaN-#66 in terms of surface morphology of each grain. The grain size distribution of GaN-#66 and GaN-#67 in Figure 5-24 shows us the latter has a wider grain size distribution than former. Being consistent with  $\theta$ -2 $\theta$  XRD patterns in Figure 5-22, SEM micrographs of these two specimens also demonstrated the crystalline quality of GaN-#66 is higher than GaN-#67.

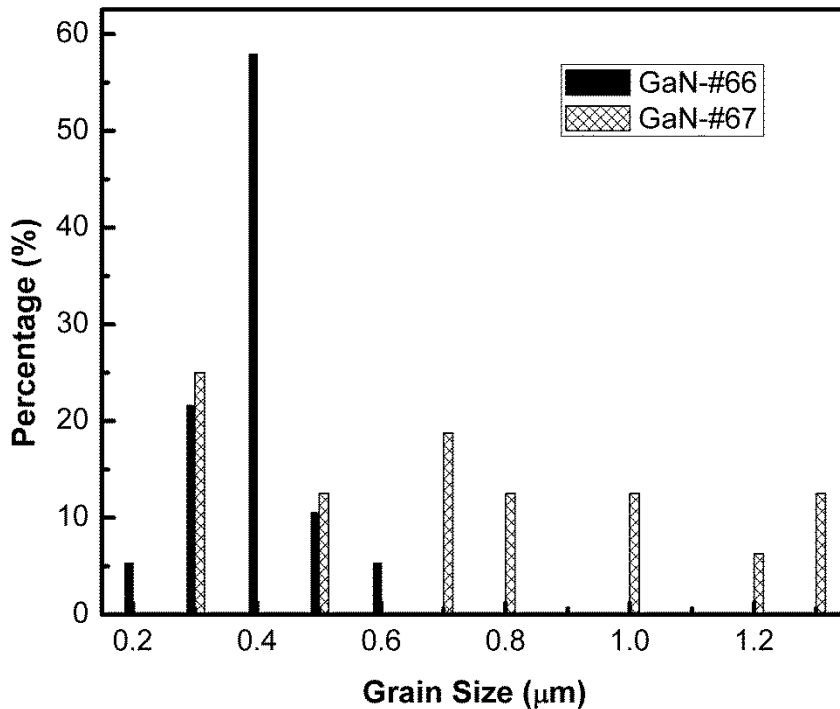


Figure 5-24. Grain size distribution of GaN-#66 and GaN-#67.

### 5.4.3 2D-XRD Pole Figures of GaN Thin Films

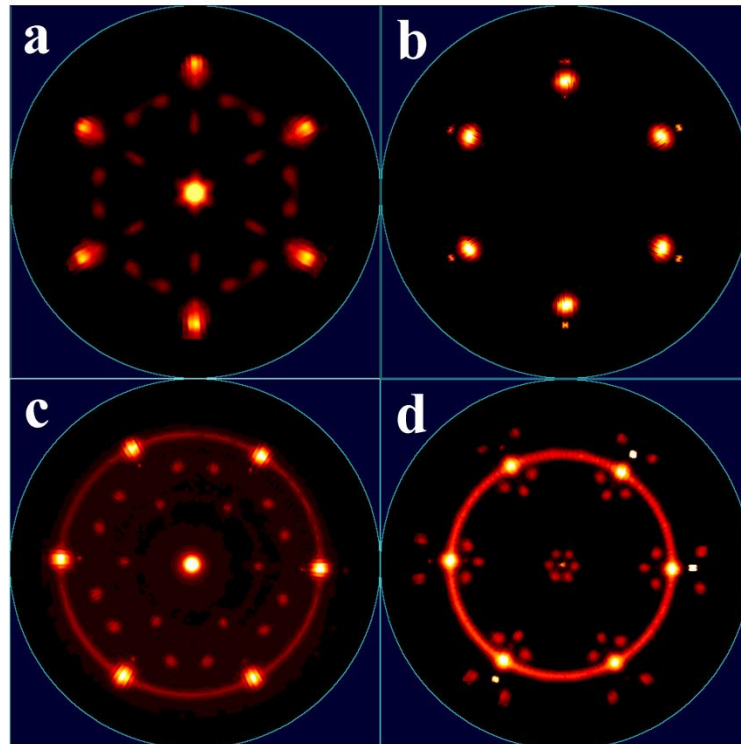
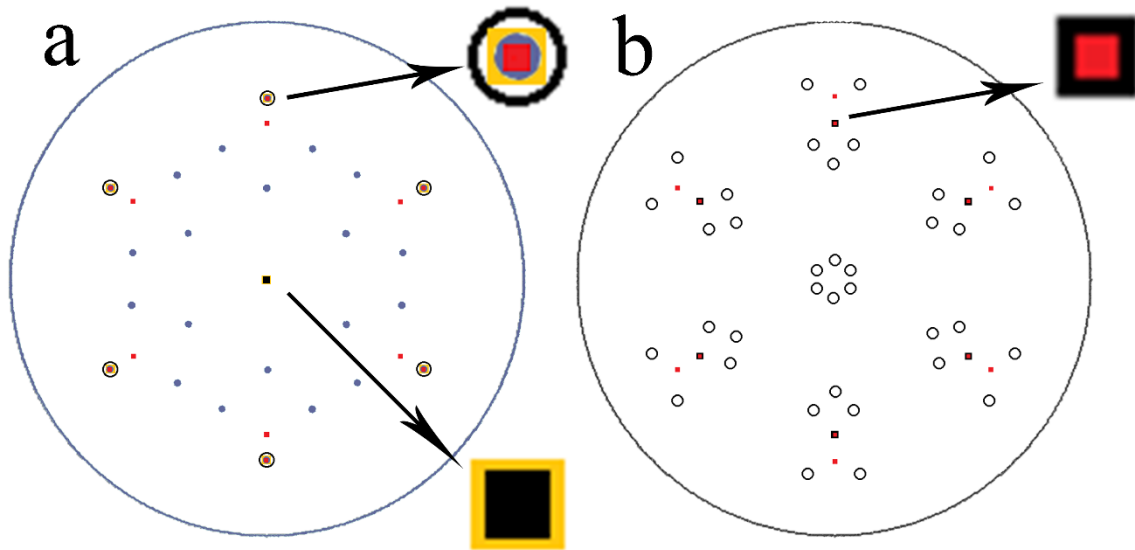


Figure 5-25. Pole figures of GaN-#66 and GaN-#67 obtained by 2D-XRD. a, (0002) pole figure of GaN-#66; b,  $\{10\bar{1}1\}$  pole figure of GaN-#66; c, (0002) pole figure of GaN-#67; d,  $\{10\bar{1}1\}$  pole figure of GaN-#67.



**Figure 5-26. a, simulated patterns of (0002) pole figure with all possible orientations; b, simulated patterns of  $\{10\bar{1}1\}$  pole figure with all possible orientations. Black squares, black circles, gold squares, blue dots, and red squares correspond to the poles from (0002) oriented wurtzite GaN,  $\{3\bar{3}02\}$  oriented wurtzite GaN,  $\{111\}$  oriented zinc-blende GaN,  $\{511\}$  oriented zinc-blende GaN, and 6H-SiC substrate, respectively. Note that  $\{111\}$  and  $\{511\}$  oriented zinc-blende GaN does not show up in  $\{10\bar{1}1\}$  pole figures because the  $2\theta$  range of  $\{10\bar{1}1\}$  pole figures does not cover any reflections from the zinc-blende GaN.**

For a comprehensive investigation and understanding of GaN thin film epitaxial relationship with 6H-SiC substrate, 2D-XRD were also conducted on GaN-#66 and GaN-#67 and the corresponding pole figures are shown in Figure 5-25. The orientations of these two samples can be figured out according to the pole figures in a manner similar to the one being used for GaN-#61 as described in Section 5.3.3. From the comparison between the experimental  $\{10\bar{1}1\}$  pole figure of GaN-

#66 as shown in Figure 5-25b and the simulated one as shown in Figure 5-26b, we find out that  $\{3\bar{3}02\}$  oriented wurtzite GaN does not show up in this sample. On the other hand, fiber textures were recorded in both  $(0002)$  and  $\{10\bar{1}1\}$  pole figures of GaN-#67, which were indicated from the rings in Figure 5-25c and Figure 5-25d. The ring shown in the  $(0002)$  pole figure (Figure 5-25c) is a fiber texture of  $\{111\}$  oriented zinc-blende GaN, and the ring shown in the  $\{10\bar{1}1\}$  pole figure (Figure 5-25d) is a fiber texture of  $(0001)$  oriented wurtzite GaN. Therefore, the intensities of these two rings are different. The orientations of GaN-#66 and GaN-#67 are summarized in Table 5-2.

**Table 5-2. Summary of GaN thin films orientations on 6H-SiC substrates for GaN-#66 and GaN-#67. (w-GaN: wurtzite GaN; z-GaN: zinc-blende GaN)**

Sample	Orientation-1	Orientation-2	Orientation-3	Orientation-4
GaN- #66	$(0001)_{\text{w-GaN}} \parallel (0001)_{\text{SiC}}$ $\langle 11\bar{2}0 \rangle_{\text{w-GaN}} \parallel \langle 11\bar{2}0 \rangle_{\text{SiC}}$	$\{111\}_{\text{z-GaN}} \parallel (0001)_{\text{SiC}}$ $\langle 01\bar{1} \rangle_{\text{z-GaN}} \parallel \langle 11\bar{2}0 \rangle_{\text{SiC}}$	N/A	$\{511\}_{\text{z-GaN}} \parallel (0001)_{\text{SiC}}$ $\langle 01\bar{1} \rangle_{\text{z-GaN}} \parallel \langle 11\bar{2}0 \rangle_{\text{SiC}}$
GaN- #67	$(0001)_{\text{w-GaN}} \parallel (0001)_{\text{SiC}}$	$\{111\}_{\text{z-GaN}} \parallel (0001)_{\text{SiC}}$	$\{3\bar{3}02\}_{\text{w-GaN}} \parallel (0001)_{\text{SiC}}$ $\langle 11\bar{2}0 \rangle_{\text{w-GaN}} \parallel \langle 11\bar{2}0 \rangle_{\text{SiC}}$	$\{511\}_{\text{z-GaN}} \parallel (0001)_{\text{SiC}}$ $\langle 01\bar{1} \rangle_{\text{z-GaN}} \parallel \langle 11\bar{2}0 \rangle_{\text{SiC}}$

#### 5.4.4 GaN/SiC Interfacial Structure and Chemical Composition

To investigate the initial growth stage of GaN thin films in GaN-#66 and GaN-#67, the interfacial structure of GaN and the SiC substrate was also characterized by HAADF imaging and ABF imaging in a STEM and the results are shown in Figure 5-27. The chemical analysis of the GaN/SiC interface in GaN-#66 and GaN-#67 was carried out by EELS and the results are shown in Figure 5-28. Similar to the amorphous layer in GaN-#58, we suggest that the amorphous layers in the GaN/SiC interfaces of GaN-#66 and GaN-#67 are native oxide layers on the substrates. However, these native oxide layers were found to have reduced thicknesses (3 nm for GaN-#66, 2.5 nm for GaN-#67) relative to GaN-#58. Moreover, as shown in Figure 5-27a and Figure 5-27b, a crystalline zone in the GaN/SiC interface was found in GaN-#66 (highlighted in Figure 5-27a).

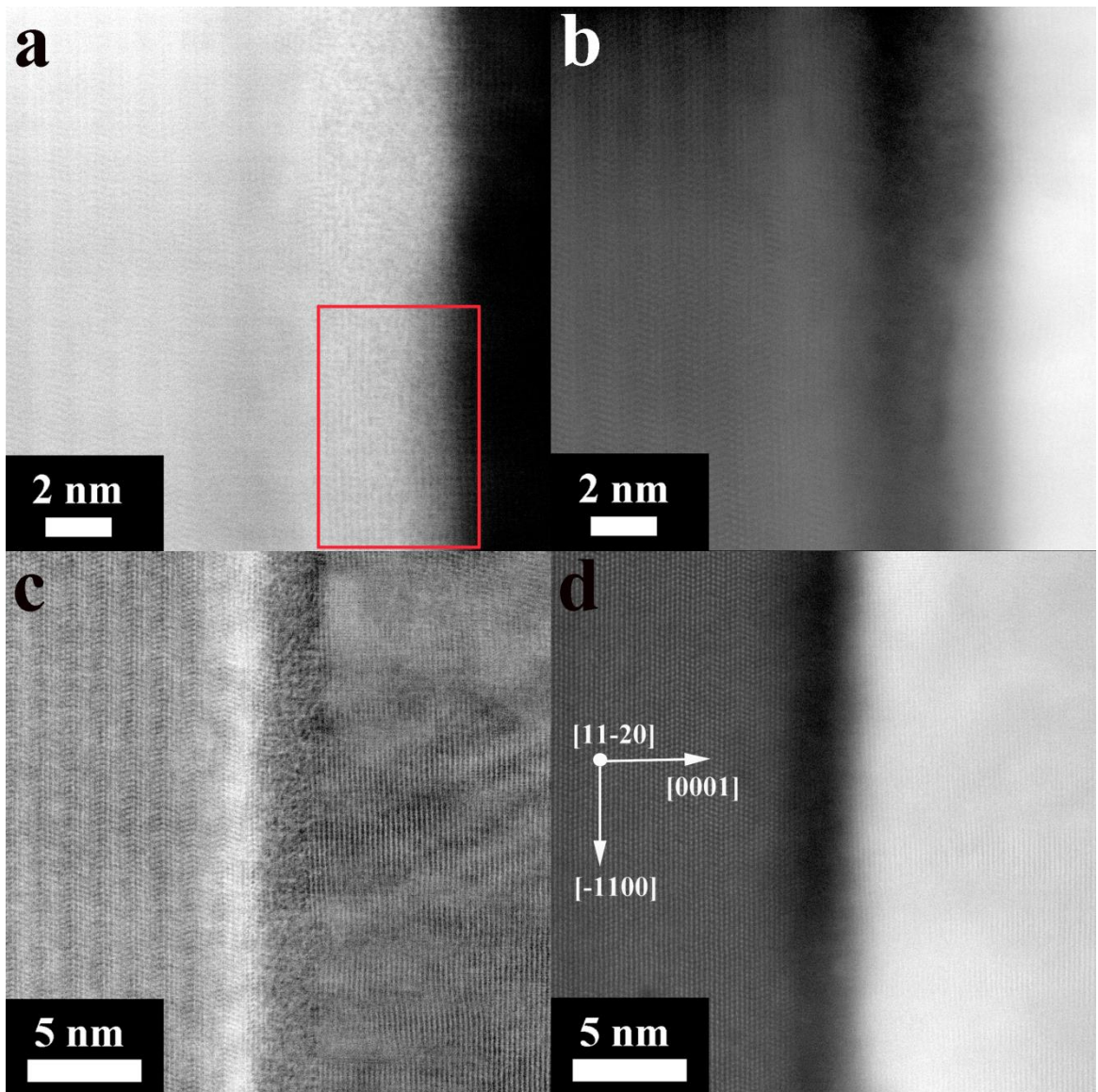
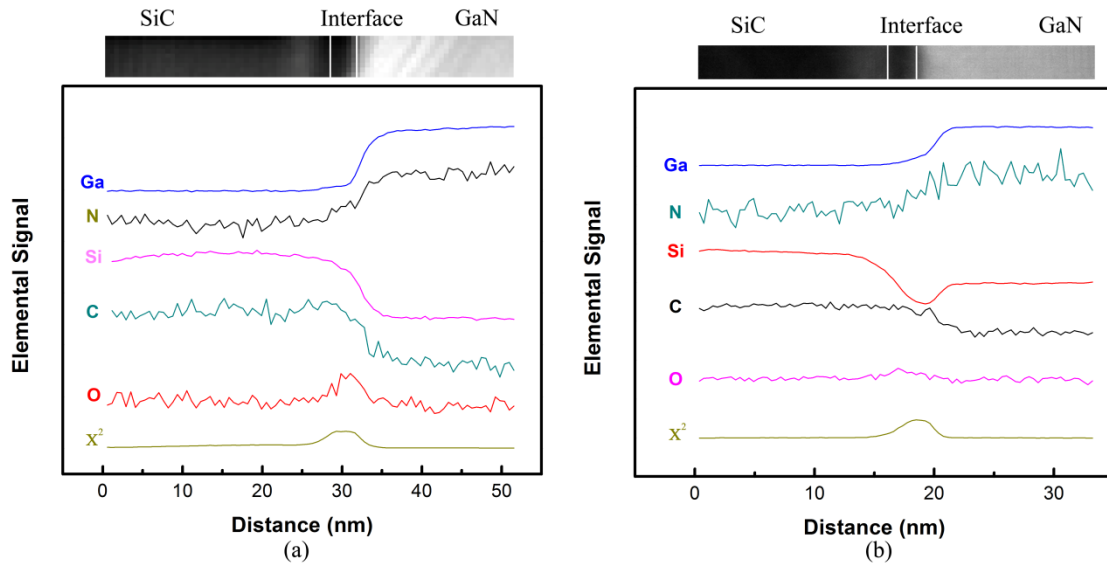


Figure 5-27. a, ABF image of GaN/SiC interface of GaN-#66, note that the crystalline zone in native oxide layer is highlighted in a red rectangular; b, HAADF image of GaN/SiC interface of GaN-#66; c, ABF image of GaN/SiC interface of GaN-#67; d, HAADF image of GaN/SiC interface of GaN-#67. Note that Figure c & d were taken on the same area simultaneously, Figure e & f were taken on the same area simultaneously. The crystallographic directions are identical in Figure a, b, c, d.



**Figure 5-28. a, elemental profiles across GaN/SiC interface of GaN-#66 by EELS and HAADF image of scanned area; b, elemental profiles across GaN/SiC interface of GaN-#67 by EELS and HAADF image of scanned area. Ga L<sub>23</sub> edge, N K edge, Si L<sub>23</sub> edge, C K edge, and O K edge are used for each profile. Note that because the EELS spectral features of Si L<sub>23</sub> edge and Ga-M<sub>23</sub> edge overlap, Ga L<sub>23</sub> edge signal are used instead of Ga M<sub>23</sub> edge signal to calculate Ga profile, Si profile are obtained by the MLLS fitting from the overlapped Si L<sub>23</sub> edge and Ga M<sub>23</sub> edge peak. Chi-squared test was carried out to measure the degree of fitting, and a large difference between observed and expected outcome was found at the interface, which indicates the fitted Si profile at the interface is not accurate.**

We find the amorphous layer thickness decreases with the amount of H<sub>2</sub> in the system: 3.5 nm for GaN-#58, 3 nm for GaN-66 and 2.5 nm for GaN-#67. This clearly demonstrates that by using Ar-H<sub>2</sub> forming gas during the heat treatment step of 6H-SiC substrate, the amorphous native silicon oxide layer on SiC can be partially removed. In Figure 5-27a, a crystalline zone is found in the lower part of the silicon oxide layer in GaN-#66 as highlighted in a red rectangular, which indicates that with the addition of H<sub>2</sub>, although the amorphous layer cannot be

removed completely, a phase transformation from amorphous to crystalline structure can take place at or near the SiC surface. The chemical reaction between silicon oxide and hydrogen can be illustrated as follows:  $\text{Si}_x\text{O}_y + y\text{H}_2 = x\text{Si} + y\text{H}_2\text{O}$ . If this chemical reaction takes place on the top layer of the SiC surface, water will readily evaporate by heating (at 900°C) and silicon can be sublimated by heating in vacuum as well. However, if it occurs in the crystalline zone of sample C as shown in the highlighted zone in Figure 5-27a, water molecules will still evaporate as the substrate temperature is much higher than the boiling point of water, but silicon will be trapped by the covalent bonding between silicon atoms and the adjacent atoms.

As mentioned in Section 5.3, GaN thin films can be grown epitaxially on 6H-SiC substrate even with the existence of a native oxide layer on SiC. The mechanism responsible for it has been explained in Section 5.3 as well. For GaN-#66, with the existence of a crystalline region at GaN/SiC interface, orientation-3 of GaN thin film was eliminated as indicated by 2D-XRD pole figures, as the crystalline area at the interface should perform better for the transfer of substrate orientation. However, the intensity of (0002) reflections in  $\theta$ -2 $\theta$  XRD patterns of GaN-#66 is lower than GaN-#61 even with the existence of crystalline area in the native oxide layer; the reason can be attributed to the effect of H<sub>2</sub> during growth. The details are illustrated in the next paragraph.

In GaN-#67, GaN thin film structures change from epitaxially grown thin films into (0002) oriented wurtzite GaN and {111} oriented zinc-blende GaN fiber textures, as demonstrated by 2D-XRD. Previous studies of hydrogen introduced during GaN sputtering growth at room temperature demonstrated that hydrogen related  $\text{GaNH}_3^+$  and  $\text{GaNH}_2$  molecules can be created within the deposited thin films, and those films deposited in  $\text{N}_2\text{-H}_2$  atmosphere are amorphous[6]. In the current work, the substrate temperature was set at  $700^\circ\text{C}$ , which provides sufficient kinetic energy for the incoming adatoms to diffuse on the substrate surface and eventually form a (0002) oriented thin film. However, the addition of  $\text{H}_2$  in Ar and  $\text{N}_2$  has made the GaN thin film growth more complicated than that in GaN-#61 and GaN-#66, as the formation and decomposition of  $\text{GaNH}_3^+$  and  $\text{GaNH}_2$  molecules at the elevated growth temperature has impeded the adatoms from strictly following the substrate orientation. Thus, it is demonstrated that in Ar- $\text{H}_2$  and  $\text{N}_2\text{-H}_2$  atmospheres, GaN thin film with (0002) oriented wurtzite GaN and {111} oriented zinc-blende GaN fiber textures was deposited on the SiC substrate.

## 6 Conclusion

In this work, a new method including a series of steps was invented for the precise alignment of SiC whiskers and further manipulation of aligned SiC whiskers for the epitaxial growth of GaN thin films. To take advantage of the versatility and scalability of sputtering, a reactive DC-magnetron sputtering system was built for the growth of high quality GaN thin films. A series of experiments was done to investigate GaN growth behavior on SiC substrates in the sputtering system. The conclusions can be drawn as follows:

1. Patterned 3M Vikuiti™ Brightness Enhancement Film is an effective alignment template for SiC whiskers; the degree of whisker alignment achieved in this way is higher than that achieved by extrusion.
2. The aligned whiskers can be transferred into an alumina matrix by tape casting and sintered with the protection of an alumina-SiC<sub>w</sub> mixture without excessive oxidation of the aligned whiskers. The conventional hot-pressing step was eliminated for the preservation of SiC whiskers alignment.
3. The crystalline quality of GaN thin films is highly sensitive to contaminations in the sputtering chamber. Both residual oxygen in the chamber and copper contamination in the gallium target can have a negative effect on the crystalline quality of GaN thin films. Once the residual oxygen was controlled at a reasonably low level and the copper contamination in the gallium target was eliminated, the crystalline quality of

GaN thin films was improved dramatically.  $\theta$ - $2\theta$  XRD patterns and the XRRC demonstrate that (0002) oriented high quality GaN thin film can be grown on 6H-SiC even with the existence of native oxide layer on the 6H-SiC substrate. The FWHM of the XRRC of GaN thin films grown in this work can be as low as 50 arcmin, which indicates that the crystalline quality of corresponding specimens is high among literature GaN thin films grown by sputtering.

4. Sputtering growth time has an influence on the stoichiometric nature of GaN thin films. Large gallium clusters can be formed on the specimen surface during sputtering due to Oswald ripening induced by long sputtering time and the chemical reaction between gallium clusters and nitrogen will be insufficient as the GaN formed on the cluster surface can have a passivation effect on the reaction between inner gallium atoms and nitrogen. GaN thin films grown for long sputtering times have a reduced (0002) reflection intensity than those grown for short sputtering times according to  $\theta$ - $2\theta$  XRD patterns.
5. HAADF images obtained by STEM shows the epitaxial growth of GaN thin films on 6H-SiC substrates relies on the short range order of the amorphous native oxide layer on SiC. The addition of 5% H<sub>2</sub> into Ar can reduce the native oxide layer thickness and can also induce a phase transformation from amorphous to crystalline in some area of native oxide layer according to ABF images obtained by STEM. The existence of a

crystalline zone in the native oxide layer can eliminate one unwanted minor-orientation (orientation-3) in GaN thin films according 2D-XRD pole figures. However, GaN thin film with fiber texture can be grown in Ar: 5% H<sub>2</sub> and N<sub>2</sub>: 10% H<sub>2</sub> as the amount of H<sub>2</sub> at this level can have complex reactions with N<sub>2</sub> at an elevated growth temperature.

In the future, recommended work is to investigate the GaN growth behavior on the (111) plane of aligned SiC whiskers and related properties. This includes several steps as follows:

1. Upgrade sputtering chamber to an ultra high vacuum system with a background pressure of  $10^{-10}$  Torr for the use of pure H<sub>2</sub> for the complete elimination of native oxide layer on SiC. Work needs to be carried out for the upgrade and safe handling of H<sub>2</sub>.
2. A specific characterization method needs to be developed because the exposed (111) planes of aligned whiskers only have an average diameter of 1.5  $\mu\text{m}$ , and conventional crystal structure characterization methods cannot accurately focus on this tiny area. Focused ion beam (FIB) can be an effective tool for the preparation of cross-sections of STEM samples as FIB is able to find regions of interest and surrounding materials can be milled away.

3. More work is needed to find the electrical and luminescent properties of the as-grown GaN thin films, thus providing a comprehensive understanding of the properties of GaN thin films grown in this work.

## References

1. Ponce, F.A. and D.P. Bour, *Nitride-based semiconductors for blue and green light-emitting devices*. *Nature*, 1997. 386(6623): p. 351-359.
2. Nakamura, S., *The roles of structural imperfections in InGaN-Based blue light-emitting diodes and laser diodes*. *Science*, 1998. 281(5379): p. 956-961.
3. Perkins, J. *LED Manufacturing Technologies & Costs*. 2009.
4. Narendran, N. *LED Technology*. 2005; Available from: <http://www.ceat.uiuc.edu/PUBLICATIONS/brownbag/presentations/Aug%2005%20Nadarajah%20Narendran.pdf>.
5. Sharma, N.K., W.S. Williams, and A. Zangvil, *FORMATION AND STRUCTURE OF SILICON-CARBIDE WHISKERS FROM RICE HULLS*. *Journal of the American Ceramic Society*, 1984. 67(11): p. 715-720.
6. Miyazaki, T., et al., *Properties of radio-frequency-sputter-deposited GaN films in a nitrogen/hydrogen mixed gas*. *Journal of Applied Physics*, 2005. 97(9).
7. Yadav, B.S., S.S. Major, and R.S. Srinivasa, *Growth and structure of sputtered gallium nitride films*. *Journal of Applied Physics*, 2007. 102(7).
8. Goto, Y. and A. Tsuge, *MECHANICAL-PROPERTIES OF UNIDIRECTIONALLY ORIENTED SIC-WHISKER-REINFORCED Si3N4 FABRICATED BY EXTRUSION AND HOT-PRESSING*. *Journal of the American Ceramic Society*, 1993. 76(6): p. 1420-1424.
9. Round, H.J., *A note on carborundum*. *Electrical World*, 1907. 49(309).
10. Losev, O.V., *Luminous carborundum [silicon carbide] detector and detection with crystals*. *Telegrafiya i Telefoniya bez Provodov*, 1927. 44: p. 485-494.
11. Whelan, M. *Small lights with big potential: light emitting diodes & organic light emitting diodes Commercial History (1960s - Today)*. 2013 [cited 2013 Jun. 5, 2013]; Available from: <http://www.edisontechcenter.org/LED.html>.

12. Shuji Nakamura, T.M., Masayuki Senoh and Naruhito Iwasa, *Thermal Annealing Effects on P-Type Mg-Doped GaN Films*. Japanese Journal of Applied Physics, 1992. 31: p. L139-L142.
13. Kuo, C.P., et al., *High performance AlGaInP visible light - emitting diodes*. Applied Physics Letters, 1990. 57(27): p. 2937-2939.
14. Chang, S.J. and C.S. Chang, *650 nm AlGaInP/GaInP compressively strained multi-quantum well light emitting diodes*. Japanese Journal of Applied Physics Part 2-Letters, 1998. 37(6A): p. L653-L655.
15. Chang, S.J., et al., *AlGaInP multiquantum well light-emitting diodes*. IEEE Proceedings-Optoelectronics, 1997. 144(6): p. 405-409.
16. Kish, F.A.a.F., R. M., *AlGaInP light-emitting diodes*, in *Semiconductors and Semimetals*, G.B.S.a.M.G. Craford, Editor. 1997, Academic Press: San Diego. p. 149.
17. Krames, M.R., et al., *High-power truncated-inverted-pyramid (Al<sub>x</sub>Ga<sub>1-x</sub>)<sub>0.5</sub>In<sub>0.5</sub>P/GaP light-emitting diodes exhibiting >50% external quantum efficiency*. Applied Physics Letters, 1999. 75(16): p. 2365-2367.
18. H. P. Maruska, J.J.T., *THE PREPARATION AND PROPERTIES OF VAPOR - DEPOSITED SINGLE - CRYSTAL - LINE GaN*. Applied Physics Letters, 1969. 15(10): p. 327-329.
19. Pankove, J.I., Miller, E. A. & Berkeyheiser, J. E. , *GaN Electroluminescent Diodes*. RCA Review, 1971. 32: p. 383-392.
20. Manasevit, H.M.E., F. M. & Simpson, W. I., *The use of metalorganics in the preparation of semiconductor materials*. J. Electrochem. Soc., 1971. 118: p. 1864-1868.
21. Dingle, R., Shaklee, K. L., Leheny, R. F. & Zetterstrom, R. B., *Stimulated emission and laser action in gallium nitride*. Applied Physics Letters, 1971. 19(1): p. 5-7.
22. Matsumoto T. & Aoki, M., *Temperature dependence of photoluminescence from GaN*. Japanese Journal of Applied Physics, 1974. 13: p. 1804-1807.
23. Akasaki, I.H., I., *Research on blue emitting devices*. Ind. Sci. Technol., 1976. 17: p. 48-52.

24. S. Yoshida, S.M., & A. Itoh, *Epitaxial growth of aluminum nitride films on sapphire by reactive evaporation*. Applied Physics Letters, 1975. 26(8): p. 461-462.
25. Karpinski, J., S. Porowski, and S. Miotkowska, *HIGH-PRESSURE VAPOR GROWTH OF GAN*. Journal of Crystal Growth, 1982. 56(1): p. 77-82.
26. Yoshida, S., S. Misawa, and S. Gonda, *IMPROVEMENTS ON THE ELECTRICAL AND LUMINESCENT PROPERTIES OF REACTIVE MOLECULAR-BEAM EPITAXIALLY GROWN GAN FILMS BY USING AIN-COATED SAPPHIRE SUBSTRATES*. Applied Physics Letters, 1983. 42(5): p. 427-429.
27. Amano, H., et al., *METALORGANIC VAPOR-PHASE EPITAXIAL-GROWTH OF A HIGH-QUALITY GAN FILM USING AN AIN BUFFER LAYER*. Applied Physics Letters, 1986. 48(5): p. 353-355.
28. Amano, H., et al., *P-TYPE CONDUCTION IN MG-DOPED GAN TREATED WITH LOW-ENERGY ELECTRON-BEAM IRRADIATION (LEEBI)*. Japanese Journal of Applied Physics Part 2-Letters, 1989. 28(12): p. L2112-L2114.
29. Nagatomo, T., et al., *PROPERTIES OF GA<sub>1-X</sub>IN<sub>X</sub>N FILMS PREPARED BY MOVPE*. Japanese Journal of Applied Physics Part 2-Letters, 1989. 28(8): p. L1334-L1336.
30. Nakamura, S., *GaN Growth Using GaN Buffer Layer*. Jpn. J. Appl. Phys., 1991. 30: p. L1705-L1707.
31. Akasaki, I., Amano, H., Itoh, K., Koide, N. & Manabe, K., *GaN-based ultraviolet/blue light emitting devices*. Inst. Phys. Conf. Ser. , 1992. 129: p. 851-856.
32. Nakamura, S.M., T. High-quality InGaN films grown on GaN films., *High-quality InGaN films grown on GaN films*. Jpn. J. Appl. Phys., 1992. 31: p. L1457-L1459.
33. Nakamura, S., et al., *INXGA(1-X)N/INYGA(1-Y)N SUPERLATTICES GROWN ON GAN FILMS*. Journal of Applied Physics, 1993. 74(6): p. 3911-3915.
34. Nakamura, S., T. Mukai, and M. Senoh, *CANDELA-CLASS HIGH-BRIGHTNESS INGAN/ALGAN DOUBLE-HETEROSTRUCTURE BLUE-LIGHT-EMITTING DIODES*. Applied Physics Letters, 1994. 64(13): p. 1687-1689.

35. Nakamura, S., T. Mukai, and M. Senoh, *HIGH-BRIGHTNESS INGAN/ALGAN DOUBLE-HETEROSTRUCTURE BLUE-GREEN-LIGHT-EMITTING DIODES*. *Journal of Applied Physics*, 1994. 76(12): p. 8189-8191.
36. Nakamura, S., et al., *HIGH-BRIGHTNESS INGAN BLUE, GREEN AND YELLOW LIGHT-EMITTING-DIODES WITH QUANTUM-WELL STRUCTURES*. *Japanese Journal of Applied Physics Part 2-Letters*, 1995. 34(7A): p. L797-L799.
37. Nakamura, S., et al., *SUPERBRIGHT GREEN INGAN SINGLE-QUANTUM-WELL-STRUCTURE LIGHT-EMITTING-DIODES*. *Japanese Journal of Applied Physics Part 2-Letters*, 1995. 34(10B): p. L1332-L1335.
38. Nakamura, S., et al., *InGaN-based multi-quantum-well-structure laser diodes*. *Japanese Journal of Applied Physics Part 2-Letters*, 1996. 35(1B): p. L74-L76.
39. Akasaki, I., et al., *Shortest wavelength semiconductor laser diode*. *Electronics Letters*, 1996. 32(12): p. 1105-1106.
40. Itaya, K., et al., *Room temperature pulsed operation of nitride based multi-quantum-well laser diodes with cleaved facets on conventional C-face sapphire substrates*. *Japanese Journal of Applied Physics Part 2-Letters*, 1996. 35(10B): p. L1315-L1317.
41. Nakamura, S., *Characteristics of InGaN Multiquantum-Well-Structure Laser Diodes*. *MRS Online Proceedings Library*, 1996. 449: p. null-null.
42. Shimizu, Y., *Development of White LED light source*. *Rare earths*, 2002. 40: p. 150-151.
43. *Cree's New Lighting-Class LEDs Shatter Industry Performance Standards 2010*; Available from: <http://www.cree.com/news-and-events/cree-news/press-releases/2010/november/101110-xml>.
44. *Press Information*. [Philips Lumileds website] 2013 [cited 2013-07-07]; Available from: <http://www.philipslumileds.com/uploads/news/id215/PR198.pdf>.
45. Iveland, J., et al., *Direct Measurement of Auger Electrons Emitted from a Semiconductor Light-Emitting Diode under Electrical Injection: Identification of the Dominant Mechanism for Efficiency Droop*. *Physical Review Letters*, 2013. 110(17).

46. Holonyak, N. and S.F. Bevacqua, **COHERENT (VISIBLE) LIGHT EMISSION FROM Ga(As<sub>1-x</sub>P<sub>x</sub>) JUNCTIONS**. Applied Physics Letters, 1962. 1(4): p. 82-83.
47. Holonyak, N., et al., **THE 'DIRECT - INDIRECT' TRANSITION IN Ga(As<sub>1-x</sub>P<sub>x</sub>) p - n JUNCTIONS**. Applied Physics Letters, 1963. 3(3): p. 47-49.
48. Holonyak, N., et al., **EFFECT OF DONOR IMPURITIES ON THE DIRECT - INDIRECT TRANSITION IN Ga(As<sub>1-x</sub>P<sub>x</sub>)**. Applied Physics Letters, 1966. 8(4): p. 83-85.
49. Pilkuhn, M. and H. Rupprecht, **Electroluminescence and Lasing Action in GaAs<sub>x</sub>P<sub>1-x</sub>**. Journal of Applied Physics, 1965. 36(3): p. 684-688.
50. Wolfe, C.M., C.J. Nuese, and N. Holonyak, **Growth and Dislocation Structure of Single - Crystal Ga (As<sub>1-x</sub>P<sub>x</sub>)**. Journal of Applied Physics, 1965. 36(12): p. 3790-3801.
51. Nuese, C.J., et al., **Gallium arsenide-phosphide: Crystal, diffusion and laser properties**. Solid-State Electronics, 1966. 9(8): p. 735-749.
52. Schubert, E.F., in **Light-Emitting Diodes**. 2006, Cambridge University Press. p. 201.
53. Schubert, E.F., in **Light-Emitting Diodes**. 2006, Cambridge University Press. p. 202.
54. Grimmeiss, H.G. and H. Scholz, **Efficiency of recombination radiation in GaP**. Physics Letters, 1964. 8(4): p. 233-235.
55. Logan, R.A., H.G. White, and F.A. Trumbore, **p - n Junctions in Compensated Solution - Grown GaP**. Journal of Applied Physics, 1967. 38(6): p. 2500-2508.
56. Logan, R.A., H.G. White, and F.A. Trumbore, **P - N JUNCTIONS IN GaP WITH EXTERNAL ELECTROLUMINESCENCE EFFICIENCY ~2% AT 25°C**. Applied Physics Letters, 1967. 10(7): p. 206-208.
57. Logan, R.A., H.G. White, and W. Wiegmann, **Efficient green electroluminescent junctions in GaP**. Solid-State Electronics, 1971. 14(1): p. 55-70.

58. Craford, M.G., et al., *Radiative recombination mechanisms in GaAsP diodes with and without nitrogen doping*. Journal of Applied Physics, 1972. 43(10): p. 4075-4083.
59. Groves, W.O., Herzog, A. H., and Craford M. G., *Process for the preparation of electroluminescent III-V materials containing isoelectronic impurities*, in *USPTO patent full-text and image database*, U.S.P.a.T. Office, Editor 1978, Monsanto (St. Louis, MO): United States.
60. Groves, W.O.a.E., A. S., *Epitaxial deposition of III-V compounds containing isoelectronic impurities*, in *USPTO patent full-text and image database*, U.S.P.a.T. Office, Editor 1977, Monsanto Company (St. Louis, MO) United States.
61. Schubert, E.F., in *Light-Emitting Diodes*. 2006, Cambridge University Press. p. 206.
62. Schubert, E.F., in *Light-Emitting Diodes*. 2006, Cambridge University Press. p. 207.
63. Schubert, E.F., in *Light-Emitting Diodes*. 2006, Cambridge University Press. p. 208.
64. Ishiguro, H., et al., *High efficient GaAlAs light - emitting diodes of 660 nm with a double heterostructure on a GaAlAs substrate*. Applied Physics Letters, 1983. 43(11): p. 1034-1036.
65. Ishimatsu, S.a.O., Y., *High efficiency GaAlAs LED*. Optoelectronics-devices and technologies, 1989. 4: p. 21.
66. F. M. Steranka, D.C.D., M. D. Camras, C.-W. Tu, D. K. McElfresh, S. L. Rudaz, L. W. Cook, and W. L. Snyder, *Red AlGaAs light emitting diodes*. Hewlett-Packard Journal, 1988: p. 84.
67. Schubert, E.F., in *Light-Emitting Diodes*. 2006, Cambridge University Press. p. 209.
68. Schubert, E.F., in *Light-Emitting Diodes*. 2006, Cambridge University Press. p. 211.
69. Schubert, E.F., in *Light-Emitting Diodes*. 2006, Cambridge University Press. p. 210.
70. Chen, C.H., Stockman, S. A., Peanasky M. J., and Kuo, C. P., *OMVPE growth of AlGaInP for high-efficiency visible light-emitting diodes*, in

- Semiconductors and Semimetals*, G.B.S.a.M.G. Craford, Editor. 1997, Academic Press: San Diego.**
71. Prins, A.D., et al., ***High pressure determination of AlGaInP band structure***. *Journal of Physics and Chemistry of Solids*, 1995. 56(3–4): p. 349-352.
  72. Kish, F.A.a.F., R. M., ***AlGaInP light-emitting diodes***, in ***Semiconductors and Semimetals***, G.B.S.a.M.G. Craford, Editor. 1997, Academic Press: San Diego.
  73. Schubert, E.F., in ***Light-Emitting Diodes***. 2006, Cambridge University Press. p. 223.
  74. Siozade, L., et al., ***Modelling of thermally detected optical absorption and luminescence of (In,Ga)N/GaN heterostructures***. *Solid State Communications*, 2000. 115(11): p. 575-579.
  75. Wu, J., et al., ***Universal bandgap bowing in group-III nitride alloys***. *Solid State Communications*, 2003. 127(6): p. 411-414.
  76. Yun, F., et al., ***Energy band bowing parameter in Al<sub>x</sub>Ga<sub>1-x</sub>N alloys***. *Journal of Applied Physics*, 2002. 92(8): p. 4837-4839.
  77. Schubert, E.F., in ***Light-Emitting Diodes***. 2006, Cambridge University Press. p. 59-62.
  78. Ben G. Streetman, S.K.B., in ***Solid State Electronic Devices***. 2000, Pearson Prentice Hall. p. 184.
  79. Schubert, E.F., in ***Light-Emitting Diodes***. 2006, Cambridge University Press. p. 62.
  80. Schubert, E.F., in ***Light-Emitting Diodes***. 2006, Cambridge University Press. p. 69.
  81. Schubert, E.F., in ***Light-Emitting Diodes***. 2006, Cambridge University Press. p. 83.
  82. Schubert, E.F., in ***Light-Emitting Diodes***. 2006, Cambridge University Press. p. 84.
  83. Michael J. Scholand, H.E.D., ***Life-Cycle Assessment of Energy and Environmental Impact of LED lighting Products***, 2012, U.S. Department of Energy.
  84. Morkoç, H., in ***Handbook of Nitride Semiconductors and Devices***. 2008, WILEY-VCH Verlag GmbH & Co. KGaA.

85. Xia, Q., H. Xia, and A.L. Ruoff, *Pressure - induced rocksalt phase of aluminum nitride: A metastable structure at ambient condition*. Journal of Applied Physics, 1993. 73(12): p. 8198-8200.
86. Perlin, P., et al., *Raman scattering and x-ray-absorption spectroscopy in gallium nitride under high pressure*. Physical Review B, 1992. 45(1): p. 83-89.
87. Ueno, M., et al., *Stability of the wurtzite-type structure under high pressure: GaN and InN*. Physical Review B, 1994. 49(1): p. 14-21.
88. Powell, R.C., et al., *Heteroepitaxial wurtzite and zinc - blende structure GaN grown by reactive - ion molecular - beam epitaxy: Growth kinetics, microstructure, and properties*. Journal of Applied Physics, 1993. 73(1): p. 189-204.
89. Mizuta, M., et al., *LOW-TEMPERATURE GROWTH OF GAN AND ALN ON GAAS UTILIZING METALORGANICS AND HYDRAZINE*. Japanese Journal of Applied Physics Part 2-Letters, 1986. 25(12): p. L945-L948.
90. Paisley, M.J., et al., *Growth of cubic phase gallium nitride by modified molecular - beam epitaxy*. Journal of Vacuum Science & Technology A, 1989. 7(3): p. 701-705.
91. Lei, T., et al., *Epitaxial growth of zinc blende and wurtzitic gallium nitride thin films on (001) silicon*. Applied Physics Letters, 1991. 59(8): p. 944-946.
92. Tanaka, M., et al., *Morphology and X-ray diffraction peak widths of aluminum nitride single crystals prepared by the sublimation method*. Japanese Journal of Applied Physics Part 2-Letters, 1997. 36(8B): p. L1062-L1064.
93. Angerer, H., et al., *Determination of the Al mole fraction and the band gap bowing of epitaxial Al<sub>x</sub>Ga<sub>1-x</sub>N films*. Applied Physics Letters, 1997. 71(11): p. 1504-1506.
94. Domagala, J., et al., *Strain relaxation of Al<sub>x</sub>Ga<sub>1-x</sub>N epitaxial layers on GaN and SiC substrates*. Journal of Alloys and Compounds, 1999. 286(1-2): p. 284-288.
95. Kim, K., W.R.L. Lambrecht, and B. Segall, *Elastic constants and related properties of tetrahedrally bonded BN, AlN, GaN, and InN*. Physical Review B, 1996. 53(24): p. 16310-16326.

96. Wright, A.F. and J.S. Nelson, *Consistent structural properties for AlN, GaN, and InN*. Physical Review B, 1995. 51(12): p. 7866-7869.
97. Leszczynski, M., et al., *Lattice parameters of gallium nitride*. Applied Physics Letters, 1996. 69(1): p. 73-75.
98. Detchprohm, T., et al., *RELAXATION PROCESS OF THE THERMAL STRAIN IN THE GAN/ALPHA-AL<sub>2</sub>O<sub>3</sub> HETEROSTRUCTURE AND DETERMINATION OF THE INTRINSIC LATTICE-CONSTANTS OF GAN FREE FROM THE STRAIN*. Japanese Journal of Applied Physics Part 2-Letters, 1992. 31(10B): p. L1454-L1456.
99. Paszkowicz, W., *X-ray powder diffraction data for indium nitride*. Powder Diffraction, 1999. 14(4): p. 258-260.
100. Leszczynski, M., et al., *LATTICE-CONSTANTS, THERMAL-EXPANSION AND COMPRESSIBILITY OF GALLIUM NITRIDE*. Journal of Physics D-Applied Physics, 1995. 28(4A): p. A149-A153.
101. Deguchi, T., et al., *Structural and vibrational properties of GaN*. Journal of Applied Physics, 1999. 86(4): p. 1860-1866.
102. Wu, J., et al., *Unusual properties of the fundamental band gap of InN*. Applied Physics Letters, 2002. 80(21): p. 3967-3969.
103. Xu, Y.N. and W.Y. Ching, *ELECTRONIC, OPTICAL, AND STRUCTURAL-PROPERTIES OF SOME WURTZITE CRYSTALS*. Physical Review B, 1993. 48(7): p. 4335-4351.
104. Lambrecht, W.R.L.a.S., B., *Band structure of the group-III nitrides*, in *Gallium Nitride, Semiconductors and Semimetals*, J.I.P.a.T.D. Moustakas, Editor. 1998, Academic Press: San Diego.
105. Park, J.K., et al., *White light-emitting diodes of GaN-based Sr<sub>2</sub>SiO<sub>4</sub> : Eu and the luminescent properties*. Applied Physics Letters, 2003. 82(5): p. 683-685.
106. Okumura, H., *Present status and future prospect of widegap semiconductor high-power devices*. Japanese Journal of Applied Physics Part 1-Regular Papers Brief Communications & Review Papers, 2006. 45(10A): p. 7565-7586.
107. DenBaars, S.P., *Basic Physics & Materials Technology of GaN LEDs and LDs*, in *Introduction to Nitride Semiconductor Blue Lasers and Light Emitting Diodes*, S.N.a.S.F. Chichibu, Editor. 2000, Taylor & Francis: London.

108. Shuji Nakamura, S.P., and Gerhard Fasol, *The Blue Laser Diode*. 2000: Springer.
109. Ledentsov, N.N., *Growth Processes and Surface Phase Equilibria in Molecular Beam Epitaxy*. 1999, Berlin: Springer.
110. Lei, T., et al., *Epitaxial-Growth of Zinc Blende and Wurtzitic Gallium Nitride Thin-Films on (001) Silicon*. Applied Physics Letters, 1991. 59(8): p. 944-946.
111. F, F.F.a.S., Ber. Deutsch Chem. Ges., 1910. 43: p. 1465.
112. Hovel, H.J. and J.J. Cuomo, *Electrical and Optical Properties of rf-Sputtered GaN and InN*. Applied Physics Letters, 1972. 20(2): p. 71-73.
113. Zembutsu, S. and M. Kobayashi, *The growth of c-axis-oriented GaN films by D.C.-biased reactive sputtering*. Thin Solid Films, 1985. 129(3-4): p. 289-297.
114. Kubota, K., Y. Kobayashi, and K. Fujimoto, *PREPARATION AND PROPERTIES OF III-V NITRIDE THIN-FILMS*. Journal of Applied Physics, 1989. 66(7): p. 2984-2988.
115. Meng, W.J. and T.A. Perry, *STRAIN EFFECTS IN EPITAXIAL GAN GROWN ON ALN-BUFFERED SI(111)*. Journal of Applied Physics, 1994. 76(12): p. 7824-7828.
116. Ross, J., M. Rubin, and T.K. Gustafson, *SINGLE-CRYSTAL WURTZITE GAN ON (111) GAAS WITH ALN BUFFER LAYERS GROWN BY REACTIVE MAGNETRON SPUTTER-DEPOSITION*. Journal of Materials Research, 1993. 8(10): p. 2613-2616.
117. Singh, P., et al., *Growth and characterization of GaN thin films by magnetron sputter epitaxy*. Journal of Vacuum Science & Technology a-Vacuum Surfaces and Films, 1998. 16(2): p. 786-789.
118. Tang, H., et al., *Influence of crystalline defects on transport properties of GaN grown by ammonia-molecular beam epitaxy and magnetron sputter epitaxy*. Journal of Electronic Materials, 2000. 29(3): p. 268-273.
119. Tansley, T.L., R.J. Egan, and E.C. Horrigan, *PROPERTIES OF SPUTTERED NITRIDE SEMICONDUCTORS*. Thin Solid Films, 1988. 164: p. 441-448.

120. Daigo, Y. and N. Mutsukura, *Synthesis of epitaxial GaN single-crystalline film by ultra high vacuum r.f. magnetron sputtering method*. Thin Solid Films, 2005. 483(1-2): p. 38-43.
121. Elkashef, N., et al., *Sputter deposition of gallium nitride films using a GaAs target*. Thin Solid Films, 1998. 333(1-2): p. 9-12.
122. Guo, Q.X., et al., *Growth condition dependence of structure and surface morphology of GaN films on (III)GaAs substrates prepared by reactive sputtering*. Journal of Vacuum Science & Technology A, 2004. 22(4): p. 1290-1292.
123. Horng, R.H., et al., *A research on the persistent photoconductivity behavior of GaN thin films deposited by r.f. magnetron sputtering*. Thin Solid Films, 1999. 343: p. 642-645.
124. Kikuma, T., et al., *GaN films deposited by planar magnetron sputtering*. Vacuum, 2002. 66(3-4): p. 233-237.
125. Kim, J.H., M.R. Davidson, and P.H. Holloway, *Electroluminescence from Tm-doped GaN deposited by radio-frequency planar magnetron sputtering*. Applied Physics Letters, 2003. 83(23): p. 4746-4748.
126. Knox-Davies, E.C., J.M. Shannon, and S.R.P. Silva, *The properties and deposition process of GaN films grown by reactive sputtering at low temperatures*. Journal of Applied Physics, 2006. 99(7).
127. Kusaka, K., et al., *Effect of substrate temperature on crystal orientation and residual stress in radio frequency sputtered gallium-nitride films*. Journal of Vacuum Science & Technology A, 2004. 22(4): p. 1587-1590.
128. Lakshmi, E., et al., *The Growth of Highly Resistive Gallium Nitride Films*. Thin Solid Films, 1980. 74(1): p. 77-82.
129. Maruyama, T. and H. Miyake, *Gallium nitride thin films deposited by radio-frequency magnetron sputtering*. Journal of Vacuum Science & Technology A, 2006. 24(4): p. 1096-1099.
130. Miyazaki, T., et al., *Properties of GaN films deposited on Si(111) by radio-frequency-magnetron sputtering*. Journal of Applied Physics, 2001. 89(12): p. 8316-8320.
131. Park, M., et al., *X-ray and Raman analyses of GaN produced by ultrahigh-rate magnetron sputter epitaxy*. Applied Physics Letters, 2002. 81(10): p. 1797-1799.

132. Shirakata, S., R. Sasaki, and T. Kataoka, *Photoluminescence of Eu-doped GaN thin films prepared by radio frequency magnetron sputtering*. Applied Physics Letters, 2004. 85(12): p. 2247-2249.
133. Preschilla, N., et al., *Nanocrystalline gallium nitride thin films*. Applied Physics Letters, 2000. 77(12): p. 1861-1863.
134. Zembutsu, S. and M. Kobayashi, *The Growth of C-Axis-Oriented GaN Films by Dc-Biased Reactive Sputtering*. Thin Solid Films, 1985. 129(3-4): p. 289-297.
135. Shinoda, H. and N. Mutsukura, *Structural properties of GaN and related alloys grown by radio-frequency magnetron sputter epitaxy*. Thin Solid Films, 2008. 516(10): p. 2837-2842.
136. Liu, L. and J.H. Edgar, *Substrates for gallium nitride epitaxy*. Materials Science & Engineering R-Reports, 2002. 37(3): p. 61-127.
137. Maruyama, M., *Ruby Crystals Grown by the Czochralski Technique*. Japanese Journal of Applied Physics, 1966. 5: p. 1026-1028.
138. Kurlov, V.N. and B.M. Epelbaum, *EFG growth of sapphire tubes upto 85mm in diameter*. Journal of Crystal Growth, 1998. 187(1): p. 107-110.
139. Qiang, Z., D. Peizhen, and G. Fuxi, *X - ray topographic investigation of characteristic dislocation structure in sapphire single crystals*. Journal of Applied Physics, 1990. 67(10): p. 6159-6164.
140. Ambacher, O., *Growth and applications of Group III nitrides*. Journal of Physics D-Applied Physics, 1998. 31(20): p. 2653-2710.
141. Lei, T., K.F. Ludwig, and T.D. Moustakas, *Heteroepitaxy, polymorphism, and faulting in GaN thin films on silicon and sapphire substrates*. Journal of Applied Physics, 1993. 74(7): p. 4430-4437.
142. Morkoç, H., in *Handbook of Nitride Semiconductors and Devices*. 2008, WILEY-VCH Verlag GmbH & Co. KGaA. p. 373.
143. Melton, W.A. and J.I. Pankove, *GaN growth on sapphire*. Journal of Crystal Growth, 1997. 178(1-2): p. 168-173.
144. Doppalapudi, D., et al., *Epitaxial growth of gallium nitride thin films on A-Plane sapphire by molecular beam epitaxy*. Journal of Applied Physics, 1999. 85(7): p. 3582-3589.

145. Kato, T., et al., *Morphology of twinned GaN grown on (11-0) sapphire substrates*. Solid-State Electronics, 1997. 41(2): p. 227-229.
146. Kato, T., et al., *Simultaneous growth of two different oriented GaN epilayers on (1 1 · 0) sapphire I. Morphology and orientation*. Journal of Crystal Growth, 1997. 173(3-4): p. 244-248.
147. Cheng, L., et al., *Microstructures of GaN films grown by low pressure metal-organic vapor phase epitaxy on (0#&#xa0;1#&#xa0;1#&#xa0;2) sapphire substrates*. Journal of Crystal Growth, 1998. 191(4): p. 641-645.
148. Hwang, J.S., et al., *Heteroepitaxy of gallium nitride on (0001), (1012) and (1010) sapphire surfaces*. Journal of Crystal Growth, 1994. 142(1-2): p. 5-14.
149. Perkins, J. *LED Manufacturing Technologies & Costs*. 2009 Sep. 30, 2013]; Available from: [http://apps1.eere.energy.gov/buildings/publications/pdfs/ssl/perkins\\_fairfax09.pdf](http://apps1.eere.energy.gov/buildings/publications/pdfs/ssl/perkins_fairfax09.pdf).
150. Morkoc, H., *Handbook of Nitride Semiconductors and Devices*. 2008, WILEY-VCH Verlag Gmbh & Co. KGaA. p. 372.
151. Morkoc, H., *Handbook of Nitride Semiconductors and Devices*. 2008, WILEY-VCH Verlag Gmbh & Co. KGaA. p. 500.
152. Morkoç, H., in *Handbook of Nitride Semiconductors and Devices*. 2008, WILEY-VCH Verlag Gmbh & Co. KGaA. p. 337.
153. Harris, G.L. and INSPEC, in *Properties of Silicon Carbide*. 1995, INSPEC, Institution of Electrical Engineers. p. 4.
154. Harris, G.L. and INSPEC, in *Properties of Silicon Carbide*. 1995, INSPEC, Institution of Electrical Engineers. p. 3.
155. Harris, G.L. and INSPEC, in *Properties of Silicon Carbide*. 1995, INSPEC, Institution of Electrical Engineers. p. 5.
156. Kh. S. Bagdasarov, E.R.D., V.V. Pishchik, M.M. Chernik, Yu. Yu, A.S.Gershun, I.F.Zvyaginsteva, *Sov. Phys. Crystallogr.*, 1973. 18: p. 242.
157. Robert R. Reeber, K.W., *Lattice Parameters and Thermal Expansion of Important Semiconductors and Their Substrates*. Mat. Res. Soc. Symp., 2000. 622: p. T6. 35. 1.

158. Siergiej, R.R., et al., *Advances in SiC materials and devices: an industrial point of view*. Materials Science and Engineering: B, 1999. 61–62(0): p. 9-17.
159. Morkoç, H., in *Handbook of Nitride Semiconductors and Devices*. 2008, WILEY-VCH Verlag Gmbh & Co. KGaA. p. 335.
160. Morkoç, H., in *Handbook of Nitride Semiconductors and Devices*. 2008, WILEY-VCH Verlag Gmbh & Co. KGaA. p. 336.
161. Tairov, Y.M. and V.F. Tsvetkov, *Investigation of growth processes of ingots of silicon carbide single crystals*. Journal of Crystal Growth, 1978. 43(2): p. 209-212.
162. Sanchez-Garcia, M.A., et al., *Ultraviolet electroluminescence in GaN/AlGaN single-heterojunction light-emitting diodes grown on Si(111)*. Journal of Applied Physics, 2000. 87(3): p. 1569-1571.
163. Okada, Y., in *Properties of Crystalline Silicon*, R. Hull, Editor. 1999, IEE: London. p. 91.
164. Wybourne, M.N., in *Properties of Crystalline Silicon*, R. Hull, Editor. 1999, IEE: London. p. 165.
165. T. Soma, H.-M.K., in *Properties of Crystalline Silicon*, R. Hull, Editor. 1999, IEE: London. p. 153.
166. Okada, Y. and Y. Tokumaru, *Precise determination of lattice parameter and thermal expansion coefficient of silicon between 300 and 1500 K*. Journal of Applied Physics, 1984. 56(2): p. 314-320.
167. Casey, H.C., *Devices for Integrated Circuits*. 1999, New York: Wiley.
168. Petrovic, J.J., et al., *TENSILE MECHANICAL-PROPERTIES OF SIC WHISKERS*. Journal of Materials Science, 1985. 20(4): p. 1167-1177.
169. Lee, J.a.C., IB, *Formation of Silicon Carbide from Rice Hulls*. American Ceramic Society Bulletin, 1975. 54(2): p. 195.
170. Milewski, J.V., et al., *GROWTH OF BETA-SILICON CARBIDE WHISKERS BY THE VLS PROCESS*. Journal of Materials Science, 1985. 20(4): p. 1160-1166.
171. Becher, P.F. and G.C. Wei, *TOUGHENING BEHAVIOR IN SIC-WHISKER-REINFORCED ALUMINA*. Journal of the American Ceramic Society, 1984. 67(12): p. C267-C269.

172. Wei, G.C. and P.F. Becher, *DEVELOPMENT OF SIC-WHISKER-REINFORCED CERAMICS*. American Ceramic Society Bulletin, 1985. 64(2): p. 298-304.
173. Becher, P.F., et al., *TOUGHENING BEHAVIOR IN WHISKER-REINFORCED CERAMIC MATRIX COMPOSITES*. Journal of the American Ceramic Society, 1988. 71(12): p. 1050-1061.
174. Faber, K.T. and A.G. Evans, *CRACK DEFLECTION PROCESSES .1. THEORY*. Acta Metallurgica, 1983. 31(4): p. 565-576.
175. Hasson, D.F., S.M. Hoover, and C.R. Crowe, *EFFECT OF THERMAL-TREATMENT ON THE MECHANICAL AND TOUGHNESS PROPERTIES OF EXTRUDED SICW/ALUMINIUM-6061 METAL MATRIX COMPOSITE*. Journal of Materials Science, 1985. 20(11): p. 4147-4154.
176. *Brocheur, 3M Optical Systems Vikuiti™ Brightness Enhancement Film*. 2010.
177. Mistler, R.E., & Twiname, Eric R., *Tape Casting Theory and Practice*. 2000, The American Ceramic Society: Westerville. p. 97.
178. Courtesy of Nik Jewell.
179. He, B.B., *Geometry Conventions*, in *Two-Dimensional X-Ray Diffraction*. 2009, John Wiley & Sons, Inc.: Hoboken, New Jersey. p. 29.
180. He, B.B., *Introduction*, in *Two-Dimensional X-Ray Diffraction*. 2009, John Wiley & Sons, Inc.: Hoboken, New Jersey. p. 23.
181. Muller, D.A., *Structure and bonding at the atomic scale by scanning transmission electron microscopy*. Nature Materials, 2009. 8(4): p. 263-270.
182. Zhu, G., *High-Resolution Characterization of Low-Dimensional Defects in SrTiO<sub>3</sub>*, in *Department of Materials Science and Engineering 2012*, McMaster University: Hamilton, Ontario, Canada. p. 31.
183. *High-Angle Annular Dark-Field (HAADF) Microscopy*. [cited 2013 Dec-6-2013]; Available from: <http://le-csss.asu.edu/node/16>.
184. Egerton, R.F., *Electron energy-loss spectroscopy in the TEM*. Reports on Progress in Physics, 2009. 72(1).
185. *Binary alloy phase diagrams*, ed. T.B. Massalski, et al. 1986, American Society for Metals: Metals Park, Ohio.

186. Abraham, E.R.I. and E.A. Cornell, *Teflon feedthrough for coupling optical fibers into ultrahigh vacuum systems*. Applied Optics, 1998. 37(10): p. 1762-1763.
187. *Courtesy of Swagelok*.
188. Morkoç, H., in *Handbook of Nitride Semiconductors and Devices*. 2008, WILEY-VCH Verlag GmbH & Co. KGaA. p. 444.
189. Morkoç, H., in *Handbook of Nitride Semiconductors and Devices*. 2008, WILEY-VCH Verlag GmbH & Co. KGaA. p. 445.
190. Morkoç, H., in *Handbook of Nitride Semiconductors and Devices*. 2008, WILEY-VCH Verlag GmbH & Co. KGaA. p. 449.
191. Auchterlonie, G.J., D.R. McKenzie, and D.J.H. Cockayne, *Using ELNES with parallel EELS for differentiating between a-Si:X thin films*. Ultramicroscopy, 1989. 31(2): p. 217-222.
192. Colliex, C., *Advances in Optical and Electron Microscopy*, ed. a.V.E.C. R. Barer. Vol. 19. 1984, London: Academic Press.
193. Kimoto, K., T. Sekiguchi, and T. Aoyama, *Chemical shift mapping of Si L and K edges using spatially resolved EELS and energy filtering TEM*. Journal of Electron Microscopy, 1997. 46(5): p. 369-374.
194. Brown, F.C., R.Z. Bachrach, and M. Skibowski, *L<sub>23</sub> threshold spectra of doped silicon and silicon compounds*. Physical Review B, 1977. 15(10): p. 4781-4788.
195. Nakada, Y., I. Aksenov, and H. Okumura, *GaN heteroepitaxial growth on silicon nitride buffer layers formed on Si (111) surfaces by plasma-assisted molecular beam epitaxy*. Applied Physics Letters, 1998. 73(6): p. 827-829.
196. Harp, G.R., D.K. Saldin, and B.P. Tonner, *FINITE-SIZE EFFECTS AND SHORT-RANGE CRYSTALLINE ORDER IN SI AND SiO<sub>2</sub> STUDIED BY X-RAY-ABSORPTION FINE-STRUCTURE SPECTROSCOPY*. Journal of Physics-Condensed Matter, 1993. 5(31): p. 5377-5388.
197. Bernhardt, J., et al., *Epitaxially ideal oxide-semiconductor interfaces: Silicate adlayers on hexagonal (0001) and (000(1)over-bar) SiC surfaces*. Applied Physics Letters, 1999. 74(8): p. 1084-1086.
198. Kim, M., et al., *Epitaxial growth mechanisms of AlN on SiC substrates at room temperature*. Applied Physics Letters, 2007. 91(15).

199. Horita, M., J. Suda, and T. Kimoto, *High-quality nonpolar 4H-AIN grown on 4H-SiC (11(2)over-bar20) substrate by molecular-beam epitaxy*. Applied Physics Letters, 2006. 89(11).
200. Edgar, J.H., et al., *X-ray diffraction and high resolution transmission electron microscopy of 3C-SiC/AIN/6H-SiC(0001)*. Journal of Electronic Materials, 1997. 26(12): p. 1389-1393.